

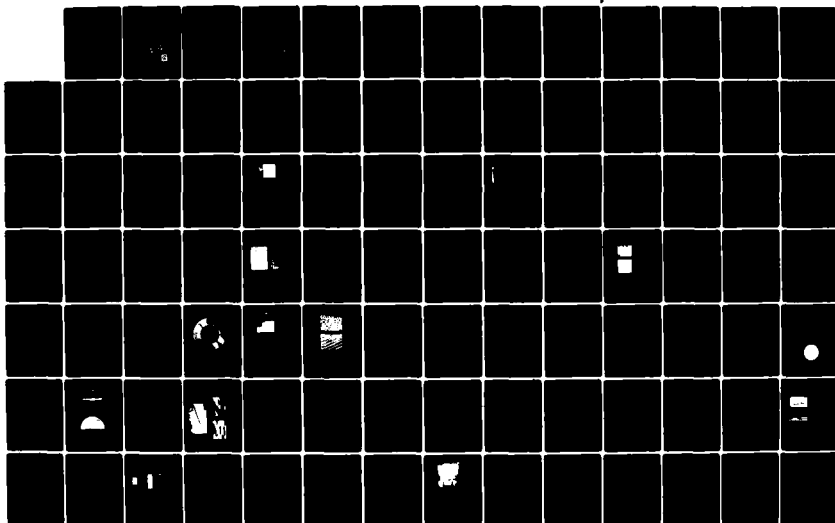
AD-A122 252

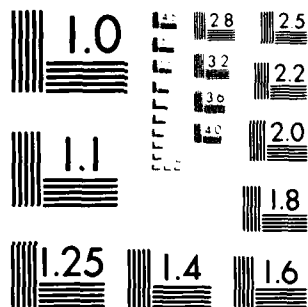
SOLID STATE RESEARCH(U) MASSACHUSETTS INST OF TECH
LEXINGTON LINCOLN LAB A L MCWHORTER 15 MAY 82 1982-2
ESD-TR-82-055 F19628-80-C-0002

1/2

UNCLASSIFIED

F/G 20/12 NL





MICROCOPY RESOLUTION TEST CHART
NATIONAL BUREAU OF STANDARDS-1963-A

40 A 122202

12

2

Solid State Research

1982

DTIC

(101-0-3)



1

**MASSACHUSETTS INSTITUTE OF TECHNOLOGY
LINCOLN LABORATORY**

SOLID STATE RESEARCH

QUARTERLY TECHNICAL SUMMARY REPORT

1 FEBRUARY — 30 APRIL 1982

ISSUED 27 AUGUST 1982



Approved for public release; distribution unlimited.

LEXINGTON

MASSACHUSETTS

ABSTRACT

This report covers in detail the solid state research work of the Solid State Division at Lincoln Laboratory for the period 1 February through 30 April 1982. The topics covered are Solid State Device Research, Quantum Electronics, Materials Research, Microelectronics, and Analog Device Technology. Funding is primarily provided by the Air Force, with additional support provided by the Army, DARPA, Navy, NASA, and DOE.

Accession For	✓
NTIS GRA&I	
DTIC TAB	
Unannounced	
Justification	
By	
Distribution	
Availability	
Dist	
A	

TABLE OF CONTENTS

Abstract	iii
Introduction	vii
Reports on Solid State Research	xi
Organization	xvii
 I. SOLID STATE DEVICE RESEARCH	 1
A. Excess Noise Factor in InP Avalanche Photodiodes	1
B. Threshold Characteristics of GaInAsP/InP Double Heterostructure Lasers	4
C. Beryllium-Implanted GaInAsP/InP Double Heterojunction Laser Diodes	7
D. A Slow Selective Etch for GaInAsP Grown on InP	14
 II. QUANTUM ELECTRONICS	 21
A. Effects of Temporal Correlation on Signal Averaging of LIDAR Measurements	21
B. Stimulated Surface Plasma Waves and the Growth of Grating Structures in Laser Photodeposited Metal Films	29
C. High-Speed X-Ray-Sensitive InP Photoconductive Detectors	31
 III. MATERIALS RESEARCH	 39
A. Low-Dislocation-Density GaAs Epilayers Grown on Ge-Coated Si Substrates by Means of Lateral Epitaxial Overgrowth	39
B. Effects of Ionizing Radiation on n-Channel MOSFETs Fabricated in Zone-Melting-Recrystallized Si Films on SiO ₂ -Coated Substrates	45
C. Zone-Melting Recrystallization of Si Films on SiO ₂ -Coated Si Substrates	50

IV. MICROELECTRONICS	59
A. Charge-Coupled Devices: Time-Integrating Correlator	59
B. A Two-Stage Monolithic IF Amplifier Utilizing a High Dielectric Constant Capacitor	63
C. Heterodyne Experiments from Millimeter-Wave to Optical Frequencies Using GaAs MESFETs Above f_T	75
D. Si Damage Induced by Dry Etching	80
V. ANALOG DEVICE TECHNOLOGY	89
A. Superconductive Matched Filters: Pulse Compression	89
B. Temperature Dependence of Wideband SAW RAC Devices on Quartz	93
1. Introduction	93
2. Theory	94
3. Measurements	97
4. Results and Conclusions	98

INTRODUCTION

I. SOLID STATE DEVICE RESEARCH

The excess noise factor as a function of multiplication has been determined in p^+-n-n^+ inverted-mesa InP avalanche photodiodes. The noise factor is below 3 for multiplication values less than 10, but rises rapidly for higher multiplication as was previously observed in GaInAsP/InP diodes. The ratio of the ionization coefficients determined from noise data is shown to depend on the model used.

GaInAsP/InP double-heterostructure laser wafers were grown, fabricated into lasers, and evaluated. By using nearly optimized growth conditions, a high yield of lasers with low threshold current density J_{th} emitting at 1.3 μm wavelength was obtained. Accurate measurements of the active-layer thicknesses d yielded J_{th}/d values of 5 to 4.5 $kA/cm^2-\mu m$ as d increased from 0.45 to 1.1 μm .

Be-implanted broad-area GaInAsP/InP double-heterostructure laser diodes operating at 1.3 μm have been fabricated which have threshold current densities comparable to those prepared using conventional Zn doping during the epitaxial growth of the InP cap layer. The lowest threshold current density measured in an implanted laser was 1.2 kA/cm^2 , corresponding to J_{th}/d of 4.2 $kA/cm^2-\mu m$. A more typical lower value of J_{th} on wafers with thin active layers (0.25 to 0.35 μm) was 2.0 kA/cm^2 .

The technology for fabricating laser diodes, detectors, and optical waveguides in GaInAsP/InP epitaxial wafers requires the use of suitable etching techniques for providing smooth, damage-free surfaces for precision pattern geometries and for the preferential and reproducible removal of specific layers. It has been found that a 1 H_2SO_4 :1 H_2O_2 :10 H_2O room-temperature solution etches (100) $Ga_{0.27}In_{0.73}As_{0.03}P_{0.37}$ ($\lambda = 1.3 \mu m$) at a very constant etch rate of 1000 $\text{\AA}/min$. Various other ratios of $H_2SO_4:H_2O_2:H_2O$ should prove useful as slow selective etches for GaInAsP in a variety of applications.

II. QUANTUM ELECTRONICS

The limitations of signal averaging due to temporal correlation in laser remote-sensing measurements have been determined experimentally. The results are in excellent agreement with the theoretically predicted improvement in measurement accuracy achievable by signal-averaging partially correlated data. With temporal correlations, the improvement in the standard deviation that can be obtained by signal-averaging is limited, regardless of the number of pulses averaged.

The submicrometer ripple structures observed in UV-laser photodeposited metal films have been shown to arise from stimulated surface plasma-wave scattering processes. This is the first observation of a stimulated scattering process involving surface electromagnetic waves.

The response of Fe-doped InP photoconductive detectors to ~9-keV x-ray pulses has been examined, and device risetimes <90 ps have been measured. The devices are the fastest solid-state x-ray detectors reported to date; they are simple, compact, and could be integrated into array structures.

III. MATERIALS RESEARCH

Single-crystal GaAs layers have been obtained by means of lateral epitaxial overgrowth seeded within stripe openings in a SiO_2 mask over GaAs layers grown on Ge-coated Si substrates. The dislocation density in the laterally overgrown layers is less than 10^4 cm^{-2} , compared with 10^7 to 10^8 cm^{-2} for the layers grown directly on the Ge/Si substrates, indicating that the overgrown layers will be useful for solar cells and other device applications.

A study has been made of the effects of ionizing radiation on the electrical characteristics of n-channel MOSFETs fabricated in zone-melting-recrystallized Si films on SiO_2 -coated Si substrates. These effects can be largely suppressed by applying a moderate negative bias to the substrates during irradiation and device operation, so that these devices are promising components for radiation-hardened circuits.

A scaled-up graphite strip-heater system has been constructed for routine zone-melting recrystallization of Si films on SiO₂-coated Si substrates. Almost all large-angle grain boundaries have been eliminated by means of seeded recrystallization, which is accomplished by scribing a stripe opening that extends through the Si and SiO₂ films to the Si wafer, but the films still contain large numbers of low-angle subgrain boundaries.

IV. MICROELECTRONICS

The design of a charge-coupled-device time-integrating correlator for use with the Global Positioning System P-code has been completed. An input structure has been chosen which generates the required complementary charge packets and is not susceptible to a CW jammer at the carrier frequency. The design of the charge integrator incorporates a skimming process which reduces the amount of charge transferred to the output register without introducing temporal noise onto the signal.

A two-stage monolithic IF amplifier incorporating a reactively sputtered Ta₂O₅ capacitor has been fabricated. The capacitor is a sequentially sputtered composite layer structure consisting of Au, Ta, Ta₂O₅, Ta and Au, and has a unit area capacitance of 1500 pF/mm². The amplifiers exhibit a gain of 17.5 ± 1.0 dB for 1.2 to 2.6 GHz and a minimum noise figure of ~2.7 dB, with an associated gain of 17.5 dB at 1.7 GHz.

Response of GaAs FETs in millimeter-wave and optical-heterodyne experiments has been obtained at frequencies above the frequency of unity current gain f_T . In the mixing of two visible lasers, beat frequencies as high as 300 GHz have been observed. These high IFs were downconverted to microwave frequencies by radiatively coupling millimeter-wave local oscillators into the gate region.

The effects on silicon surfaces of reactive ion etching with CF₄, CHF₃, SiCl₄, or Cl₂ and ion milling with Ar were investigated by measurements on MOS structures fabricated on etched surfaces, and by Secco etching to determine the extent of oxidation-induced stacking faults. Chlorine-based

gases produced less damage during etching than fluorine-based gases, and surfaces etched in CHF_3 provided a better Si-SiO₂ interface than those etched by CF_4 . The density of oxidation-induced stacking faults after Ar ion milling was found to increase with ion energy.

V. ANALOG DEVICE TECHNOLOGY

Superconductive tapped delay lines have been configured as upchirp and downchirp filters, with bandwidths of 2 GHz and dispersion times of 27 ns. Also, pulse compression has been demonstrated with a matched pair of these unweighted filters. The compressed pulse output, obtained in a preliminary experiment using 800 MHz of bandwidth and 11 ns of delay, closely matches the results obtained from an accurate theoretical model.

An analytical model developed to explain the temperature dependence of surface-acoustic-wave reflective-array devices fabricated on anisotropic substrates has been applied to ST-quartz devices. The calculated results were in excellent agreement with measurements of the temperature dependence of chirp slope, group delay, and insertion loss for dispersive filters fabricated on this cut. Devices fabricated on both isotropic-RAC-cut and ST-cut quartz were found to be temperature stable, with a stability about 100 times better than that of devices fabricated on lithium niobate.

REPORTS ON SOLID STATE RESEARCH

15 February through 15 May 1982

PUBLISHED REPORTS

Journal Articles

JA No. 5209	Photovoltaic Cells	J.C.C. Fan	In Kirk Jthmer: <u>Encyclopedia of Chemical Technology</u> , Vol. 17, Third Edition (Wiley, New York, 1982), pp. 709-732
5269	The Permeable Base Transistor and Its Application to Logic Circuits	C.O. Bozler G.D. Alley	Proc. IEEE <u>70</u> , 46 (1982)
5270	Production and Annealing of Ion-Bombardment Damage in Silicides of Pt, Pd, and Ni	B-Y. Tsaur C.H. Anderson, Jr.	J. Appl. Phys. <u>53</u> , 940 (1982)
5277	Efficient Raman Frequency Conversion in Liquid Nitrogen	S.R.J. Brueck H. Kildal	IEEE J. Quantum Electron. <u>QE-18</u> , 310 (1982)
5279	Zone-Melting Recrystallization of Encapsulated Silicon Films on SiO ₂ - Morphology and Crystallography	M.W. Geis H.I. Smith* B-Y. Tsaur J.C.C. Fan E.W. Maby* D.A. Antoniadis*	Appl. Phys. Lett. <u>40</u> , 158 (1982)
5282	Stress-Enhanced Carrier Mobility in Zone Melting Recrystallized Polycrystalline Si Films on SiO ₂ -Coated Substrates	B-Y. Tsaur J.C.C. Fan M.W. Geis	Appl. Phys. Lett. <u>40</u> , 322 (1982)
5283	Localized Laser Etching of Compound Semiconductors in Aqueous Solution	R.M. Osgood, Jr. A. Sanchez-Rubio D.J. Ehrlich V. Daneu	Appl. Phys. Lett. <u>40</u> , 391 (1982)
5295	Effects of Subgrain Boundaries on Carrier Transport in Zone-Melting-Recrystallized Si Films on SiO ₂ -Coated Si Substrates	B-Y. Tsaur J.C.C. Fan M.W. Geis D.J. Silversmith R.W. Mountain	IEEE Electron Device Lett. <u>EDL-3</u> , 79 (1982)
5303	Picosecond InP Optoelectronic Switches	A.G. Foyt F.J. Leonberger R.C. Williamson	Appl. Phys. Lett. <u>40</u> , 447 (1982)

* Author not at Lincoln Laboratory.

JA No. 5308	Applications of Guided-Wave Interferometers	F.J. Leonberger	Laser Focus <u>18</u> , 125 (1982)
5310	Raman Measurements of Stress in Silicon-on-Sapphire Device Structures	S.R.J. Brueck B-Y. Tsaur J.C.C. Fan D.V. Murphy T.F. Deutsch D.J. Silversmith	Appl. Phys. Lett. <u>40</u> , 895 (1982)
5312	4-Bit 828-Megasample/s Electro-optic Guided-Wave Analog-to-Digital Converter	F.J. Leonberger C.E. Woodward R.A. Becker	Appl. Phys. Lett. <u>40</u> , 565 (1982)
5313	Transient Annealing of Selenium-Implanted Gallium Arsenide Using a Graphite Strip Heater	R.L. Chapman J.C.C. Fan J.P. Donnelly B-Y. Tsaur	Appl. Phys. Lett. <u>40</u> , 805 (1982)
5318	A Novel Technique for GaInAsP/InP Buried Heterostructure Laser Fabrication	Z.L. Liau J.N. Walpole	Appl. Phys. Lett. <u>40</u> , 568 (1982)
5320	Observation of Linewidth Broadening in (GaAl)As Diode Lasers Due to Electron Number Fluctuations	D. Welford A. Mooradian	Appl. Phys. Lett. <u>40</u> , 560 (1982)
5326	Efficient GaAs Solar Cells Formed by UV Laser Chemical Doping	T.F. Deutsch J.C.C. Fan D.J. Ehrlich G.W. Turner R.L. Chapman R.P. Gale	Appl. Phys. Lett. <u>40</u> , 722 (1982)
5327	Output Power and Temperature Dependence of the Linewidth of Single-Frequency cw (GaAl)As Diode Lasers	D. Welford A. Mooradian	Appl. Phys. Lett. <u>40</u> , 865 (1982)
5331	Optically Pumped Mode-Locked InGaAsP Lasers	R.S. Putnam* C.B. Roxlo* M.M. Salour* S.H. Groves M.C. Plonko	Appl. Phys. Lett. <u>40</u> , 660 (1982)

Meeting Speeches

MS No. 5650	The Effect of Grooves in Amorphous Substrates on the Orientation of Metal Deposits	R. Anton* H. Poppa* D.C. Flanders	J. Cryst. Growth <u>56</u> , 433 (1982)
----------------	--	---	---

* Author not at Lincoln Laboratory.

MS No. 5707C	Summary Abstract: Photodeposition of Metal Films with Ultraviolet Laser Light	D.J. Ehrlich R.M. Osgood, Jr. T.F. Deutsch	J. Vac. Sci. Technol. <u>20</u> , 738 (1982)
5751	Experimental and Theoretical Analysis of Temperature Dependence of Wideband SAW RAC Devices on Quartz	D.M. Boroson D.E. Gates	1981 Ultrasonics Symposium Proceedings (IEEE, New York, 1981), pp. 38-43
5752	High Performance Elastic Convolver with Extended Time-Bandwidth Product	I. Yao	1981 Ultrasonics Symposium Proceedings (IEEE, New York, 1981), pp. 181-185
5755	Compact Multiple-Channel SAW Sliding-Window Spectrum Analyzer	D.R. Arsenault V.S. Dolat	1981 Ultrasonics Symposium Proceedings (IEEE, New York, 1981), pp. 220-225
5756	A SAW Tapped Delay Line with Short (15-ns) Pedestal of Delay and High (>110 dB) Feedthrough Isolation	D.E. Gates R.W. Ralston	1981 Ultrasonics Symposium Proceedings (IEEE, New York, 1981), pp. 44-47
5764	Single-Crystal GaAs Films on Amorphous Substrates by the CLEFT Process	C.O. Bozler R.W. McClelland J.P. Salerno J.C.C. Fan	J. Vac. Sci. Technol. <u>20</u> , 720 (1982)

* * * * *

UNPUBLISHED REPORTS

Journal Articles

JA No. 5274	Photodeposition of Metal Films with Ultraviolet Laser Light	D.J. Ehrlich R.M. Osgood, Jr. T.F. Deutsch	Accepted by J. Vac. Sci. Technol.
5300	II-VI and IV-VI Semiconductors	A.J. Strauss	Accepted by <u>Encyclopedia of Materials Science and Engineering</u> (Pergamon Press, New York)
5314	Laser Remote Sensing of Hydrazine, MMH and UDMH Using a Differential-Absorption CO ₂ LIDAR	N. Menyuk D.K. Killinger W.E. DeFeo	Accepted by Appl. Opt.

JA No. 5316	Tantalum Oxide Capacitors for GaAs Monolithic Integrated Circuits	M.E. Fira A. Chu L.J. Mahoney R.T. Gerretani W.E. Courtney	Accepted by IEEE Electron Device Lett.
5321	Fabrication of Through-Wafer Via Conductors in Si by Laser Photochemical Processing	D.J. Ehrlich D.J. Silversmith R.W. Mountain J.Y. Tsao	Accepted by IEEE Trans. Components, Hybrids, and Manufacturing Technology
5325	An Integrated Optical Temperature Sensor	L.M. Johnson F.J. Leonberger G.W. Pratt, Jr.*	Accepted by Appl. Phys. Lett.
5335	Pulse-Pumped Operation of Divalent Transition-Metal Lasers	P.F. Moulton	Accepted by IEEE J. Quantum Electron.
5360	Speculations on Solid State Tunable Lasers	P.F. Moulton	Accepted by IEEE J. Quantum Electron. (Editorial Section)

Meeting Speeches†

MS No. 5609C	Advances in Divalent Transition-Metal Lasers	P.F. Moulton	Seminar, Boston College, Newton, Massachusetts, 21 April 1982
5632C	InP Optoelectronic Mixers	A.G. Foyt	United Technologies Research Center, E. Hartford, Connecticut, 26 March 1982
5707F	Ultraviolet-Laser Photodeposition	D.J. Ehrlich J.Y. Tsao	Workshop on Diamond-Like Carbon Films, Albuquerque, New Mexico, 19-20 April 1982
5899A	Raman Scattering as a Probe of Thin-Films	S.R.J. Brueck	
5707G	Laser Photodeposition of Thin Film Structures	D.J. Ehrlich	OSA/IEEE Regional Mtg., San Jose, California, 21 April 1982
5726A	Current Status of Thin-Film GaAs Solar Cells	J.C.C. Fan C.O. Bozler R.W. McClelland	Space Photovoltaic Research and Technology Conf., Cleveland, Ohio, 20-22 April 1982

* Author not at Lincoln Laboratory.

† Titles of Meeting Speeches are listed for information only. No copies are available for distribution.

MS No. 5763A	Analysis of the Electronic Behavior of Grain Boundaries in GaAs	J.P. Salerno	American Association for Crystal Growth, New England Section, Cambridge, Massachusetts, 16 February 1982
5866	MMOS/CCD Nonvolatile Analog Memory	R.S. Withers D.J. Silversmith R.W. Mountain	IEEE Nonvolatile Semiconductor Memory Workshop, Monterey, California, 7-10 March 1982
5871	Picosecond InP Optoelectronic Switches	A.G. Foyt F.J. Leonberger R.C. Williamson	CLEO '82, Phoenix, Arizona, 14-16 April 1982
5881	High-Speed UV- and X-Ray-Sensitive InP Photoconductive Detectors	T.F. Deutsch F.J. Leonberger A.G. Foyt	
5883A	4-Bit 828-Megasample/s Guided-Wave Electrooptic Analog-to-Digital Converter	F.J. Leonberger C.E. Woodward R.A. Becker	
5888	Spatial-Period-Division Using an ArF Laser	A.M. Hawryluk* H.L. Smith* R.M. Osgood, Jr.* D.L. Ehrlich	
5899	Laser Raman Scattering as a Probe of Si Device Structures	S.R.J. Brueck B-Y. Tsaur D.V. Murphy J.C.C. Fan T.F. Deutsch D.L. Silversmith	
5910A	Fundamental Line Broadening Mechanisms of Single-Frequency CW (GaAl)As Diode Lasers	D. Kettord A. Mooradian	8th Strategic Space Symp., Monterey, California, 1-5 March 1982
6013	Review of Current Submillimeter Laser Applications	H.R. Fetterman	
6018	Laser Photodeposited Metal Films: Stimulated Surface Plasma Waves and Growth of Grating Structures	S.R.J. Brueck D.L. Ehrlich	
5886	Hybrid Analog/Digital Signal Processing	J.H. Cafarella	

*Author not at Lincoln Laboratory.

MS No. 5896	Raman Spectra of Ultrathin Si Films	D.V. Murphy S.R.J. Brueck D.D. Rathman	American Physical Society Mtg., Dallas, Texas, 8-12 March 1982
5913	Dry Etching of Gate Recesses for GaAs MESFETs	L.I. Mahoney A. Chu G.A. Lincoln M.W. Geis N.N. Efremow	Workshop on Compound Semiconductor Microwave Materials and Devices, Scottsdale, Arizona, 21-23 February 1982
5914	Fabrication of Surface Relief Structures for Permeable Base Transistors	R.A. Voiak K.B. Nichols G.A. Lincoln M.W. Geis R.W. McClelland D.C. Flanders J.P. Salerno	
5929	IR Detectors: Heterodyne and Direct	D.L. Spears	Workshop on Optical and Laser Remote Sensing, Monterey, California, 9-11 February 1982
5975	Nonlinear Optics with Simple Molecular Liquids	S.R.J. Brueck	Seminar, University of Toronto, Ontario, Canada, 30 March 1982
6003	Some Recent Progress in InGaAsP Lasers	J.N. Walpole	Optics and Quantum Electronics Seminar, M.I.T., 10 March 1982
6007	Electrooptical Devices for GHz Sampling and A/D Conversion	F.J. Leonberger	Seminar, Moore School of Engineering, University of Pennsylvania, 25 March 1982
6011	Surface Wave Technology	D.E. Oates	Ultrasonics Industry Association Technical Symp., New York, 31 March 1982
6029	Ion-Beam Mixing	B-Y. Tsaur	Symp. on Surface Modification of Materials, Oak Ridge, Tennessee, 16 April 1982

ORGANIZATION

SOLID STATE DIVISION

A.L. McWhorter, Head
I. Melngailis, Associate Head
J.F. Goodwin, Assistant

P.E. Tannenwald, Senior Staff

QUANTUM ELECTRONICS

A. Mooradian, Leader
P.L. Kelley, Associate Leader

Barch, W.F.	Johnson, B.C.*
Belanger, L.J.	Killinger, D.K.
Brueck, S.R.J.	Lenth, W.
Burke, J.W.	Lewis, R.C.*
Bushee, J.F.	Menyuk, N.
Coulombe, M.J.	Moulton, P.F.
DeFeo, W.E.	Murphy, D.V.
Deutsch, T.F.	Parker, C.D.
Ehrlich, D.J.	Peck, D.D.
Feldman, B.	Sullivan, D.J.
Fetterman, H.R.	Tsao, J.Y.
Goodhue, W.D.*	Welford, D.
Hancock, R.C.	

ELECTRONIC MATERIALS

A.J. Strauss, Leader
J.C.C. Fan, Assistant Leader
J.G. Mavroides, Senior Staff
H.J. Zeiger, Senior Staff

Anderson, C.H., Jr.	Krohn, L., Jr.
Branz, H.M.*	Mastromattei, E.L.
Button, M.J.	Metze, G.M.
Chapman, R.L.	Nitishin, P.M.
Davis, F.M.	Owens, E.B.
Delaney, E.J.	Palm, B.J.
Fahey, R.E.	Pantano, J.V.
Finn, M.C.	Salerno, J.P.*
Foley, G.H.	Tracy, D.M.
Gale, R.P.	Tsaur, B-Y.
Iseler, G.W.	Turner, G.W.
King, B.D.	Vohl, P.
Kolesar, D.F.	

APPLIED PHYSICS

R.C. Williamson, Leader
C.E. Hurwitz, Associate Leader
F.J. Leonberger, Assistant Leader
T.C. Harman, Senior Staff
R.H. Kingston, Senior Staff
R.H. Rediker, Senior Staff

Armiento, C.A.*	Groves, S.H.	Paladino, A.E.
Becker, R.A.	Hovey, D.L.	Plonko, M.C.
Carter, F.B.	Johnson, L.M.	Schloss, R.P.*
Chinnock, C.B.	Lattes, A.L.*	Spears, D.L.
DeMeo, N.L., Jr.	Liau, Z.L.	Tsang, D.Z.
Diadiuk, V.	Lind, T.A.	Walpole, J.N.
Donnelly, J.P.	McBride, W.F.	Woodhouse, J.D.
Ferrante, G.A.	O'Donnell, F.J.	
Foyt, A.G.	Orr, L.*	

*Research Assistant

ANALOG DEVICE TECHNOLOGY

E. Stern, Leader
J.H. Cafarella, Assistant Leader
R.W. Ralston, Assistant Leader

Anderson, A.C.	Flynn, G.T.	Oates, D.E.
Arsenault, D.R.	Holtham, J.H.	Reible, S.A.
Baker, R.P.	Kernan, W.C.	Sage, J.P.
Behrmann, G.J.	Leung, I.	Slattery, R.L.
Brogan, W.T.	Lowney, S.D.	Withers, R.S.
Dolat, V.S.	Macedo, E.M., Jr.	Wright, P.V.
Fischer, J.H.	Macropoulos, W.	Yao, I.
Fitch, G.L.*	Melngailis, J.†	

MICROELECTRONICS

W.T. Lindley, Leader
F.J. Bachner, Associate Leader
N.P. Economou, Assistant Leader
R.A. Murphy, Assistant Leader

Bozler, C.O.	Flanders, D.C.	Nichols, K.B.
Bromley, E.I.	Gatley, J.S.*	Pang, S.W.
Burke, B.E.	Geis, M.W.	Piacentini, W.J.
Cabral, S.M.	Goeloe, G.T.§	Pichler, H.H.
Calawa, A.R.	Gray, R.V.	Rabe, S.†
Chiang, A.M.	Hansell, G.L.	Randall, J.N.
Chu, A.	Lincoln, G.A., Jr.	Rathman, D.D.
Clifton, B.J.	Lyszcza, T.M.	Reinold, J.H.*
Daniels, P.J.	Mahoney, L.J.	Shaver, D.C.
DeGraff, P.D.	Manfra, M.J.	Silversmith, D.J.
Durant, G.L.	McClelland, R.W.	Smythe, D.L., Jr.
Efremow, N.N., Jr.	McGonagle, W.H.	Vigilante, J.L.
Elta, M.E.	Mountain, R.W.	Vojak, B.A.
Felton, B.J.	Mroczkowski, I.H.	Wilde, R.E.

*Co-op Student

†Part Time

§Staff Associate

¶Research Assistant

I. SOLID STATE DEVICE RESEARCH

A. EXCESS NOISE FACTOR IN InP AVALANCHE PHOTODIODES

Measurements of the excess noise factor as a function of multiplication have been carried out in high-quantum efficiency p^+n-n^+ inverted-mesa InP avalanche photodiodes (APDs). The structure and parameters of the diodes are shown in Fig. I-1. The edge of the mesas were masked as described earlier¹ to prevent photon absorption in the exposed depletion region and in the p^+ -substrate near the junction. This ensures the nearly pure single-carrier injection (holes, in this case) necessary for accurate excess-noise-factor measurements.

The noise power of the APD as a function of multiplication M was measured at several frequencies and varying levels of illumination by means of a sensitive spectrum analyzer preceded by low-noise transimpedance amplifiers. The excess noise factor F was calculated from the expression $F = I_n^2 / 2eBI_{po} M^2$, where I_n^2 is the measured mean square noise current added by the light, M is the concurrently measured gain, I_{po} is the primary photocurrent, and B is the bandwidth. The results are shown in Fig. I-2. The solid curves were calculated from the theoretical expression of McIntyre²: $F(M) = M[1 - (1 - k_{eff})(1 - M)^2/M^2]$, where k_{eff} is the effective ratio of the field-dependent electron and hole ionization coefficients. It is clear from the figure that the experimental data do not correspond to a single value of k_{eff} over the entire range of multiplication. Low values of F , consistent with a k_{eff} of 0.02 to 0.1, are found for $M \lesssim 10$; but for higher values of M , F increases more rapidly than expected even from the field-dependent McIntyre theory. This result does not agree well with reported noise measurements on diffused-junction devices,^{3,4} which yield $k_{eff} \sim 0.4$ to 0.6 for $M \lesssim 40$, but is in reasonable agreement with data obtained recently⁵ on grown-junction APDs. There is also excellent agreement between the results described here and those obtained previously on InP/GaInAsP heterostructure devices, with separate collection and multiplication regions in which the $p-n$ junction is in the InP (Refs. 6 and 7). These results are

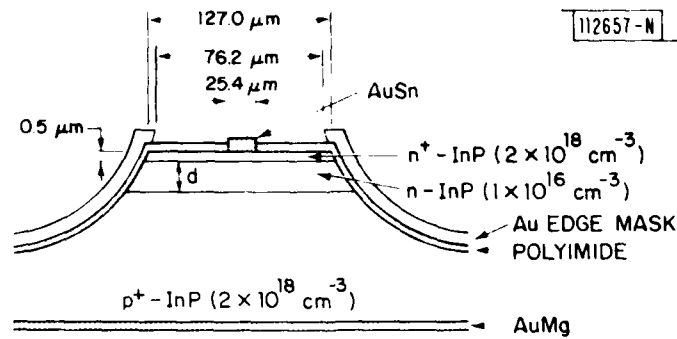


Fig. I-1. InP avalanche photodiode structure and parameters. The n-InP layer thickness d was $5 \mu\text{m}$, and quantum efficiency 60 percent. An edge-mask prevents light incident on mesa sides.

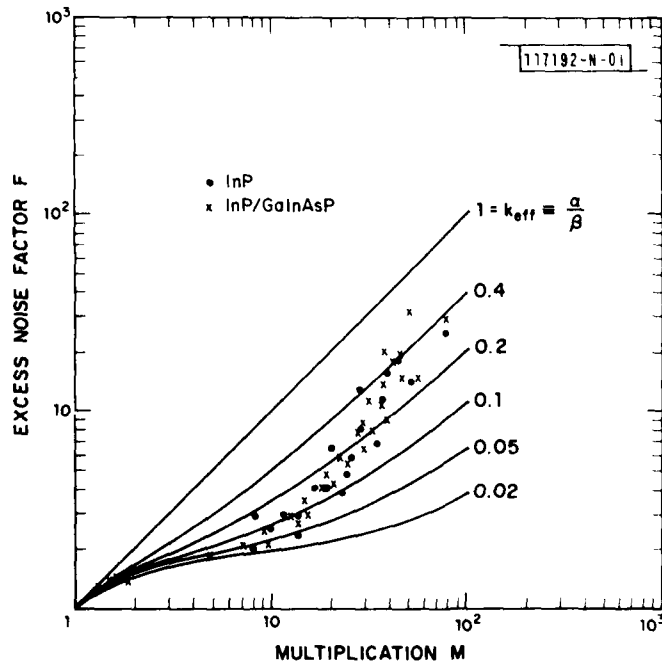


Fig. I-2. Experimental excess noise factor vs multiplication obtained from InP APDs and InP/GaInAsP heterostructure devices described earlier.^{6,7} Solid curves are calculated from McIntyre's noise theory.²

also shown in Fig. I-2 for comparison. The strong similarity in the magnitude and functional behavior of $F(M)$ for both the simple InP and the composite GaInAsP/InP devices implies that the noise characteristics of the latter are determined by the InP p-n junction rather than the narrow-gap material or the heterointerface.

Using a statistical approach, Van Vliet⁸ has developed a model to describe avalanche noise which differs from McIntyre's theory in that only a finite number N of possible ionizing events are allowed per pass of a carrier through the depletion region. The excess noise factor determined from this model is shown as the solid curve in Fig. I-3. The discontinuities in the curve correspond to the values of M which have equal probabilities of being achieved with either N or $N + 1$ ionizations. This represents a piecewise

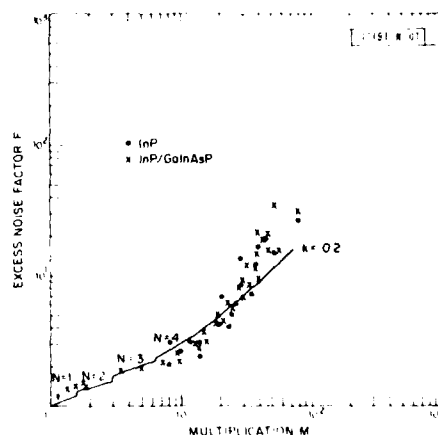


Fig. I-3. Excess noise factor vs multiplication calculated from Van Vliet's noise theory⁸ for $k = 0.2$. N is number of ionizations per carrier pass required to achieve a given value of M . Experimental data are same as in Fig. I-2.

approximation to the continuous behavior that would be expected experimentally. The theoretical curve shown in Fig. I-3 represents the best fit to the data of Fig. I-2 and corresponds to a value of k which is approximately 0.2. Theory is in reasonably good agreement with the experimental data for $M \lesssim 10$ but, as in the case of the McIntyre model, the rapid rise in F for the higher values of M is again not predicted.

The fact that the measured excess noise factor $F(M)$ for $M < 10$ agrees reasonably well with McIntyre's theory with $k_{\text{eff}} = 0.02$ to 0.1, or Van Vliet's model with $k = 0.2$, makes it clear that the value of the ratio of the ionization coefficients obtained from noise data is very dependent on the model being employed and is therefore open to question. In evaluating receiver performance, however, the measured noise power and calculated resulting excess noise factor are the important quantities, and these values are desirably low for moderate values of gain in both the InP and GaInAsP/InP APDs.

V. Diadiuk
S.H. Groves
C.E. Hurwitz

B. THRESHOLD CHARACTERISTICS OF GaInAsP/InP DOUBLE HETEROSTRUCTURE LASERS

There have been a number of investigations⁹⁻¹³ on the threshold current densities of GaInAsP/InP double heterostructure lasers with emission wavelengths near 1.3 μm . However, the reported data were generally scattered over a wide range, making their physical interpretation less certain. In this work we have attempted a systematic study, with special attention directed toward uniformity within a wafer and accuracy in the measurement of active-layer thickness.

The double heterostructure laser wafers were grown by conventional liquid-phase epitaxial growth techniques on Sn-doped ($n \approx 1 \times 10^{18} \text{ cm}^{-3}$) (100) InP substrates.¹⁴ Some experiments on growth temperature and time were

carried out to assure uniform thickness and good surface morphology in the InP buffer and cap layers. Broad-area lasers $\sim 200 \mu\text{m}$ in width and $\sim 500 \mu\text{m}$ in length were fabricated by plated and alloyed Au/Zn/Au and Au/Sn/Au contacts to the p-type InP cap layer and n-type InP substrates, respectively, followed by cleaving and saw-cutting. In addition to the room-temperature pulsed threshold current density J_{th} , the active-layer thickness d was also measured for each individual laser diode by using a scanning electron microscope. To improve the measurement for devices with $d \leq 2000 \text{ \AA}$, the mirror facets were etched in an aqueous solution of $\text{K}_3\text{Fe}(\text{CN})_6$ and KOH in order to bring out the contrast between the $\text{Ga}_{0.27}\text{In}_{0.73}\text{As}_{0.63}\text{P}_{0.37}$ active layer and InP. The etching time was minimized to assure a negligible enhancement of the active-layer thickness.¹⁴

The devices fabricated from each wafer showed good uniformity in J_{th} , and only ~ 10 percent of the tested devices did not lase or had abnormally high J_{th} . Figure I-4 shows the plot of J_{th} vs d for laser diodes fabricated out of seven different wafers. The diode lengths (L 's) were typically between 440 and 550 μm . A "normalization" of each J_{th} to $L = 500 \mu\text{m}$ was carried out by using the averaged slope in the J_{th} vs $1/L$ plot. These corrections resulted in less than 4-percent change in the values of J_{th} . The wafer with best uniformity was LPE 324, in which only one device did not lase out of 30 tested. Moreover, 25 of the devices had J_{th} values within ± 10 percent of their average. This wafer also had a very uniform active-layer thickness, as shown in Fig. I-4.

Figure I-5 shows the normalized threshold current density J_{th}/d plotted vs d for lasers of thicker active layers. In this figure, J_{th}/d decreases approximately 10 percent when d increases from 0.45 to 1.1 μm . This could be due to more reabsorption of spontaneous photons by thicker active layers.¹⁵⁻¹⁷

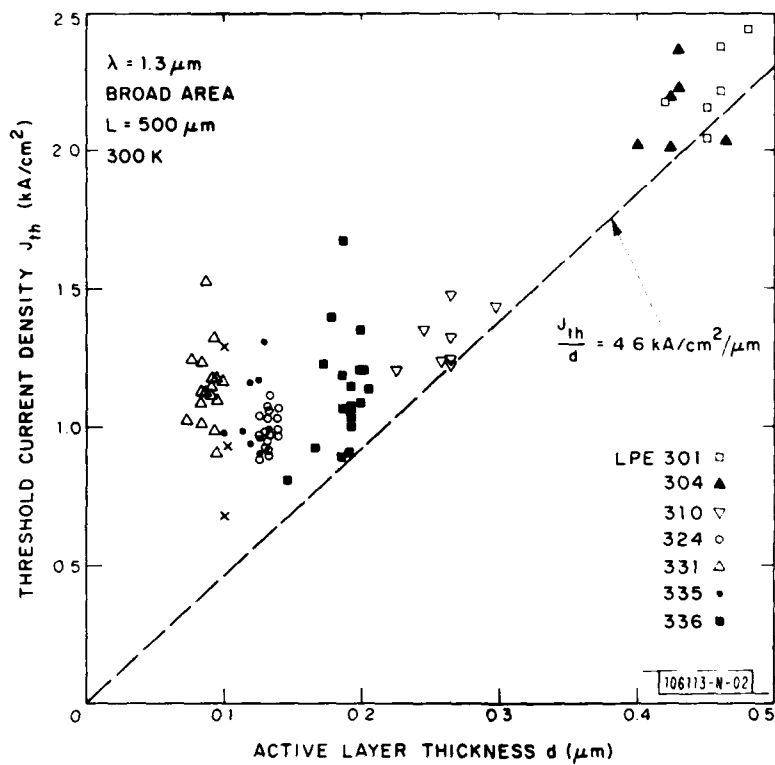
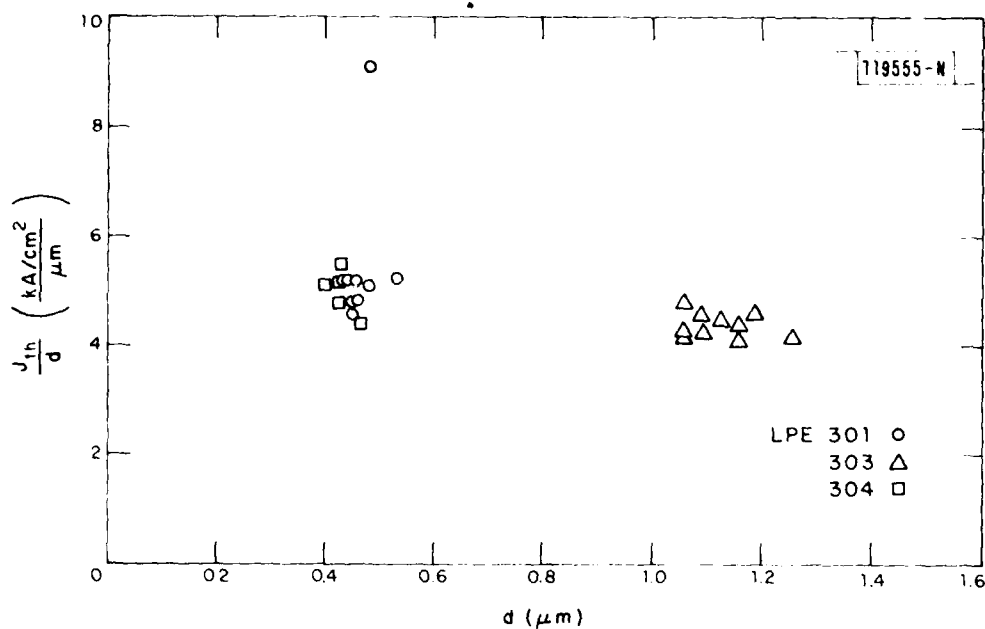


Fig. I-4. Plot of threshold current density vs active-layer thickness for GaInAsP/InP double heterostructure lasers fabricated from seven different wafers.



The low J_{th} values obtained in this work are comparable to those of Itaya et al.¹⁰ and Greene and Henshall,¹¹ and are close to the lowest (0.67 kA/cm²) reported by Nelson.¹² The wafer uniformity achieved in this work appears to be better than those previously reported.⁹⁻¹³ Furthermore, buried heterostructure lasers fabricated out of similar wafers also showed low threshold currents (6.4 mA) and high yield.¹⁸

C. BERYLLIUM-IMPLANTED GaInAsP/InP DOUBLE HETEROJUNCTION LASER DIODES

system.^{19,20} In this section, the use of Be implantation to fabricate broad-area GaInAsP/InP double heterojunction laser diodes operating at 1.3 μm is reported. The use of implantation rather than simple diffusion could lead to greater flexibility in and control of doping for new, integrated laser structures. These lasers have threshold current densities comparable to those obtained using conventional Zn doping during the epitaxial growth of the InP cap layer.

The samples used in these experiments were standard InP/GaInAsP/InP double heterojunction wafers grown by liquid phase epitaxy (LPE). Starting with an n^+ -InP substrate, a tin-doped InP buffer layer with a carrier concentration of about $2 \times 10^{18} \text{ cm}^{-3}$ was grown first. This was followed by a GaInAsP active layer and an InP cap layer, both of which were n-type with a carrier concentration of $(1 \text{ to } 2) \times 10^{17} \text{ cm}^{-3}$.

Although the results are not as well documented as for GaAs (see Refs. 21 through 23), it has been reported that implanted Be in InP also has a concentration-dependent diffusion coefficient.^{24,25} If the Be concentration is kept below $(2 \text{ to } 3) \times 10^{18} \text{ cm}^{-3}$, the resulting p-n junctions are at a depth expected from LSS range theory.²⁶⁻²⁸ For high Be concentrations, the junctions are appreciably deeper than expected and the depth increases with implant dose and implant temperature.²⁴

To investigate the effects of this concentration-dependent diffusion on laser performance, two basically different Be-implant schedules were used in these experiments: one that results in minimal diffusion of the implanted Be, and one that results in junctions $\approx 1.0 \mu\text{m}$ deeper than expected from LSS range theory.²⁶⁻²⁸ The Be-implantation schedule used that results in minimal diffusion was $5.0 \times 10^{13} \text{ cm}^{-2}$ at 400 keV, $3.5 \times 10^{13} \text{ cm}^{-2}$ at 200 keV, and $8.0 \times 10^{13} \text{ cm}^{-2}$ at 30 keV. This schedule results in a hi-lo profile which was chosen to provide the highest possible Be concentration near the surface consistent with minimal diffusion for contacting, but a lower concentration near the active layer to minimize free-carrier absorption. For the p-n junction to be at the InP-GaInAsP interface or in the quaternary, the InP cap

should be ≈ 1.5 to $1.7 \mu\text{m}$ thick for a background carrier concentration of $(1 \text{ to } 2) \times 10^{17} \text{ cm}^{-3}$. Implantations using this "nondiffused" Be schedule were carried out with the GaInAsP/InP samples at either room temperature or 150°C .

For "diffused" Be-implanted lasers, a Be-implantation schedule which results in a flat LSS profile of $1 \times 10^{19} \text{ cm}^{-3}$ and a LSS junction depth about $1.0 \mu\text{m}$ less than the InP cap thickness was used. For this high concentration implant, the Be diffused sufficiently during the post-implantation anneal to result in a p-n junction at the hetero-interface or slightly into the GaInAsP layer. Samples were held at 150°C during implantation with a diffused implant schedule.

After implantation, all the samples were annealed at 750°C for 10 min. using a phosphosilicate glass (PSG) encapsulation plus a PH_3 overpressure.^{24,29} Following contacting, laser diodes approximately $200 \times 500 \mu\text{m}$ in size with sawed sides and cleaved end faces were made from each wafer. The cap and active-layer thicknesses of each wafer were determined using both optical and scanning-electron-beam (SEM) microscopy. Electron-beam-induced-current (EBIC) measurements were used to determine the position of the p-n junction. On several wafers, an SEM was used to determine cap and active-layer thicknesses on the individual laser diodes after threshold-current measurements were completed.

Capacitance-voltage measurements indicate that samples implanted with the nondiffused Be-implant schedule have fairly abrupt junctions, while samples implanted with a diffused Be-implant schedule have linearly graded junctions. These results differ from those in GaAs (Ref. 23) where Be-implanted profiles generally become sharper (i.e., more abrupt) on diffusion, but are consistent with those previously reported for InP (Ref. 25).

Threshold current densities of both nondiffused and diffused implanted lasers were comparable to those obtained using conventional Zn doping. The relative power output vs current of a typical laser is shown in Fig. I-6. This particular diode had a threshold current density of 2.2 kA/cm^2 and was from a wafer implanted at 150°C with the nondiffused Be-implant schedule. It

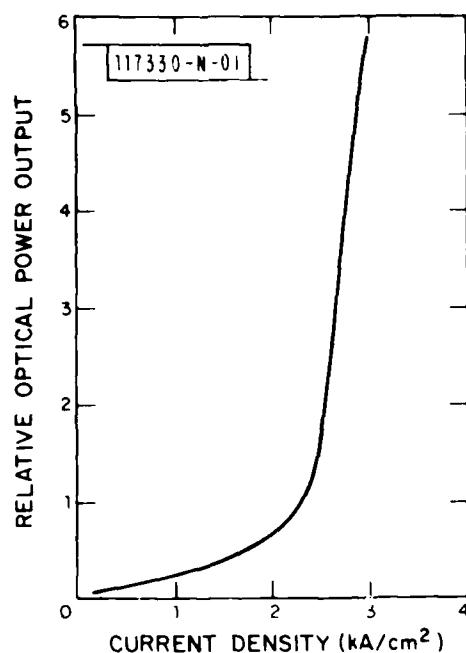


Fig. I-6. Relative power output vs current for a typical broad-area "nondiffused" Be-implanted GaInAsP/InP laser diode.

had a cap thickness of $1.5 \mu\text{m}$ and an active region thickness of $0.3 \mu\text{m}$. The threshold current densities of lasers from several wafers are plotted in Fig. I-7 as a function of active-layer thickness. The open symbols represent threshold current densities plotted at the average active-layer thickness measured on the wafer from which the laser was made, while the filled-in symbols represent those plotted at the active-layer thickness measured on the individual laser diode. The dashed line represents the best (i.e., lower-limit) threshold current density vs active-layer thickness achieved on lasers grown in the same LPE growth system using conventional Zn doping during the growth of the InP cap layer. The nominal threshold current density ($J_{\text{nom}} = J_{\text{th}}/d$, where J_{th} is the threshold current density and d is the active-layer thickness) obtained from the slope of this line is $4.6 \text{ kA/cm}^2/\mu\text{m}$ and is representative of the current state of the art of broad-area lasers in the GaInAsP/InP material system (see Sec. B above). The lowest threshold current density measured in an implanted laser was 1.2 kA/cm^2 , corresponding to a

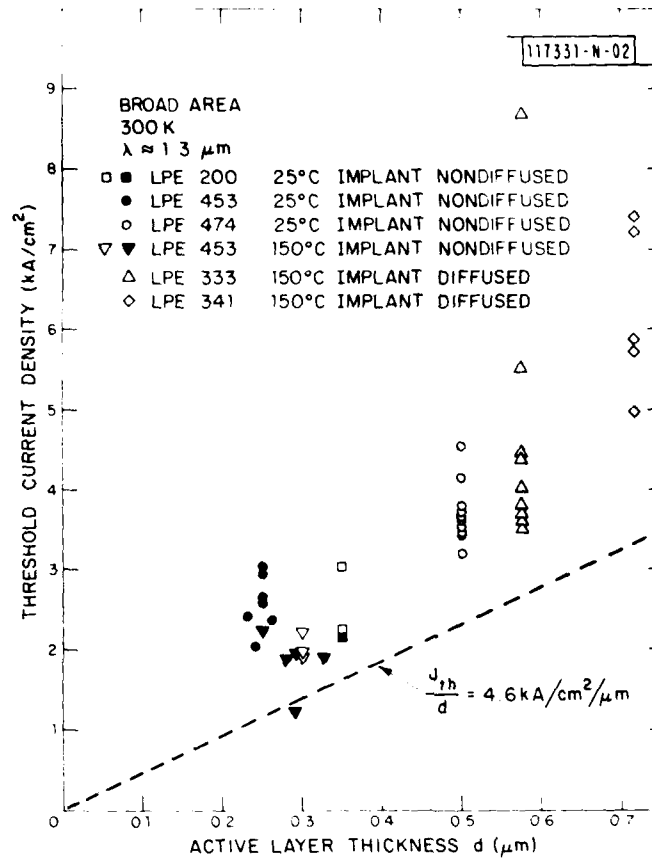


Fig. I-7. Threshold current densities of broad-area Be-implanted GaInAsP/InP double heterojunction lasers plotted as a function of active-layer thicknesses. Dashed line represents best current threshold densities achieved on lasers grown in same LPE system using conventional Zn doping during epitaxial growth.

$J_{\text{nom}} = 4.2 \text{ kA/cm}^2/\mu\text{m}$. A more typical lower value of J_{th} on wafers with thin active layers (0.25 to 0.35 μm) was 2.0 kA/cm^2 . On most wafers, the majority of lasers had a nominal threshold current density within a factor of two of $4.6 \text{ kA/cm}^2/\mu\text{m}$. Although lasers implanted with the nondiffused Be-implant schedule have had slightly lower nominal threshold densities than those implanted with the diffused schedule, the data are not sufficient to permit any definite conclusions at this time.

The thickness of the InP cap and the uniformity of this layer are important parameters which must be controlled in order to achieve reproducible results. This is especially true for lasers implanted with the nondiffused Be-implant schedule. For a given maximum implant energy, if the cap layer is too thick the implanted p-n junction will be in the top InP layer, resulting in either high threshold current densities or no lasing at all. Cap layers with nonuniform thicknesses result in variations in the position of the p-n junction, which can lead to nonuniform injection and wide variations in threshold current densities. Nonuniform thicknesses are likely the more serious problem since cap layers which are uniform but too thick can be etched to the desired thicknesses. Since the position of the p-n junction is also determined by the background carrier concentrations in the cap, variations in this parameter can have the same effects.

A SEM micrograph of the cleaved face of a laser diode implanted at room temperature with the nondiffused Be-implant schedule is shown in Fig. I-8. Superimposed on the micrograph is the diode's EBIC response, which indicates that the p-n junction of this laser is actually in the InP, but within 0.3 μm of the heterojunction interface. This laser (taken from wafer LPE 200) had a cap thickness of about 1.9 μm and an active-layer thickness of 0.35 μm . Even with the junction in the InP, the threshold current density of this laser was 2.3 kA/cm^2 . Other samples implanted with the nondiffused implant schedule had cap thicknesses of 1.5 to 1.6 μm and junctions nominally at the heterojunction interface. The InP cap layer, however, cannot be made arbitrarily thin. An increase in threshold current density can occur as the cap layer thickness is decreased due to the tails of the guided optical mode

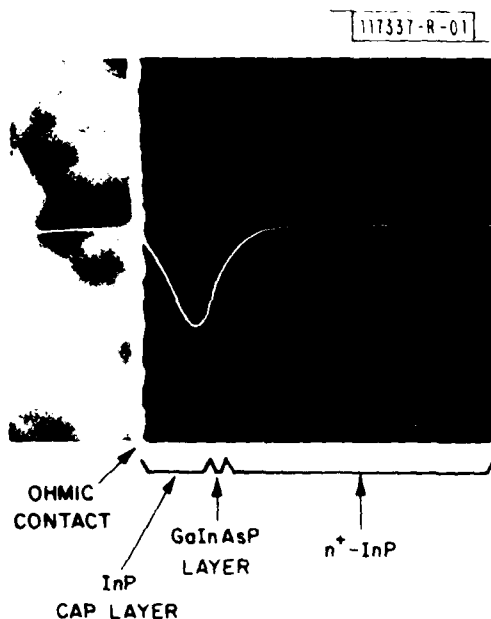


Fig. I-8. A SEM micrograph of a cleaved Be-implanted nondiffused GaInAsP/InP laser diode fabricated in a wafer with a 1.9- μm cap layer and a 0.35- μm active layer. Superimposed on SEM is EBIC response which shows that p-n junction lies in InP cap layer. Even with p-n junction in cap layer, this particular laser had a threshold current density of 2.3 kA/cm^2 .

penetrating to the p-type ohmic contact. Some increase in threshold current density due to this effect is very likely occurring on the nondiffused lasers, with active layers less than 0.35 μm reported in this section. If the background carrier concentration of the InP cap was reduced to 10^{16} cm^{-3} or less, a cap thickness of about 2.0 μm could be used without any change in implant parameters. Higher-energy Be implants would also permit the use of thicker cap layers.

Thicker cap layers have been used for the Be-implanted diffused lasers. The diffused wafers for which data are plotted in Fig. I-7 had cap thicknesses of 2.5 μm (LPE 333) and 3.0 μm (LPE 341). The Be-implant schedule used for sample LPE 333 had a maximum Be energy of 280 keV, while that used

for LPE 341 had a maximum energy of 400 keV. The resultant p-n junction on both samples due to diffusion during the anneal was nominally at the heterojunction interface.

J.P. Donnelly
J.N. Walpole
Z.L. Liao

D. A SLOW SELECTIVE ETCH FOR GaInAsP GROWN ON InP

The technology for fabricating laser diodes, detectors, and optical waveguides in GaInAsP/InP epitaxial wafers requires the use of suitable etching techniques for providing smooth, damage-free surfaces, precise pattern geometries, and preferential and reproducible removal of specific layers. Several previous publications have reported slow, controllable etches for InP (Refs. 30 through 33) and etches for selectively removing InP layers grown over GaInAsP (Ref. 34). Little has been reported on slow etches for GaInAsP or on selectively etching GaInAsP on InP. Here we describe etch rate and surface morphology results obtained using a dilute sulfuric acid, hydrogen peroxide, and water etch, which has proven to be a slow selective etch for GaInAsP.

The samples used in these experiments were (100) LPE-grown GaInAsP/In heterojunction wafers in which the quaternary composition was either $\text{Ga}_{0.27}\text{In}_{0.73}\text{As}_{0.63}\text{P}_{0.37}$ [having a bandgap of 0.95 eV ($\lambda = 1.3 \mu\text{m}$)] or $\text{Ga}_{0.10}\text{In}_{0.90}\text{As}_{0.04}\text{P}_{0.96}$ [having a bandgap of 1.24 eV ($\lambda = 1 \mu\text{m}$)]. Each etch solution used was placed in a clean 200-ml pyrex beaker which was modified for mounting a microscope slide inside. The solution was stirred continuously by means of a Teflon-coated magnetic stirrer. Part of each sample to be etched was masked with SiO_2 to provide a step in order to measure etch depth. For etching, the sample was mounted on a microscope slide using apiezon wax. After etching, the mask was removed, and the sample was rinsed, dried, and inspected. The etch depth was measured with a Dek-tak surface profiler.

Slow controllable etches suitable for removing thin layers of InP are generally not usable with GaInAsP. For example, we have found that iodic acid etches³¹ GaInAsP in a nonuniform manner, leaving very badly pitted surfaces. Potassium-ferrocyanide potassium-hydroxide solutions, which are often used to delineate p-n junctions in the III-V compounds, etch GaInAsP faster than InP and have been used as a selective etch.¹⁸ The selectivity, however, depends on the doping of the InP as well as the composition of the etch solution.

Sulfuric acid-peroxide-based etches, which are commonly used as fast-polishing etches for GaAs, etch InP only slowly.³⁵ For example, we have found that a 3 H₂SO₄:1 H₂O₂:1 H₂O solution at room temperature etches InP at about 200 Å/min. By decreasing the volume of H₂SO₄ and increasing that of water, the etch rate in InP can be reduced to a negligible value while maintaining a reasonable etch rate for most GaInAsP lattice-matched compositions, except those very close to InP. As shown in Fig. I-9, a 1 H₂SO₄:1 H₂O₂:10 H₂O room-temperature solution etches (100) Ga_{0.27}In_{0.73}As_{0.63}P_{0.37} ($\lambda_g = 1.3 \mu\text{m}$) at a very constant etch rate of 1000 Å/min. The etched GaInAsP surface appeared to be free of any etch-related defects. Figure I-10 shows a photomicrograph of a double heterojunction wafer in which the top InP layer was removed from most of the wafer using concentrated HCl (a selective etch for InP). Different areas of the GaInAsP layer were then etched for different times using 1 H₂SO₄:1 H₂O₂:10 H₂O. The etched surfaces have the same surface texture as the originally exposed quaternary surface. For (100) Ga_{0.10}In_{0.90}As_{0.04}P_{0.96} ($\lambda_g = 1.04 \mu\text{m}$), the etch rate (see Fig. I-9) drops to about 75 Å/min. The etch depth on (100) InP could not be measured after an hour's etch time although a fine demarcation line between the etched and unetched areas of the samples was observed. The surface quality of the InP exposed to the dilute sulfuric acid etch was good (see InP surface in Fig. I-10, which was exposed

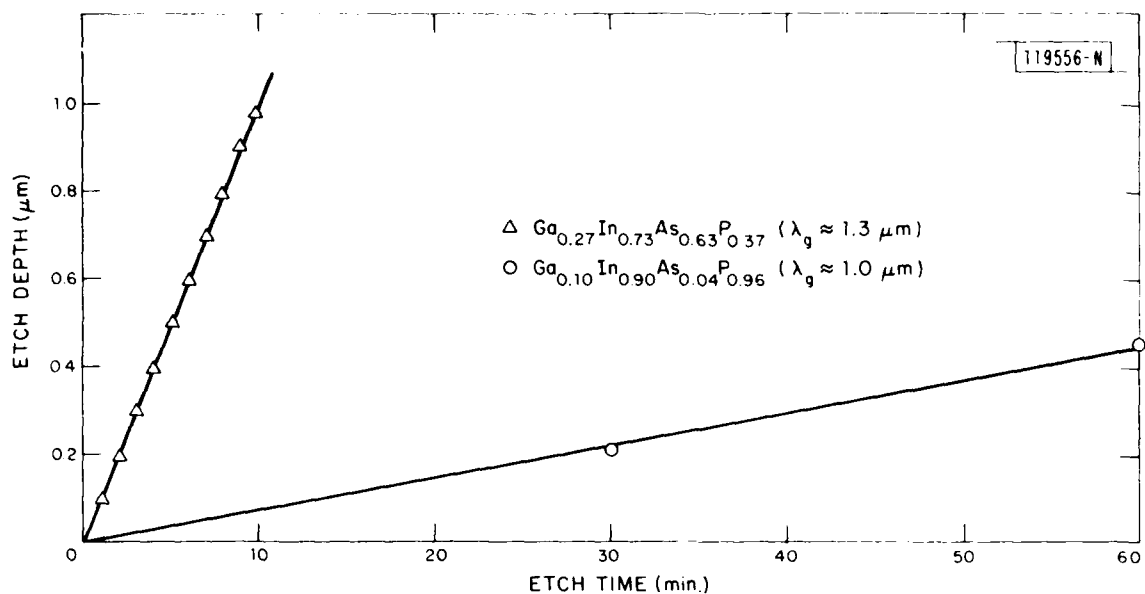


Fig. I-9. Etch depth vs etch time obtained on a $\text{Ga}_{0.27}\text{In}_{0.73}\text{As}_{0.63}\text{P}_{0.37}$ and a $\text{Ga}_{0.10}\text{In}_{0.90}\text{As}_{0.04}\text{P}_{0.96}$ layer etched in a room-temperature $1 \text{ H}_2\text{SO}_4 : 1 \text{ H}_2\text{O}_2 : 10 \text{ H}_2\text{O}$ solution.

to the dilute sulfuric acid etch). The same result was obtained on (100)-oriented liquid encapsulated Czochralski (LEC) InP samples doped with either Zn and Sn to concentrations greater than 10^{18} cm^{-3} . Various dilutions of $\text{H}_2\text{SO}_4:\text{H}_2\text{O}_2:\text{H}_2\text{O}$ should prove useful as slow selective etches for GaInAsP in a variety of applications.

G.A. Ferrante
J.P. Donnelly

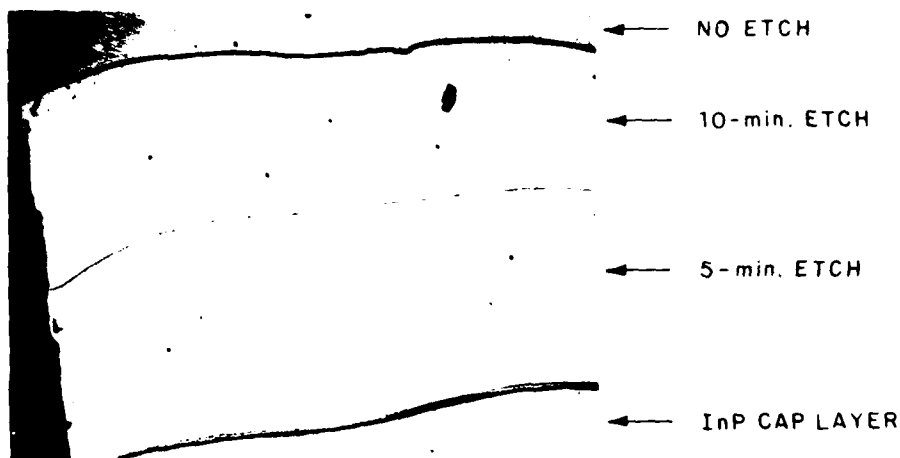


Fig. I-10. Photomicrograph of a $\text{Ga}_{0.27}\text{In}_{0.73}\text{As}_{0.63}\text{P}_{0.37}/\text{InP}$ double heterojunction wafer in which most of top InP was removed in concentrated HCl and different areas of quaternary layer etched for times indicated (no etch, 5-min. etch, and 10-min. etch) in a $1 \text{ H}_2\text{SO}_4 : 1 \text{ H}_2\text{O}_2 : 10 \text{ H}_2\text{O}$ solution.

REFERENCES

1. Solid State Research Report, Lincoln Laboratory, M.I.T. (1981:4), p. 3, DTIC AD-A114189.
2. R.J. McIntyre, IEEE Trans. Electron Devices ED-19, 703 (1972).
3. S.R. Forrest, G.F. Williams, O.K. Kim, and R.G. Smith, Electron. Lett. 17, 917 (1981).
4. T. Shirai, F. Osaka, S. Yamasaki, T. Kaneda, and N. Susa, Appl. Phys. Lett. 39, 168 (1981).
5. G.E. Bulman, L.W. Cook, M.M. Tashima, and G.E. Stillman, Proc. IEDM '81, p. 126 (1981).
6. Solid State Research Report, Lincoln Laboratory, M.I.T. (1979:4), p. 9, DDC AD-A084271/6.

7. V. Diadiuk, S.H. Groves, C.E. Hurwitz, and G.W. Iseler, IEEE J. Quantum Electron. QE-17, 260 (1981), DTIC AD-A102921/4.
8. K.M. Van Vliet, A. Friedmann, and L.M. Rucker, IEEE Trans. Electron Devices ED-26, 752 (1979).
9. R.E. Nahory and M.A. Pollack, Electron Lett. 14, 727 (1978); R.E. Nahory, M.A. Pollack, and J.C. DeWinter, Electron. Lett. 15, 695 (1979).
10. Y. Itaya, Y. Suematsu, S. Katayama, K. Kishino, and S. Arai, Jap. J. Appl. Phys. 18, 1795 (1979).
11. P.D. Greene and G.D. Henshall, Solid-State and Electron Devices 3, 174 (1979).
12. R.J. Nelson, Appl. Phys. Lett. 35, 654 (1979).
13. N. Tamari and A.A. Ballman, Appl. Phys. Lett. 39, 185 (1981); N. Tamari, Appl. Phys. Lett. 39, 792 (1981).
14. Solid State Research Report, Lincoln Laboratory, M.I.T. (1981:1), p. 7, DTIC AD-A103887/6.
15. F. Stern and J.M. Woodall, J. Appl. Phys. 45, 3904 (1974).
16. P. Asbeck, J. Appl. Phys. 48, 820 (1977).
17. Solid State Research Report, Lincoln Laboratory, M.I.T. (1980:3), p. 4, DTIC AD-A094075/9.
18. Z.L. Liao and J.N. Walpole, Appl. Phys. Lett. 40, 568 (1982).
19. N. Bar-Chaim, M. Lanir, S. Margalit, I. Ury, D. Wilt, M. Yust, and A. Yariv, Appl. Phys. Lett. 36, 233 (1980).
20. D. Wilt, N. Bar-Chaim, S. Margalit, I. Ury, M. Yust, and A. Yariv, IEEE J. Quantum Electron. QE-16, 390 (1980).
21. J.P. Donnelly, F.J. Leonberger, and C.O. Bozler, Appl. Phys. Lett. 28, 706 (1976), DDC AD-A028457/0.
22. W.V. McLevige, M.J. Helix, K.V. Vaidyanathan, and B.G. Streetman, J. Appl. Phys. 48, 3342 (1977).
23. M.J. Helix, K.V. Vaidyanathan, and B.G. Streetman, IEEE J. Solid State Circuits SC-13, 426 (1978).

24. J.P. Donnelly and C.A. Armiento, Appl. Phys. Lett. 34, 96 (1979), DDC AD-A069910/8.
25. W.T. Devlin, K.T. Ip, D.P. Leta, L.F. Eastman, and G.W. Morrison, in Gallium Arsenide and Related Compounds (1978), edited by C.M. Wolfe (Institute of Physics, London, 1979), Conf. Ser. 45, p. 510.
26. W.S. Johnson and J.F. Gibbons, Projected Range Statistics in Semiconductors (Stanford University Bookstore, 1970); also, J.F. Gibbons, W.S. Johnson, and S.W. Maglorgie, Projected Range Statistics (Halsted Press, New York, 1975).
27. J. Lindhard, M. Scharff, and H. Schiott, Mat. Fys. Metal Dar. Vad. Salal. 33, 1 (1963).
28. Only the projected range and projected standard deviation were used to determine the approximated as-implanted profiles.
29. J.P. Donnelly and C.E. Hurwitz, Appl. Phys. Lett. 31, 418 (1977), DDC AD-A050856/4.
30. R. Becker, Solid State Electron. 16, 1241 (1973).
31. A.R. Clawson, D.A. Collins, D.I. Elder, and T.J. Monroe, NOSC Technical Note 592, Naval Ocean Systems Center, San Diego, California (13 December 1978).
32. S. Adachi and H. Kawaguchi, J. Electrochem. Soc. 128, 1342 (1981).
33. S. Adachi, H. Kawaguchi, and G. Iwane, J. Mater. Sci. 16, 2449 (1981).
34. S.B. Phatak and G. Kelner, J. Electrochem. Soc. 126, 287 (1979).
35. Y. Nishitani and T. Kotani, J. Electrochem. Soc. 126, 2269 (1979).

II. QUANTUM ELECTRONICS

A. EFFECTS OF TEMPORAL CORRELATION ON SIGNAL AVERAGING OF LIDAR MEASUREMENTS

The accuracy of the remote sensing of species in the atmosphere using a differential-absorption LIDAR (DIAL) system is dependent upon the determination of the value of the "on-resonance" DIAL return compared with the "off-resonance" value. The accuracy of such measurements can generally be improved by increasing the number of measurements and taking average values. An experiment is described in which the effect of averaging on the measurement uncertainty is measured, where the uncertainty is defined by the standard deviation of the mean value of the returns. The results show that the reduction of the standard deviation by signal averaging over increasing numbers of pulses is much smaller than would be anticipated for independent measurements, and is due to small but long-term temporal correlation. The results are shown to be in excellent agreement with a theoretical analysis that takes the correlation of successive LIDAR returns into account.

A dual mini-TEA CO₂ DIAL system was employed for the experiment.¹ The first of the two CO₂ lasers in the dual-laser system (laser 1) was fired on the P(28) laser transition, and 50 μ s later laser 2 was fired on the P(22) transition, both in the 10.6- μ m band. The atmosphere is effectively "frozen" over this time interval.² The laser outputs were directed along identical beam paths to a flame-sprayed aluminum plate at a range of 2.7 km, which served as a diffusely reflecting target. A total of 22,528 LIDAR return pulses from the target were recorded for each of the two lasers. The process took 40 min., corresponding to a pulse repetition frequency of slightly under 10 Hz. Because of computational constraints, analysis was limited to sets of 12,288 pulses from each laser. The initial and final sets of 12,288 pulses exhibited somewhat differing behavior. Therefore, a full analysis was carried out for these two sets of data. The statistical analysis of the two sets of LIDAR return data included a determination of the average value of each set of 12,288 pulses, the standard deviation of each set, and the

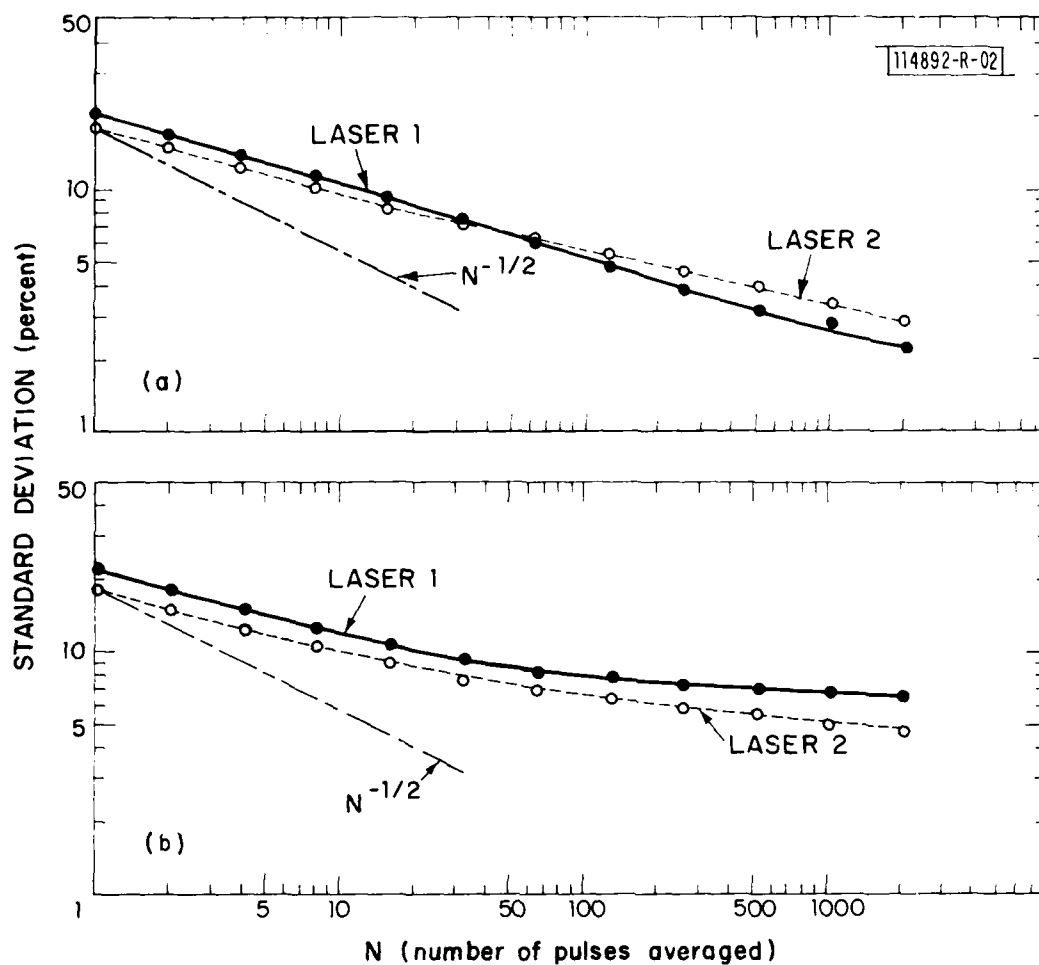


Fig. II-1. Measured percentage standard deviation of LIDAR return signals as a function of number of pulses averaged. Returns from lasers 1 and 2 for (a) initial set and (b) final set of 12,288 pulses, respectively.

normalized standard deviation of the average value of the LIDAR returns σ_N as a function of N , the number of pulses being averaged. The results for the initial and final sets of data are shown in Figs. II-1(a) and (b), respectively. The slower decrease of σ_N with increasing N for the LIDAR returns of the final set relative to the initial set has been shown to be attributable to a slow drift in atmospheric absorption which occurred during the period encompassed by the final set of data.³ In all the cases considered, it is seen that the variation of σ_N with N is significantly smaller than the $N^{-1/2}$ dependence predicted for independent measurements.

To evaluate the temporal correlation of the LIDAR pulse returns, let us define $I_k = I(t_k)$ as the normalized deviation of the k^{th} pulse return (occurring at time t_k) from its mean value \bar{P} over the full set of data. Then,

$$I_k = \frac{P_k - \bar{P}}{\bar{P}} \quad (\text{II-1})$$

where P_k is the k^{th} LIDAR pulse return signal. The normalized variance of the full set of individual pulses is defined as

$$\sigma^2 \equiv \langle (I_k)^2 \rangle = \frac{1}{\Gamma} \sum_{k=1}^{\Gamma} I_k^2 \quad (\text{II-2})$$

where Γ is the total number of pulses in the set (12,288). The temporal autocorrelation coefficient ρ_j for a delay time equal to $j\tau$ is then given by

$$\rho_j = \frac{1}{\sigma^2} \langle I(t_k) I(t_k + j\tau) \rangle = \frac{1}{\sigma^2(\Gamma - j)} \sum_{k=1}^{\Gamma-j} I_k I_{k+j} \quad (\text{II-3})$$

where τ is the time interval between pulses.

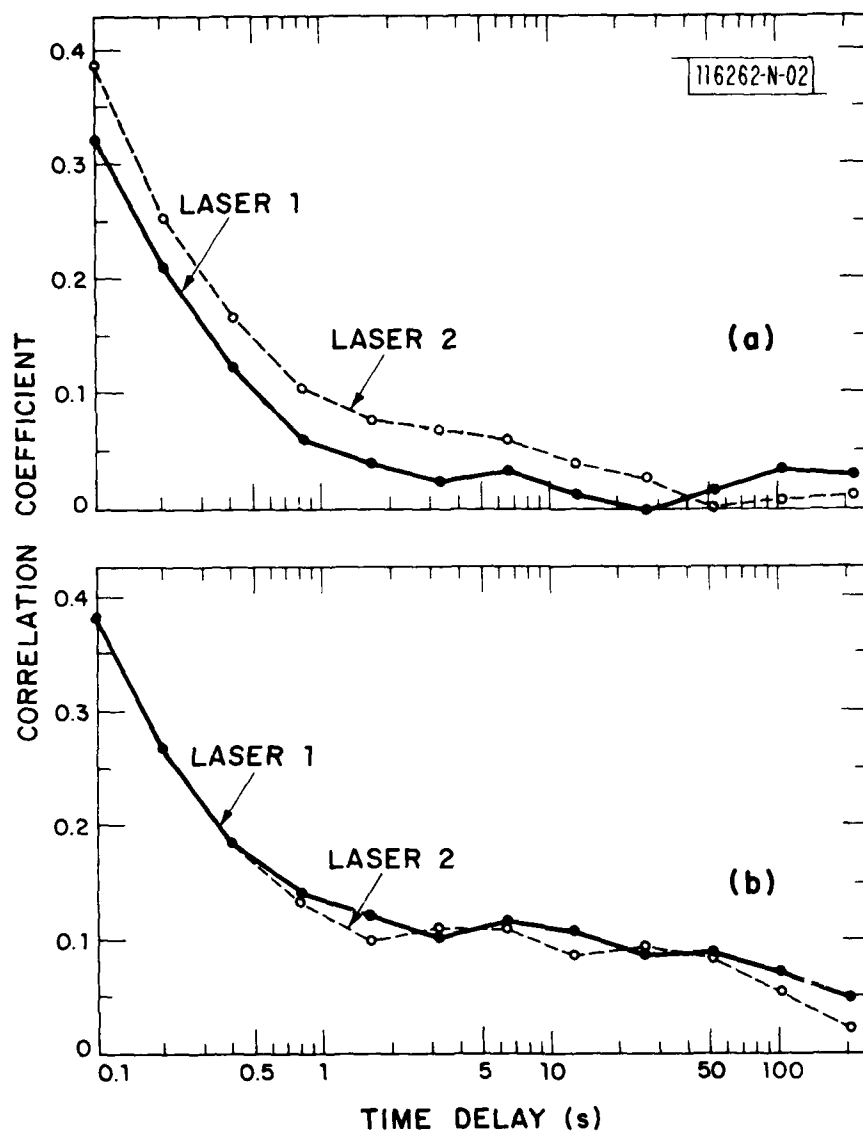


Fig. II-2. Correlation coefficient of LIDAR return signals from lasers 1 and 2 as a function of time delay between signals, based on a 10-Hz pulse-repetition rate. (a) Initial set and (b) final set of 12,288 pulses, respectively.

Equation (II-3) was used to calculate the correlation coefficient ρ_j for $j = 1, 2, 4, 8, \dots, 1024, 2048$, using the LIDAR pulse returns from L_1, L_2 and L_1/L_2 . The results are given in Figs. II-2(a) and (b) for the initial and final sets of data, respectively. It is seen from the figures that small positive temporal correlations persist in the first set out to 10 s and beyond, while the presence of a slow drift in the atmospheric absorption during the final set³ is seen to result in a larger positive correlation which persists beyond 200 s in the LIDAR returns.

Previous studies of the temporal correlation coefficient for backscattered CO_2 laser radiation through the atmosphere from a hard target have indicated that the atmosphere is effectively frozen for 1 to 5 ms, with a significant drop in correlation by 50 to 100 ms (see Refs. 2 and 4). However, residual positive correlation has been observed to persist out to several seconds.¹

The short-term correlation is primarily due to turbulence caused by thermal fluctuations in the atmosphere.⁵ For temporal correlations over the longer time intervals considered here, changes in absorption due to humidity fluctuations appear to play a significant role.³

To establish if the temporal correlation levels shown in Fig. II-2 are sufficient to cause the strong reduction in the effectiveness of pulse averaging relative to $N^{-1/2}$ behavior, the relationship between σ_N and ρ_j was derived. The derivation gave⁶

$$\sigma_N = \frac{\sigma}{\sqrt{N}} \left[1 + 2 \sum_{j=1}^{N-1} (1 - j/N) \rho_j \right]^{1/2} \quad (\text{II-4})$$

It should be noted that in the absence of correlation ($\rho_j = 0$), Eq. (II-4) predicts the expected $N^{-1/2}$ dependence. Values for σ_N were calculated on the basis of Eq. (II-4), using the values of ρ_j given in Figs. II-2(a) and (b) for $j = 1, 2, 4, 8, \dots, 1024, 2048$, and assuming a linear interpolation for all other values of j . The calculated values of σ_N for the LIDAR returns of laser 1 in both the initial and final sets of data are given in Table II-1. The corresponding measured values, as shown in Fig. II-1, are

TABLE II-1 PERCENTAGE STANDARD DEVIATION OF SIGNAL-AVERAGED LIDAR RETURNS FROM LASER 1				
N (No. of pulses averaged)	Initial Data Set		Final Data Set	
	Measured	Calculated	Measured	Calculated
1	20.5	-	21.7	-
2	16.7	16.7	18.0	18.0
4	13.7	13.7	15.1	15.1
8	11.2	11.2	12.8	12.9
16	9.0	9.1	10.9	11.1
32	7.2	7.3	9.5	9.7
64	5.8	5.8	8.5	8.6
128	4.6	4.8	7.9	8.0
256	3.7	4.0	7.5	7.6
512	3.0	3.0	7.2	7.2
1024	2.6	2.3	6.9	6.9
2048	2.3	2.6	6.3	6.5

also given in the table. The agreement between the calculated and the measured values of σ_N is seen to be excellent.

For the case of a constant value $\rho_j = \rho$, it has been found⁶ that in the limit for large values of N, Eq. (II-4) becomes

$$\sigma_N \approx \sigma\sqrt{\rho} \quad . \quad (II-5)$$

This situation is approximated experimentally when there is a continuous atmospheric drift throughout the measurement period, as was the case during the final set of data taken with lasers 1 and 2. As an example, using $\sigma = 0.22$ from Fig. II-1(b) and $\rho = 0.05$ from Fig. II-2(b), substitution into Eq. (II-5) leads to $\sigma_N \sim 0.05$. This result is consistent with the experimental data shown in Fig. II-1(b) and indicates that improvement in the standard deviation of the mean is limited in this case to a factor of ~ 4 , independent of the number of pulses averaged.

A more accurate approximation to the experimental results involves treating the temporal correlation ρ_j as a decreasing function of j ; a detailed analysis has been carried out for $\rho_j = e^{-j\alpha}$ and $\rho_j = A-B \ln(j)$, where α , A , and B are constants.⁶ On the basis of Eq. (II-5), it can be shown⁶ that if ρ_j is any monotonically decreasing or constant function of delay time, then

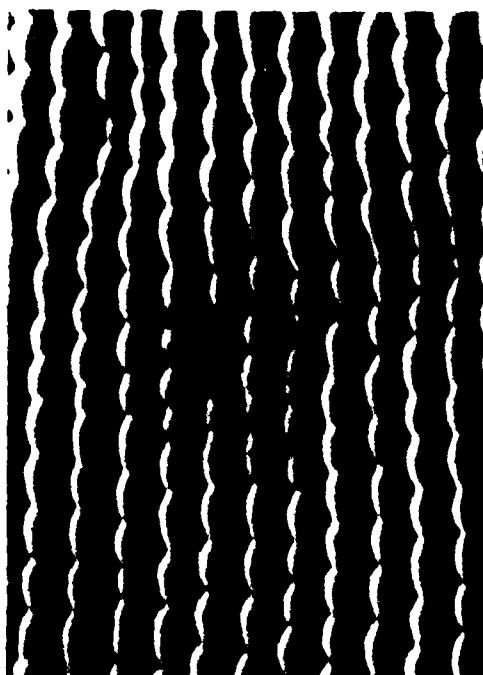
$$\sigma_N \geq \sigma \sqrt{\rho_{N-1}} \quad . \quad (II-6)$$

Equation (II-6) represents a fundamental inequality which can impose a severe limitation on the improvement attainable by averaging over a large sample. As long as the monotonically decreasing temporal correlation coefficient ρ_{N-1} has a finite value for a given time interval, that value limits the improvement in the standard deviation which can be obtained by signal averaging, regardless of the number of pulses averaged during that interval. For example, in the time interval required to bring the temporal correlation coefficient down to 1 percent, it is impossible for signal averaging to achieve more than a tenfold reduction in the standard deviation. It should further be noted that this degree of improvement occurs only for a constant correlation coefficient. For a decreasing ρ_j , the improvement can be significantly smaller.

It is apparent from the above considerations that very small temporal correlation values can severely limit the improvement achievable by signal averaging. This can be an important factor since our experimental data indicate that such small correlation values may persist over long time intervals, at least for LIDAR returns from a stationary target.

N. Menyuk
D.K. Killinger
C.R. Menyuk†

†University of Maryland, College Park, Maryland.



(a)



(b)

Fig. II-3. SEMs of ripple structure in an ~ 200 -nm-thick photodeposited Cd film on a SiO_2 substrate at viewing angles of (a) 60° and (b) normal incidence. A $1\text{-}\mu\text{m}$ scale (horizontal bar) and laser polarization direction are indicated.

B. STIMULATED SURFACE PLASMA WAVES AND THE GROWTH OF GRATING STRUCTURES IN LASER PHOTODEPOSITED METAL FILMS

Laser photodeposited Cd films exhibit high-frequency spatial structures with a period of the order of the UV-wavelength when grown under surface-dominated conditions.^{7,8} This surface structure is shown to be due to a stimulated surface plasma wave (SPW) scattering process. Initially, a weak SPW is excited by surface roughness-induced scattering from the incident field. The spatial modulation of the optical intensity resulting from the interference between the incident wave and the SPW promotes the growth of a periodic (ripple) structure, which increases the scattering into the SPW. There is a positive gain coefficient increasing both the amplitude of the film structure and SPW intensity for spatial frequencies ranging from approximately the incident light wave-vector to the SPW wave-vector. The process, which is analogous to stimulated Raman scattering where the grating structure plays the role of the material excitation and the SPW corresponds to the Stokes beam, is the first demonstration of an exponentially growing instability involving surface electromagnetic waves.

The films are deposited by CW UV laser photolysis of $\text{Cd}(\text{CH}_3)_2$ adsorbed on a smooth SiO_2 substrate surface. Scanning electron micrographs (SEMs) of a typical Cd film are shown in Figs. II-3(a) and (b). An extensive array of ripples extending over many optical wavelengths is apparent.

An SPW has a longitudinal electric field component; for normal incidence, the interference pattern between this field and the incident UV laser field gives rise to an intensity modulation at the film surface. Since the rate of adsorbed-layer photolysis is linearly related to the UV intensity, the film growth rate is also modulated. The resulting ripple structure scatters the incident field more strongly into the SPW mode and increases its field strength. For a range of spatial wave-vectors in the vicinity of the SPW wave-vector, the intensity modulation is in phase with the grating structure and an exponential growth results. Analytical results for the small signal gain as a function of spatial wave-vector q and of the film optical characteristics are shown in Fig. II-4. The dashed curve is

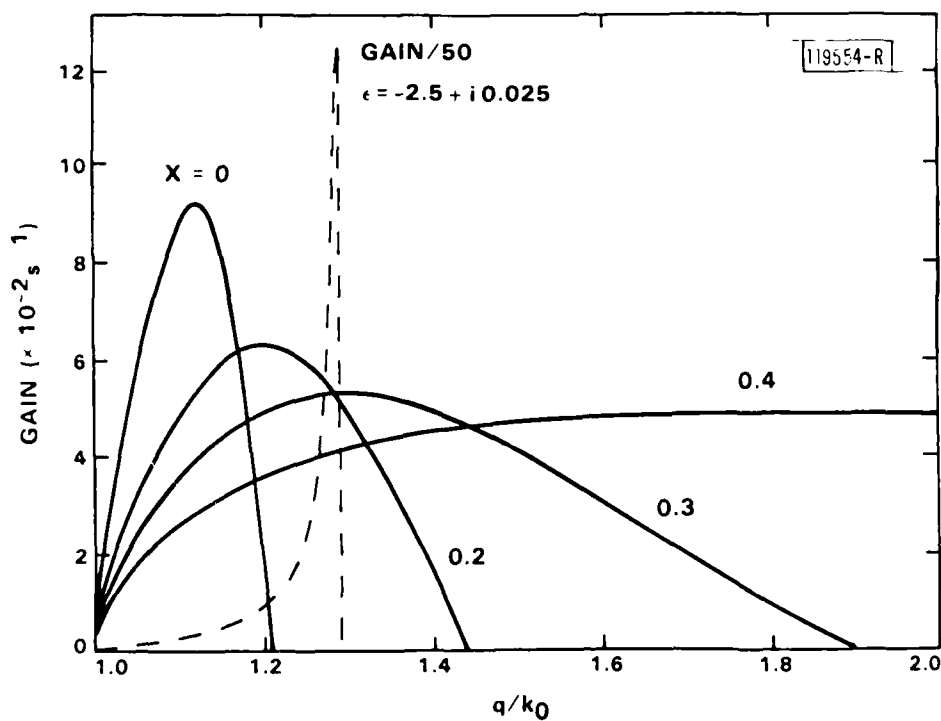


Fig. II-4. Calculated growth rates for surface grating structures of normalized spatial wave-vector q/k_0 . Dashed curve is for an idealized low-loss metal film. Solid curves are for granular Cd films, where X is volume fraction of voids.

for an idealized, almost lossless, metal film showing that the gain is sharply peaked near the surface plasma wave-vector $q_{sp} = 1.29 k_0$, where $k_0 = \omega/c$. The solid curves are calculated for realistic Cd film optical constants, derived for a granular Cd film using the Maxwell-Garnet theory of the optical constants of granular metals.⁹ In the figure, X is the volume fraction of voids in the film. Good agreement with the distribution of spatial frequencies in the actual film is obtained for $X \sim 0.4$. A more detailed discussion of this analysis will be presented elsewhere.¹⁰

Similar ripple phenomena are generally observed in a number of other laser-material systems including laser-annealing¹¹ and laser-damage.¹² Related physical effects are responsible for the formation of the ripple structures in these cases. Experiments are currently under way to probe the ripple-formation process in the pulsed-laser annealing of semiconductors. A good understanding of the process may ultimately be useful for directly producing large-area, submicrometer grating structures for semiconductor device applications.

S.R.J. Brueck
D.J. Ehrlich

C. HIGH-SPEED X-RAY-SENSITIVE InP PHOTOCONDUCTIVE DETECTORS

The use of photoconductive optoelectronic switches for high-speed optical detection has been reported in a number of recent publications. In particular, proton-bombarded InP photoconductive devices have recently been shown to have response times < 100 ps for 850-nm optical pulses and greater sensitivity than other comparably fast devices.¹³ This is a report on the performance of InP devices as fast detectors of pulsed x-ray radiation. In particular, it has been demonstrated that the devices have risetimes < 90 ps in the 9-keV x-ray region.

The devices consist of an array of interdigitated Ni/Ge/Au electrodes on an Fe-doped InP substrate which had a resistivity of $\sim 5 \times 10^7 \Omega\text{-cm}$. The electrode structure consisted of 2- μm -wide fingers and spaces, with an overall active area of $48 \times 48 \mu\text{m}$ (see Ref. 13).

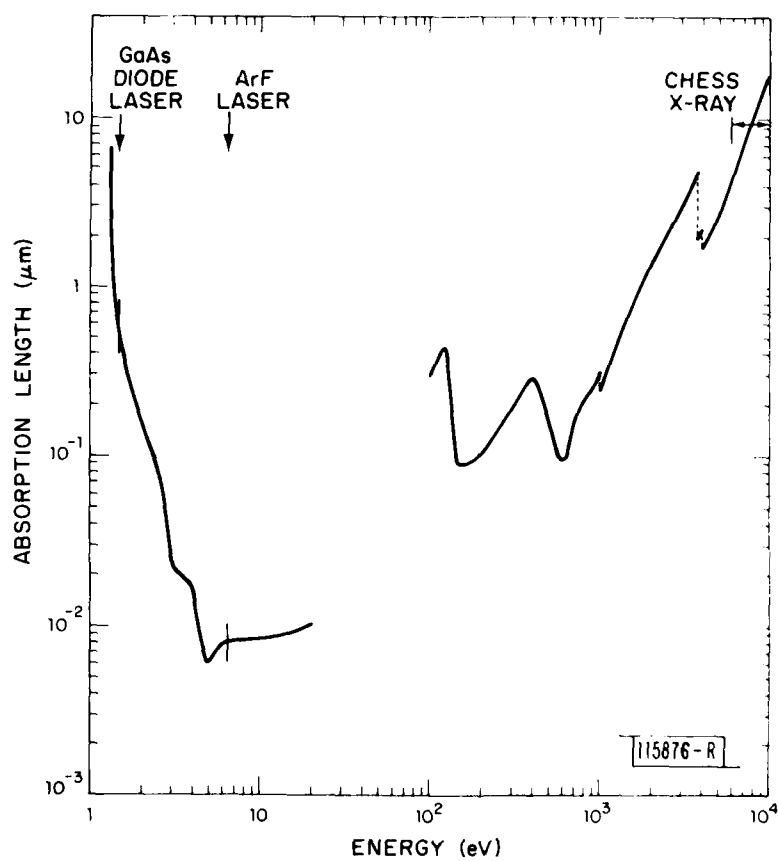


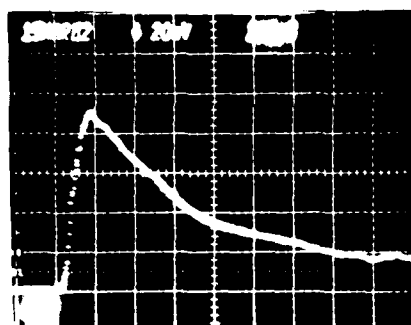
Fig. II-5. Absorption length vs photon energy for InP (see text).

Because these are surface-oriented photoconductors, with the photoconduction occurring between the interdigitated electrode fingers, only those carriers created in a depth approximately equal to the finger spacing contribute to the measured response. However, the penetration depth of the radiation sources used here varied from values much smaller than to much greater than the finger spacing, and this variation can have a significant effect on the performance of the device. Figure II-5 displays the absorption length $[(\text{absorption coefficient})^{-1}]$ of InP as a function of photon energy. The values for photon energies <20 eV were obtained from the literature.¹⁴ The values in the range 0.1 to 10 keV were calculated from the absorption coefficients for In and P, obtained from Atomic Data Tables,¹⁵ appropriately weighted. The curve shows that the absorption length varies by several decades over the wavelength range of interest, from ~ 0.6 μm at the 1.45-eV photon energy of the AlGaAs diode laser to <100 Å at the 6.4-eV photon energy of the ArF excimer laser, increasing to ~ 10 μm for 10-keV x-rays. This suggests that the InP detector may be relatively more sensitive to surface effects in those portions of the spectrum where the photoconductive effect is confined to a layer <0.1 μm beneath the surface.

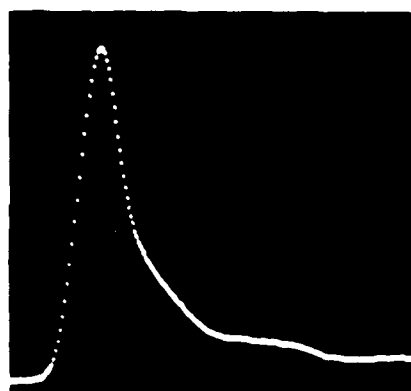
The measurements of response in the x-ray region, performed at the Cornell High Energy Synchrotron Source (CHESS), used a broadband pulsed beam of synchrotron radiation which had half-power points at 7 and 10 keV. The pulse repetition rate was 400 kHz and the pulse width, calculated from known storage ring parameters, was 160 ps full width at half maximum (FWHM).

The InP detector was positioned in the collimated 0.5 x 1-mm beam by a remotely controlled x-y translator. The output of the detector was connected to a nearby sampling oscilloscope head, which had a risetime <25 ps. A bias voltage of 400 mV was used throughout.

A number of devices were examined in the pulsed x-ray beam. While some of the highest output units produced signals (~ 8 mV) that could be examined directly with the sampling oscilloscope, accurate pulse-width measurements required the use of a digital signal averager fed by the sampling oscilloscope. Figure II-6 shows the response of one of the fastest x-ray detectors tested, together with its response to an 850-nm AlGaAs diode laser



0.85 μm
LASER DIODE
SOURCE



X-RAY
SOURCE
($\sim 6\text{-}10\text{ keV}$)

Fig. II-6. Photoresponse of a $48 \times 48\text{-}\mu\text{m}$ InP photoconductive detector to an AlGaAs laser pulse with a FWHM $< 100\text{ ps}$ (top) and an x-ray pulse with a FWHM $= 160\text{ ps}$ (bottom). A bias of 400 mV was used.

source which produced pulses having a FWHM ≤ 100 ps (see Ref. 13). The long tail evident in the response to the diode source is almost completely absent in the x-ray response. Thus, devices which are slow as optical detectors can be fast x-ray detectors. Since the absorption length is about $0.6 \mu\text{m}$ at the diode laser wavelength and $10 \mu\text{m}$ in the x-ray region, the performance at 850 nm may be influenced by surface conditions. In recent experiments it has, in fact, been found that for some devices the long tail observed in the response to the diode laser is influenced by surface treatment.

The fastest devices examined showed a FWHM of 260 ps, substantially longer than the calculated source pulse width of 160 ps. Since the measured pulses show some tailing, the measured risetime provides a better means of characterizing the device response. Using the measured value of the 10- to 90-percent risetime (145 ps), the risetime of the source (115 ps), and the expression $\tau_{\text{meas}}^2 = \tau_{\text{source}}^2 + \tau_{\text{device}}^2$, we obtain a device risetime τ_{device} of ≈ 88 ps. Faster x-ray detectors have been reported¹⁶⁻¹⁸; for example, x-ray vacuum photodiodes have shown risetimes < 50 ps (see Ref. 16) and x-ray streak cameras have shown 15-ps resolution.¹⁷ However, the InP devices are the fastest all-solid-state x-ray detectors reported to date. They are simple, compact devices which could be integrated into array structures.

T.F. Deutsch	F.J. Leonberger
A.G. Foyt	D. Mills†

†School of Applied and Engineering Physics and Cornell High Energy Synchrotron Source, Cornell University, Ithaca, New York 14853.

REFERENCES

1. D.K. Killinger and N. Menyuk, IEEE J. Quantum Electron. QE-17, 1917 (1981).
2. N. Menyuk and D.K. Killinger, Opt. Lett. 6, 301 (1981).
3. N. Menyuk, D.K. Killinger, and W.E. DeFeo, Appl. Opt. 21, 2275 (1982).
4. B. Marthinsson, J. Johansson, and S.T. Eng, Opt. Quantum Electron. 12, 327 (1980).
5. R.J. Hill, S.F. Clifford, and R.S. Lawrence, J. Opt. Soc. Am. 70, 1192 (1980).
6. N. Menyuk, D.K. Killinger, and C.R. Menyuk, Appl. Opt. (to be published).
7. D.J. Ehrlich, R.M. Osgood, Jr., and T.F. Deutsch, IEEE J. Quantum Electron. QE-16, 1233 (1980).
8. R.M. Osgood, Jr. and D.J. Ehrlich, Opt. Lett. (to be published).
9. J.P. Marton and J.R. Lemon, Phys. Rev. B 4, 271 (1971).
10. S.R.J. Brueck and D.J. Ehrlich, Phys. Rev. Lett. 48, 1678 (1982).
11. D.C. Emmony, R.P. Howson, and L.J. Willis, Appl. Phys. Lett. 23, 598 (1973).
12. P.A. Temple and M.J. Soileau, IEEE J. Quantum Electron. QE-17, 2067 (1981).
13. A.G. Foyt, F.J. Leonberger, and R.C. Williamson, Appl. Phys. Lett. 40, 447 (1982), and references therein.
14. B.O. Seraphim and H.E. Bennett, in Semiconductors and Semimetals, edited by R.K. Willardson and A.C. Beer (Academic, New York, 1967), Vol. 3, pp. 529-530.
15. W.J. Veigle, Atomic Data Tables 5, 51 (1973).

16. R.H. Day, P. Lee, E.B. Soloman, and D.J. Nagel, Los Alamos Scientific Laboratory Report LA-7941-MS (February 1981).
17. D.T. Attwood, R.L. Kaufman, G.L. Stradling, K.L. Medeck, R.A. Lerche, L.W. Coleman, E.L. Pierce, S.W. Thomas, D.E. Campbell, J. Noonan, G.R. Tripp, R.J. Schnetz, and G.E. Phillips, XIV International Congress on High Speed Photography and Photonics, Moscow, USSR, October 1980; and Lawrence Livermore Laboratory Report UCRL-85043 (October 15, 1980).
18. P.B. Lyons, in Low Energy X-Ray Diagnostics, edited by D.T. Attwood and B.L. Henke, AIP Proceeding No. 75 (American Institute of Physics, New York, 1981), p. 59.

III. MATERIALS RESEARCH

A. LOW-DISLOCATION-DENSITY GaAs EPILAYERS GROWN ON Ge-COATED Si SUBSTRATES BY MEANS OF LATERAL EPITAXIAL OVERGROWTH

We recently reported^{1,2} the growth of single-crystal GaAs layers by chemical vapor deposition (CVD) on Ge-coated Si<100> substrates. The dislocation density in these layers is more than 10^7 cm^{-2} . The dislocations originate from the underlying Ge coatings, which contain more than 10^9 cm^{-2} dislocations due to the large lattice mismatch (~ 4 percent) between Ge and Si. The high dislocation density in the GaAs layers leads to a significant reduction in the conversion efficiency of shallow-homojunction solar cells fabricated in these layers.²

In this report, we describe the utilization of lateral epitaxial overgrowth to obtain GaAs layers with greatly reduced dislocation densities on GaAs/Ge/Si substrates. This overgrowth technique was developed for CVD growth on reusable substrates by the CLEFT (cleavage of lateral epitaxial films for transfer) process.³ The principle of the technique is illustrated by Fig. III-1, which is a schematic cross-sectional diagram of a sample at an intermediate stage of overgrowth. An initial GaAs layer is grown by conventional CVD on a Ge-coated Si wafer. This layer is masked with a film of SiO_2 , narrow stripe openings are etched in the SiO_2 film, and GaAs is then grown under conditions such that nucleation takes place only on the regions of the first layer exposed by the openings. The epitaxial GaAs deposits formed seed lateral growth over the SiO_2 . If this growth is allowed to proceed for a sufficient time, the growth fronts from adjacent openings merge to form a continuous GaAs layer with the same orientation as the Si substrate.

The GaAs layers obtained by the overgrowth technique have dislocation densities of less than 10^4 cm^{-2} , and their electrical properties are comparable to those of conventional GaAs epilayers. Shallow-homojunction solar cells fabricated in such overgrown layers should have efficiencies

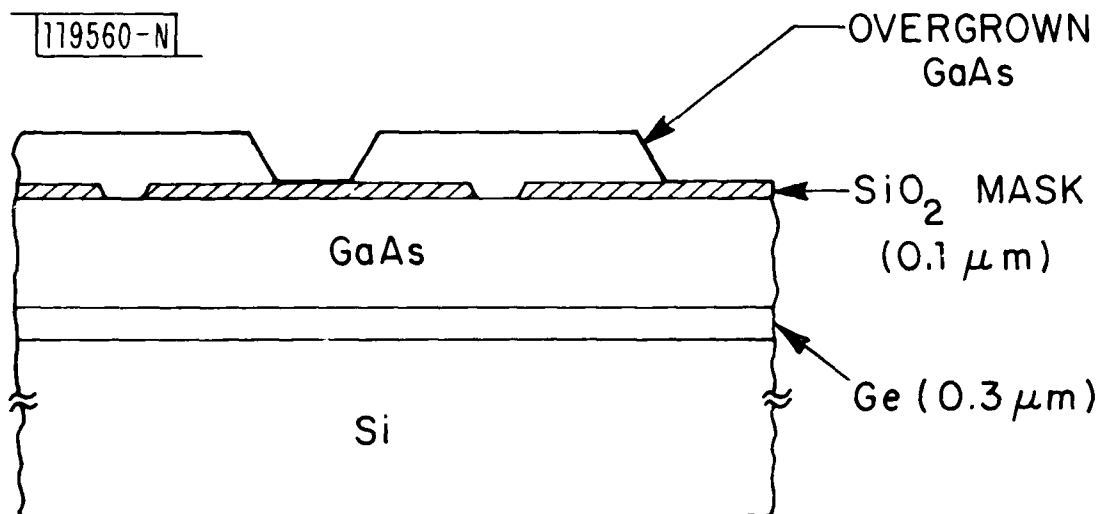


Fig. III-1. Schematic diagram showing lateral overgrowth of GaAs seeded within stripe openings in a SiO₂ mask on a GaAs/Ge/Si substrate.

approaching those of cells in conventional layers. In addition, the formation of high-quality GaAs layers on Si substrates is an important step in the development of monolithic GaAs/Si integrated circuits.

Preparation of the GaAs/Ge/Si heterostructures used as substrates has been described previously.¹ Briefly, epitaxial Ge films 0.2 to 0.3 μm thick are deposited by electron-beam evaporation on Si wafers, oriented 2° off (001) toward (110), and mirror-smooth GaAs epilayers 2 to 4 μm thick are grown on the Ge films in an AsCl₃-GaAs-H₂ system. To prepare a GaAs/Ge/Si substrate for overgrowth, a growth mask is formed by coating the GaAs layer with a CVD SiO₂ film about 0.1 μm thick and defining stripe openings in the film by conventional photolithographic techniques.

In experiments on the CLEFT process, which employs (110) GaAs substrates, it was found that lateral growth of GaAs is strongly affected by the direction of the openings in the growth mask with respect to the crystal lattice of the substrate.⁴ In the present investigation, this effect has

been studied for 2°-off-(001) GaAs/Ge/Si substrates by using a special mask that contains a circular array of radial parallel pairs of stripe openings indexed at 1° intervals over a full 360°. The orientation dependence is determined by carrying out CVD growth on a masked substrate until the GaAs layer is 2 to 4 μm thick, but has not yet become continuous. Figure III-2 is a photomicrograph showing the results of such an experiment. The regions where growth occurred appear as dark areas. The amount of lateral growth exhibits a strong periodic dependence on angle, with minimum growth occurring for stripe openings at angles corresponding to $\langle 110 \rangle$ and $\langle 100 \rangle$ directions in the plane of the substrate. The optimum angle for growth of GaAs layers is 25° counterclockwise from the $\langle 110 \rangle$ direction. At this angle the lateral growth fronts are straight and smooth, and the ratio of lateral-to-vertical growth rates is typically 5 to 6, although ratios as high as 10 have been observed.

In order to prepare continuous GaAs layers by lateral growth, we have used SiO_2 masks with parallel stripe openings etched in the optimum direction over the whole substrate surface. Continuous layers 3 to 5 μm thick with smooth surface morphology have been obtained for stripe openings that are 3 to 5 μm wide and spaced 30 to 50 μm apart. These layers were doped with S by adding H_2S to the gas stream in the CVD system; the GaAs layers grown directly on the Ge/Si substrates were not intentionally doped. Both types of layers have n-type conductivity.

The crystal quality of the overgrown GaAs layers has been studied by transmission electron microscopy (TEM) in both the cross-sectional and planar modes. Figure III-3 is a cross-sectional micrograph showing a typical laterally overgrown region in which there are no dislocations in the overgrown GaAs layer, although the layer grown directly on the Ge/Si substrate contains a high density of dislocations threading from the Ge film. In fact, the only dislocations that we have observed in the overgrown layers are a small number that originate within the stripe openings but quickly bend over and do not propagate. As in the CLEFT films,⁴ no dislocations are formed on the lines of intersection where the lateral growth fronts from adjacent openings merge. The number of dislocations observed by

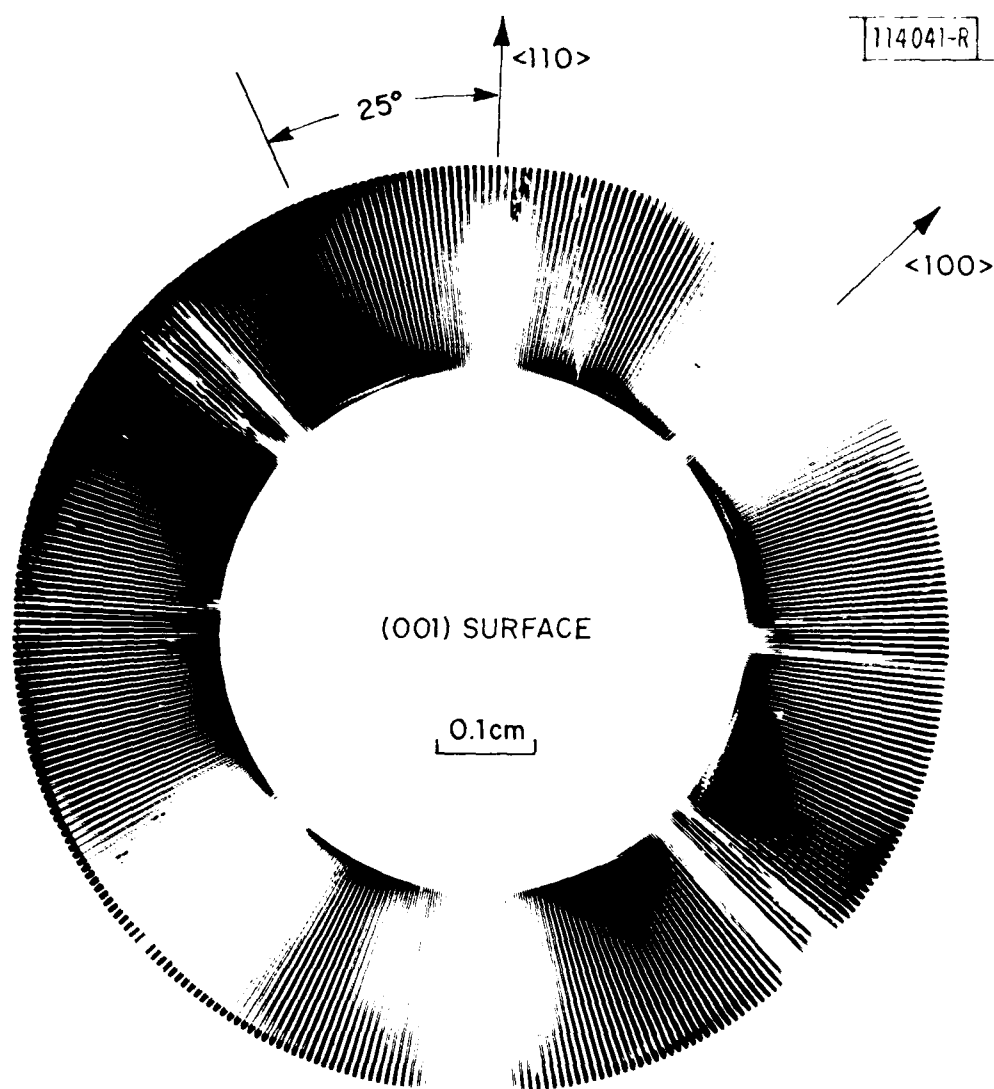


Fig. III-2. Photomicrograph showing growth of GaAs over a SiO_2 test mask on a GaAs/Ge/Si substrate.

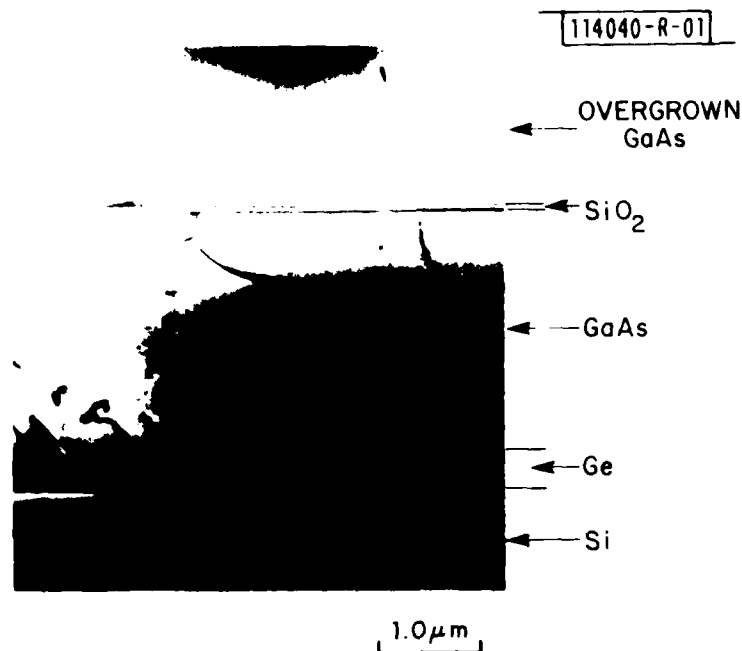
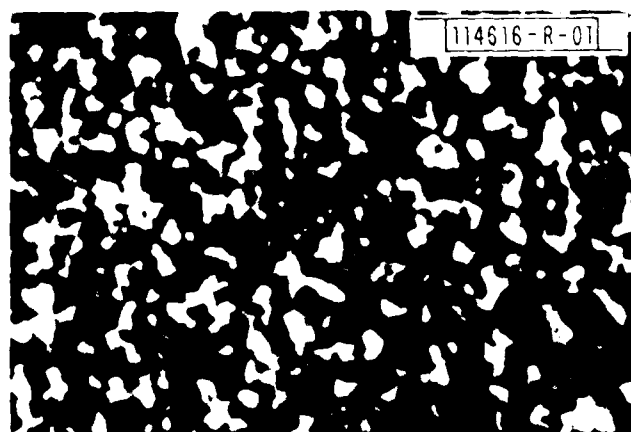


Fig. III-3. Cross-sectional TEM micrograph of one section of a sample prepared by lateral overgrowth of GaAs on a GaAs/Ge/Si substrate.

TEM in the overgrown GaAs layers is too small to permit an accurate evaluation of the dislocation density, but we estimate an upper limit of 10^4 cm^{-2} .

The crystal quality of the overgrown GaAs layers has been confirmed by scanning cathodoluminescence microscopy (SCM), an imaging technique that shows the spatial variation in the intensity of cathodoluminescence excited by the electron beam of a scanning electron microscope. Figures III-4(a) and (b), respectively, are typical SCM micrographs of a GaAs layer grown directly on a Ge/Si sample and of an overgrown GaAs layer. The dark features in Fig. III-4(a) are due to dislocations, which cause nonradiative recombination of the electron-hole pairs generated by the electron beam. The density of these features approximates the dislocation density found by TEM measurements.



(a)



(b)

20 μm

Fig. III-4. Scanning cathodoluminescence micrographs of (a) a GaAs layer grown directly on a Ge/Si substrate, and (b) a laterally overgrown GaAs layer on a GaAs/Ge/Si substrate.

The parallel light and dark bands in Fig. III-4(b) are due to a periodic variation in the carrier concentration of the overgrown layer, which is revealed because the cathodoluminescence intensity of n-type GaAs increases with increasing carrier concentration. This periodic variation occurs because the concentration of S incorporated in the layer differs for the lateral fronts growing from the opposite sides of each stripe opening, as a result of the difference in crystallographic orientation between these fronts. (A similar variation has been observed for CLEFT films.⁴) No variations in intensity due to dislocations are observed within the bright bands, indicating that the dislocation density in the overgrown layer does not exceed 10^4 cm^{-2} .

The average carrier concentration in the overgrown layers at room temperature is $\sim 8 \times 10^{16} \text{ cm}^{-3}$, as determined by Hall coefficient measurements. The electron mobility in these layers is $\sim 4500 \text{ cm}^2/\text{V-s}$, compared with $5400 \text{ cm}^2/\text{V-s}$ for similarly doped layers grown by conventional CVD on single-crystal GaAs substrates. This initial result indicates that the electrical properties of the overgrown layers will be satisfactory for many device applications.

B-Y. Tsaur	J.P. Salerno
R.W. McClelland	B.A. Vojak
J.C.C. Fan	C.O. Bozler
R.P. Gale	

B. EFFECTS OF IONIZING RADIATION ON n-CHANNEL MOSFETs FABRICATED IN ZONE-MELTING-RECRYSTALLIZED Si FILMS ON SiO_2 -COATED SUBSTRATES

Silicon-on-insulator (SOI) MOS devices have several advantages over their bulk Si counterparts as components for radiation-hardened circuits: reduced transient photocurrent, elimination of latch-up, increased speed and packing density. Consequently, Si-on-sapphire (SOS) devices are utilized extensively in such circuits. However, SOS n-channel MOSFETs also have an important disadvantage, since ionizing radiation produces a significant back-channel leakage current.

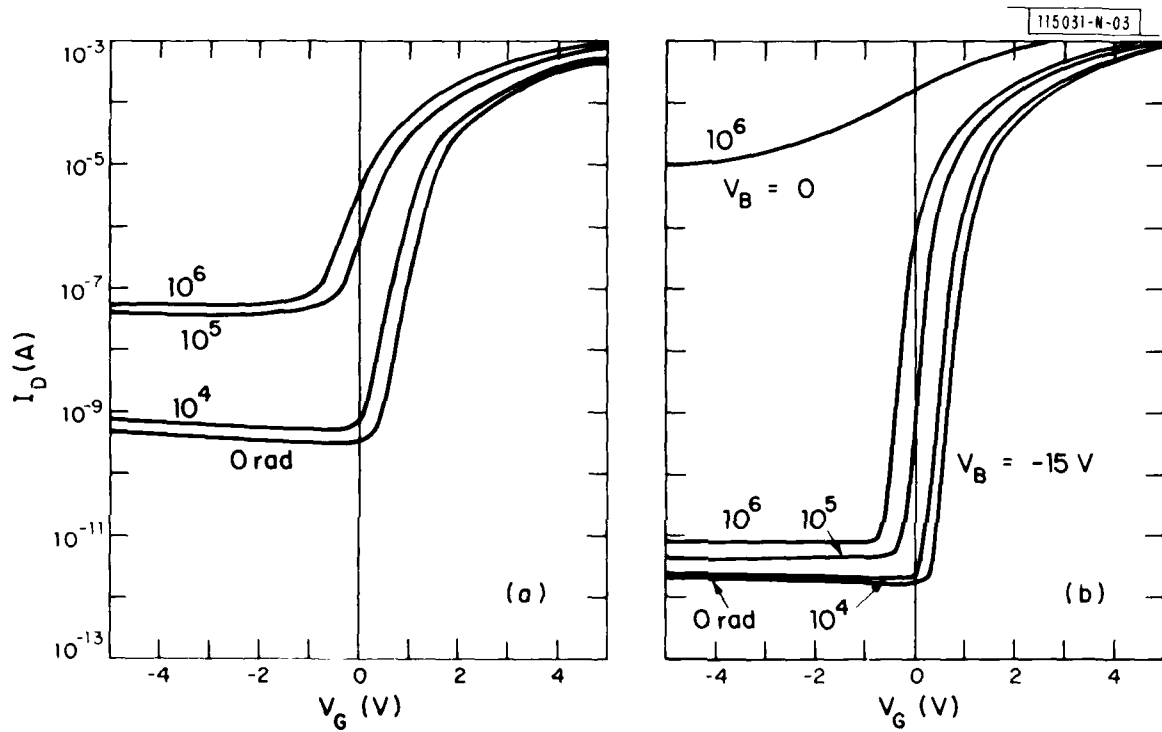


Fig. III-5. Subthreshold source-drain current I_D vs gate voltage V_G before and after irradiation of (a) SOS and (b) recrystallized-Si MOSFETs.

We recently reported⁵ the fabrication of n-channel MOSFETs in thin Si films prepared by zone-melting recrystallization of poly-Si deposited on SiO₂-coated Si substrates. These SOI devices exhibit surface electron mobilities close to those of single-crystal Si devices, and they have subthreshold leakage currents of less than 1 pA/ μ m (channel width). To evaluate the new devices as possible alternatives to SOS MOSFETs for radiation-hardened circuits, we have investigated the effects of irradiation with 1.5-MeV electrons on their leakage current and threshold voltage. We have found that the adverse consequences of ionizing radiation can be largely suppressed by applying a moderate negative bias to the Si substrate during irradiation and device operation in order to reduce the effect of charge trapping in the SiO₂ coating. We therefore believe that SOI MOSFETs fabricated in the recrystallized films show great promise as components for radiation-hardened circuits.

N-channel MOSFETs were fabricated in recrystallized Si films on SiO₂-coated Si substrates and also in the Si films (0.5 μ m thick) of commercial SOS wafers, by a standard self-aligned poly-Si gate technique. The device channel was doped by implantation with 60-keV B ions. Half the devices also received a deep channel implant of 200-keV B ions. The drain, gate, and substrate biases with respect to ground are represented by V_D , V_G , and V_B , respectively.

The MOSFETs were irradiated with doses of 1.5-MeV electrons ranging from 3×10^{10} to 3×10^{13} cm⁻², corresponding to ionizing doses from 10^3 to 10^6 rad(Si). The bias voltages during irradiation were $V_D = 5$ V, $V_G = 0$ V, and $V_B = 0$ or -15 V. Subthreshold leakage current and threshold voltage measurements were performed within 20 min. after exposure. For each device, the V_D and V_B values were the same during the measurements as during irradiation.

Figure III-5 shows typical subthreshold source-drain I-V characteristics for (a) SOS and (b) recrystallized-Si devices, respectively, before and after irradiation. The devices received the deep B implant. For the SOS device, a two-order-of-magnitude increase in the leakage current and a significant increase in subthreshold slope are observed after 10^6 rad(Si) irradiation.

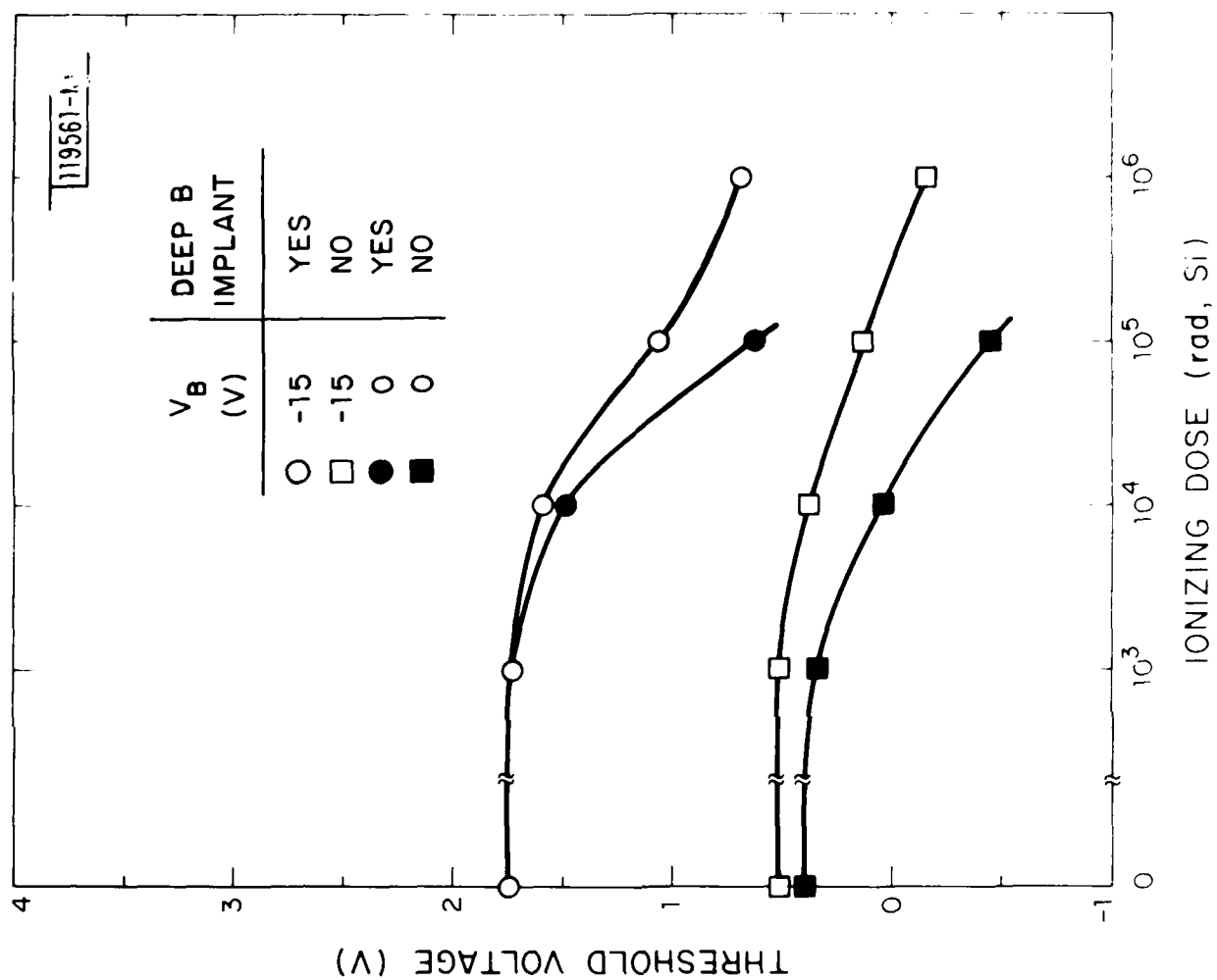


Fig. III-6. Threshold voltage of recrystallized-Si MOSFETs as a function of ionizing dose.

These results are typical of SOS devices exposed to this dose of ionizing radiation. For the recrystallized-Si devices, the characteristics depend strongly on whether or not the substrate was biased. For a dose of 10^6 rad(Si), the devices with $V_B = 0$ become extremely leaky and cannot be turned off even with a large negative gate bias. For the same dose, the subthreshold slope of the devices with $V_B = -15$ V remains sharp and the leakage current is less than 0.2 pA/ μ m (channel width), which is far lower than the current after irradiation for the best SOS devices reported.⁶

Ionizing radiation causes a reduction in threshold voltage V_T , as indicated by the gradual shift of subthreshold curves shown in Fig. III-5. In Fig. III-6, V_T deduced from linear source-drain I-V characteristics is plotted as a function of ionizing dose for recrystallized-Si devices that differ in channel doping and substrate bias. Compared with the devices without substrate bias, the devices with $V_B = -15$ V have nearly the same value of V_T before irradiation but display a smaller shift of V_T due to irradiation. The shift should be further decreased by using thinner gate oxide and employing gate oxidation procedures optimized for radiation hardening.⁷

For the recrystallized-Si MOSFETs, as well as for the SOS devices, exposure to ionizing radiation produces an increase in leakage current (Fig. III-5) because the insulator below the Si film becomes positively charged, inducing a conducting inversion channel in the Si near the Si-insulator interface. Positive charging occurs because holes generated by the radiation are more readily trapped than the more mobile electrons, which are largely swept out of the insulator by the electric field between the source and drain. For recrystallized-Si devices irradiated without substrate biasing, the leakage current is much higher than for SOS devices exposed to the same dose, because the density of trapped positive charge is greater for SiO_2 than for Al_2O_3 and also because the electron mobilities close to the Si-insulator interface are much higher in the recrystallized-Si films than in Si films on sapphire. These mobilities are typically about $650 \text{ cm}^2/\text{V-s}$ (Ref. 5) and 50 to $100 \text{ cm}^2/\text{V-s}$ (Ref. 8), respectively.

For the recrystallized-Si MOSFETs, applying a moderate negative bias to the Si substrate has two effects that, together, greatly reduce the increase in leakage current produced by ionizing radiation. First, because of the electric field due to the bias, more of the holes generated by the radiation are removed from the SiO_2 layer before they can be trapped, so that the density of positive charge in the layer is reduced. Second, during device operation the electric field counteracts the tendency of the positive charge to induce an inversion channel in the Si film. This effect is equivalent to a reduction in the trapped charge density of $\Delta N_T = C_i V_B / q = \epsilon_i V_B / dq$, where C_i is the capacitance per unit area of the SiO_2 layer, d is the thickness of this layer, and ϵ_i is the dielectric constant of SiO_2 . In the present experiments, $\Delta N_T = 3.3 \times 10^{11} \text{ cm}^{-2}$. It should be possible to obtain still higher values of ΔN_T in the recrystallized-Si devices by increasing V_B or decreasing d to increase the applied electric field. In these initial experiments, no attempt was made to investigate the effect of varying these parameters. The reduction in V_T produced by exposure of the recrystallized-Si devices to ionizing radiation (Fig. III-6) is due to the trapping of positive charge in the gate oxide as well as in the SiO_2 layer below the Si film.^{9,10} Applying a negative bias to the Si substrate decreases the shift in V_T because it reduces the effect of charge trapping in the lower SiO_2 layer. In recrystallized-Si MOSFETs with substrate bias, we expect the shift in V_T to be essentially the same as in bulk Si devices.

B-Y. Tsaur	G.W. Turner
J.C.C. Fan	D.J. Silversmith

C. ZONE-MELTING RECRYSTALLIZATION OF Si FILMS ON SiO_2 -COATED Si SUBSTRATES

We previously reported¹¹⁻¹⁵ the preparation of high-quality Si films on SiO_2 -coated Si substrates by zone-melting recrystallization using two graphite strip heaters, a lower fixed heater and an upper movable one. Recrystallization was carried out either with seeding (the LESS technique of lateral epitaxy by seeded solidification)¹¹⁻¹³ or without seeding.^{14,15}

Films recrystallized with and without seeding are similar in crystal quality, except that the LESS films do not contain large-angle grain boundaries. All but the initial LESS films contain sub-boundaries. Such sub-boundaries have little effect on the device characteristics of n-channel MOSFETs,¹⁶ while the effects of grain boundaries are more detrimental.

Because of the limited dimensions of the initial strip-heater apparatus, films previously recrystallized were only about 2.5 cm on a side. We have now constructed a larger system with sufficient temperature uniformity for the recrystallization of significantly larger Si films. The new system employs a standard stainless-steel vacuum chamber with eight ports that allow easy access. The top of the chamber has an optical quartz window for visually monitoring the recrystallization process. The top, bottom, and side wall of the chamber are water cooled. As shown schematically in Fig. III-7, a sample wafer is placed in a circular depression at the center of the lower heater. Both heaters are resistively heated by alternating currents up to a few hundred amperes that are monitored and controlled by a microprocessor. Temperatures at the center and edges of the wafer are monitored by three Pt/Pt-13% Rh thermocouples imbedded in the lower heater. These temperatures are found to be uniform to about 50°C.

The substrates are single-crystal <100>Si wafers that have been overcoated with thermal SiO₂, CVD Si, and a Si₃N₄/SiO₂ encapsulant. The recrystallization procedure is carried out in flowing Ar at atmospheric pressure. After the bottom heater reaches its operating temperature, the upper heater is heated until the surface of the Si film begins to melt, forming a narrow molten zone. The upper heater is then scanned across the sample by means of a computer-controlled motor.

The initial experiments with the new system were performed without intentional seeding. In these experiments, the recrystallization procedure was developed to the point where Si films could be routinely recrystallized over at least 80 percent of their area. The recrystallized films consisted of elongated grains running generally parallel to the direction of molten-zone motion. However, in several cases we observed that some regions

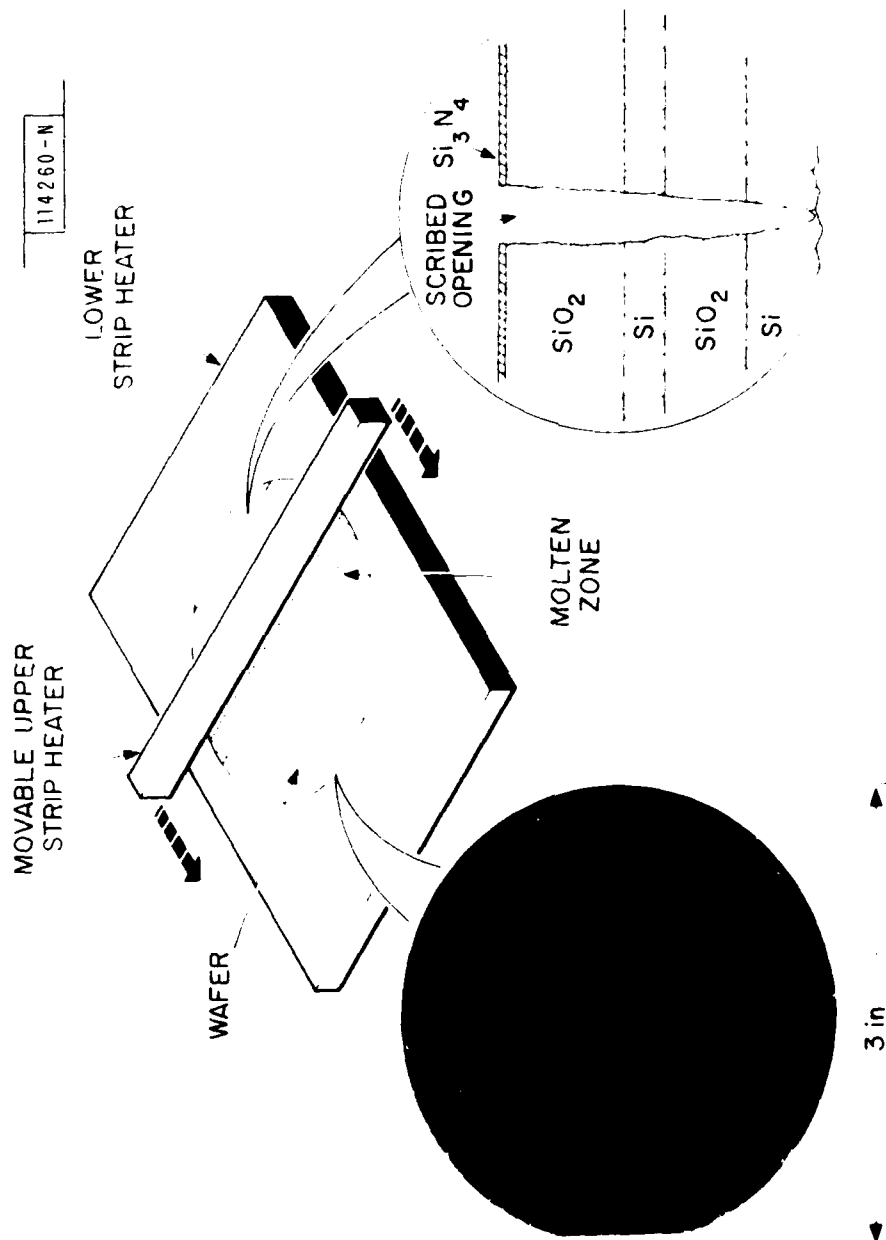


Fig. III-7. Top: schematic diagram of sample and heater configuration used for zone-melting recrystallization. Lower right: schematic cross-sectional diagram of scribed seed opening. Lower left: optical micrograph of recrystallized Si film.

adjacent to the wafer edges did not contain large-angle grain boundaries, apparently because the initial melting process had resulted in contact between the molten zone and the edge of the Si wafer. This observation suggested the possibility of accomplishing controlled seeding for the LESS technique by scribing a narrow opening, near one end of the sample, that extended through the $\text{Si}_3\text{N}_4/\text{SiO}_2$ encapsulant, the Si film, and the SiO_2 film to the Si wafer. This seeding procedure has proved to be very successful.

A schematic cross-sectional diagram of a seed opening is shown at the lower right side of Fig. III-7, and a photograph of a sample that was recrystallized using the seeding procedure is shown at the lower left side. (The opening is seen as a bright line near the right side of the photograph.) The sample is placed on the lower graphite heater with the opening parallel to the upper heater, as shown in the upper diagram of Fig. III-7. The upper heater is positioned so that the molten zone in the Si film is initially formed between the opening and the nearer edge of the sample. When the heater is scanned across the opening, contact is established between the molten film formed just beyond the opening and the exposed surface of the Si wafer, which seeds the solidification of the melt as the heater moves away.

After recrystallization, the sample wafers are unwarped. Whether seeded or unseeded, the recrystallized films remain visually mirror smooth, but they differ in reflectivity from the as-deposited films. This difference is apparent in the photograph of Fig. III-7, where it can be seen that almost all the film was recrystallized, with only regions at the beginning of the heater scan and around the edge of the sample remaining unmelted.

Figures III-8(a) and (b) are photomicrographs illustrating the effectiveness of the new seeding procedure. A small portion of one recrystallized film in the vicinity of the seed opening is shown in Fig. III-8(a). The direction of molten-zone motion was from top to bottom in the photomicrograph, so that recrystallization was unseeded in the region shown above the opening and seeded in the region below it. After recrystallization, the film was etched by a technique described elsewhere¹⁵ to produce a grid of etch pits that indicate the local crystallographic orientation.

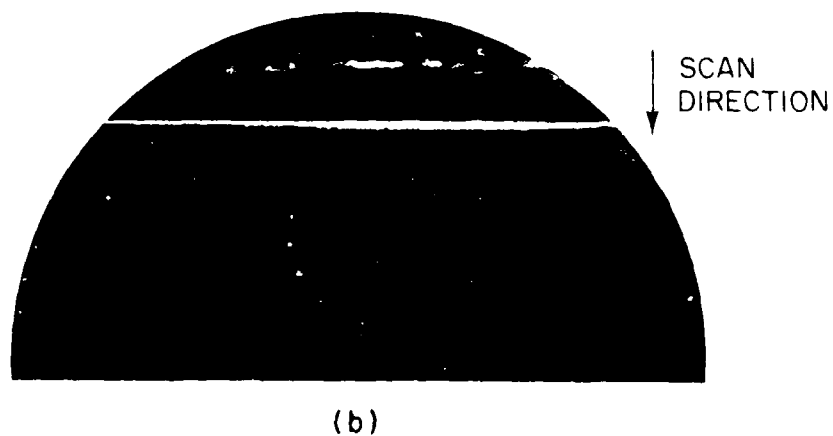
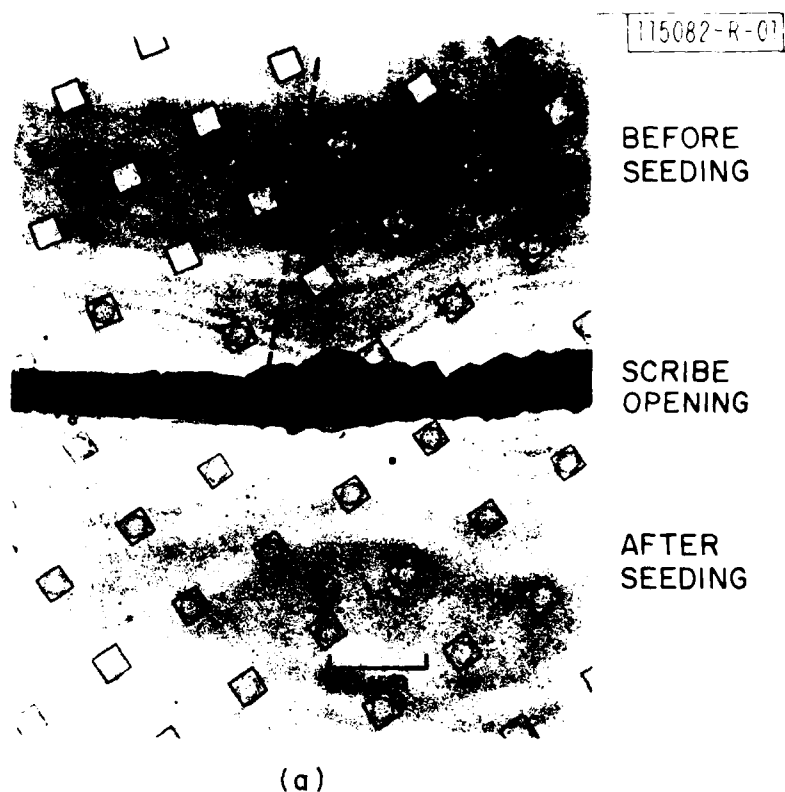


Fig. III-8. (a) Optical micrograph of unseeded and seeded regions adjacent to scribed seed opening in recrystallized Si film that has been etched to show local crystallographic orientation. (b) Optical micrograph of much larger area of similarly recrystallized and etched film.

All the pits are square, showing that both unseeded and seeded regions have (100) texture. The diagonals of the pits lie in $\langle 100 \rangle$ directions. The alignment of the pits shows that a large-angle grain boundary is present in the unseeded region, but is no longer present after seeding.

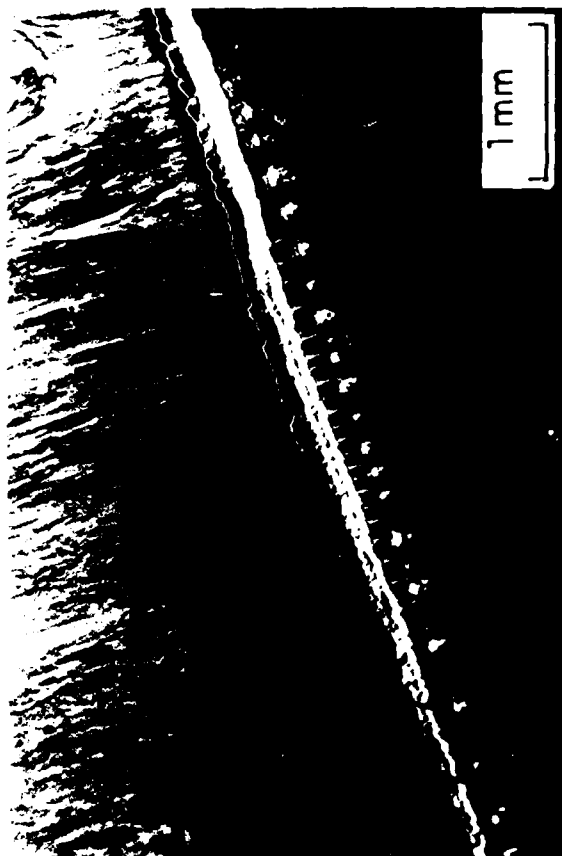
Figure III-8(b) shows a larger area of a film that was etched after recrystallization. The seed opening in this film was scribed in a $\langle 100 \rangle$ direction, so that molten-zone motion took place along a $\langle 100 \rangle$ direction, which is the preferred growth direction for spontaneously nucleated grains in films recrystallized by the strip-heater method.^{14,15} A large number of grains are present in the unseeded region, but after seeding there are only a few grains, almost all of which originate from the periphery of the sample, where the film remained unmelted. Furthermore, since these grains propagate roughly parallel to the direction of molten-zone motion, an area of the film approximately as wide as the seed opening remains free of grain boundaries.

Although the new seeding procedure eliminates almost all large-angle grain boundaries, the films obtained by this procedure still contain large numbers of low-angle subgrain boundaries, at about the same density as in films recrystallized in the smaller strip-heater system. The sub-boundaries, which run roughly parallel to the direction of molten-zone motion, are easily delineated by etching.^{15,16} They can be detected nondestructively by examining the films with a scanning electron microscope operating in the backscattering mode. Three micrographs obtained in this manner for one recrystallized film are shown in Fig. III-9. The upper micrograph shows unseeded and seeded regions adjacent to the seed opening. There is a high density of sub-boundaries in both regions, except for a band about 20 to 50 μm wide at the beginning of the seeded region. The micrographs at the lower left and lower right, which are higher magnification images of the unseeded and seeded regions, respectively, show the individual subgrains. We estimate that the differences in intensity between the subgrains correspond to variations in tilt of less than 1° .

The recrystallized films also contain defects of another type - protrusions several micrometers across and less than 0.5 μm high that are located along the sub-boundaries. A number of these protrusions are visible

114613-R

BEFORE SEEDING



AFTER SEEDING

PROTRUSIONS

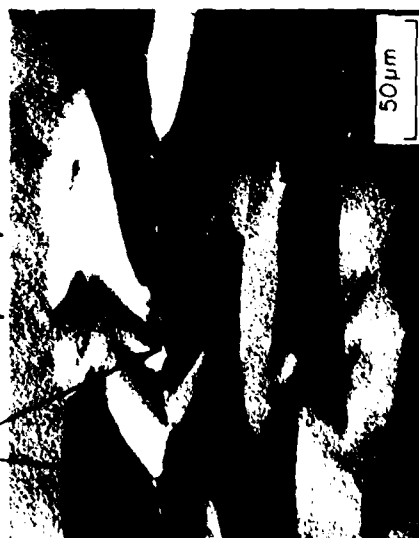


Fig. III-9. Micrographs of recrystallized Si film taken with a scanning electron microscope operated in backscattering mode. Top: unseeded and seeded regions adjacent to scribed seed opening. Lower left and lower right: magnified views taken in unseeded and seeded regions, respectively.

as bright spots in the lower left micrograph of Fig. III-9 showing the unseeded region. No protrusions are present within the portion of the seeded region shown in the lower right micrograph, but their density in the rest of the film is about the same as in the unseeded region. Protrusions are also present, though much less frequently, in films recrystallized in the smaller system. The origin of the protrusions is not well understood, and their effects on MOSFET characteristics are being investigated.

J.C.C. Fan R.L. Chapman
B-Y. Tsaur M.W. Geis

REFERENCES

1. B-Y. Tsaur, M.W. Geis, J.C.C. Fan, and R.P. Gale, Appl. Phys. Lett. 38, 779 (1981), DTIC AD-A103403/2.
2. R.P. Gale, J.C.C. Fan, B-Y. Tsaur, G.W. Turner, and F.M. Davis, IEEE Electron Device Lett. EDL-2, 169 (1981), DTIC AD-A107056/4.
3. R.W. McClelland, C.O. Bozler, and J.C.C. Fan, Appl. Phys. Lett. 37, 560 (1980), DTIC AD-A101024/8.
4. C.O. Bozler, R.W. McClelland, J.P. Salerno, and J.C.C. Fan, J. Vac. Sci. Technol. 20, 720 (1982).
5. B-Y. Tsaur, M.W. Geis, J.C.C. Fan, D.J. Silversmith, and R.W. Mountain, Appl. Phys. Lett. 39, 909 (1981), DTIC AD-A113234.
6. J.H. Yuan and E. Harari, IEEE Trans. Nucl. Sci. NS-24, 2199 (1977).
7. K.G. Aubuchon, IEEE Trans. Nucl. Sci. NS-18, 117 (1973).
8. S.T. Hsu, IEEE Trans. Electron Devices ED-25, 913 (1978).
9. E. Sano, R. Kasai, K. Ohwada, and H. Ariyoshi, IEEE Trans. Electron Devices ED-27, 2043 (1980).
10. E.R. Worley, IEEE Electron Device Lett. EDL-2, 139 (1981).

11. J.C.C. Fan, M.W. Geis, and B-Y. Tsaur, IEDM Technical Digest Washington, DC, 8-10 December 1980, p. 845.
12. J.C.C. Fan, M.W. Geis, and B-Y. Tsaur, Appl. Phys. Lett. 38, 365 (1981), DTIC AD-A103036/0.
13. B-Y. Tsaur, J.C.C. Fan, M.W. Geis, D.J. Silversmith, and R.W. Mountain, Appl. Phys. Lett. 39, 561 (1981), DTIC AD-A110725.
14. E.W. Maby, M.W. Geis, Y.L. LeCoz, D.J. Silversmith, R.W. Mountain, and D.A. Antoniadis, IEEE Electron Device Lett. EDL-2, 241 (1981).
15. M.W. Geis, H.I. Smith, B-Y. Tsaur, J.C.C. Fan, E.W. Maby, and D.A. Antoniadis, Appl. Phys. Lett. 40, 158 (1982).
16. B-Y. Tsaur, J.C.C. Fan, M.W. Geis, D.J. Silversmith, and R.W. Mountain, IEEE Electron Device Lett. EDL-3, 79 (1982).

IV. MICROELECTRONICS

A. CHARGE-COUPLED DEVICES: TIME-INTEGRATING CORRELATOR

A CCD implementation of a time-integrating correlator (TIC) capable of high-speed operation was described in a previous report.¹ This device can correlate an analog signal with a continuously varying binary reference, and should find application in spread-spectrum systems such as the Navstar Global Positioning System (GPS) Precision P-code. The CCD TIC integrates the product of the delayed signal, $x(t - T_i)$, and a time-varying reference waveform, $y(t)$, at the i^{th} tap for an arbitrary time period for values of i from 1 to 32. The output waveform is then a segment of the crosscorrelation of $x(t)$ and $y(t)$ whose length depends on the length of the delay line used to generate $x(t - T_i)$.

We have just completed fabrication of a device for use at a code clock rate of 10 Mbps. The correlator will be clocked at 20 MHz and will provide 16 early and 16 late correlations spaced one-half code bit apart. In order to produce a device with the highest possible bandwidth, we have adopted the pipe-organ structure used in the fastest CCD transversal filters reported to date.^{1,2} The device has been designed to have sufficient dynamic range for operation with jamming/signal ratios of up to 60 dB when used as a baseband correlator.

Two major design issues for this device were the input structure and the charge integrator. The input structure to each CCD must generate complementary charge packets for + and - representations of the analog signal. An analysis of input structures has led us to choose a method described by Sequin *et al.*³ which can be operated with differential or single-ended inputs. This structure has superior speed and balance compared with complementary fill-and-spill inputs, and superior linearity and reduced pattern noise compared with the diode-cutoff input. More importantly, it does not suffer from a susceptibility to a CW jammer at the carrier frequency, which the other inputs do. This input structure is shown in Fig. IV-1, which also shows the other essential elements of the correlator.

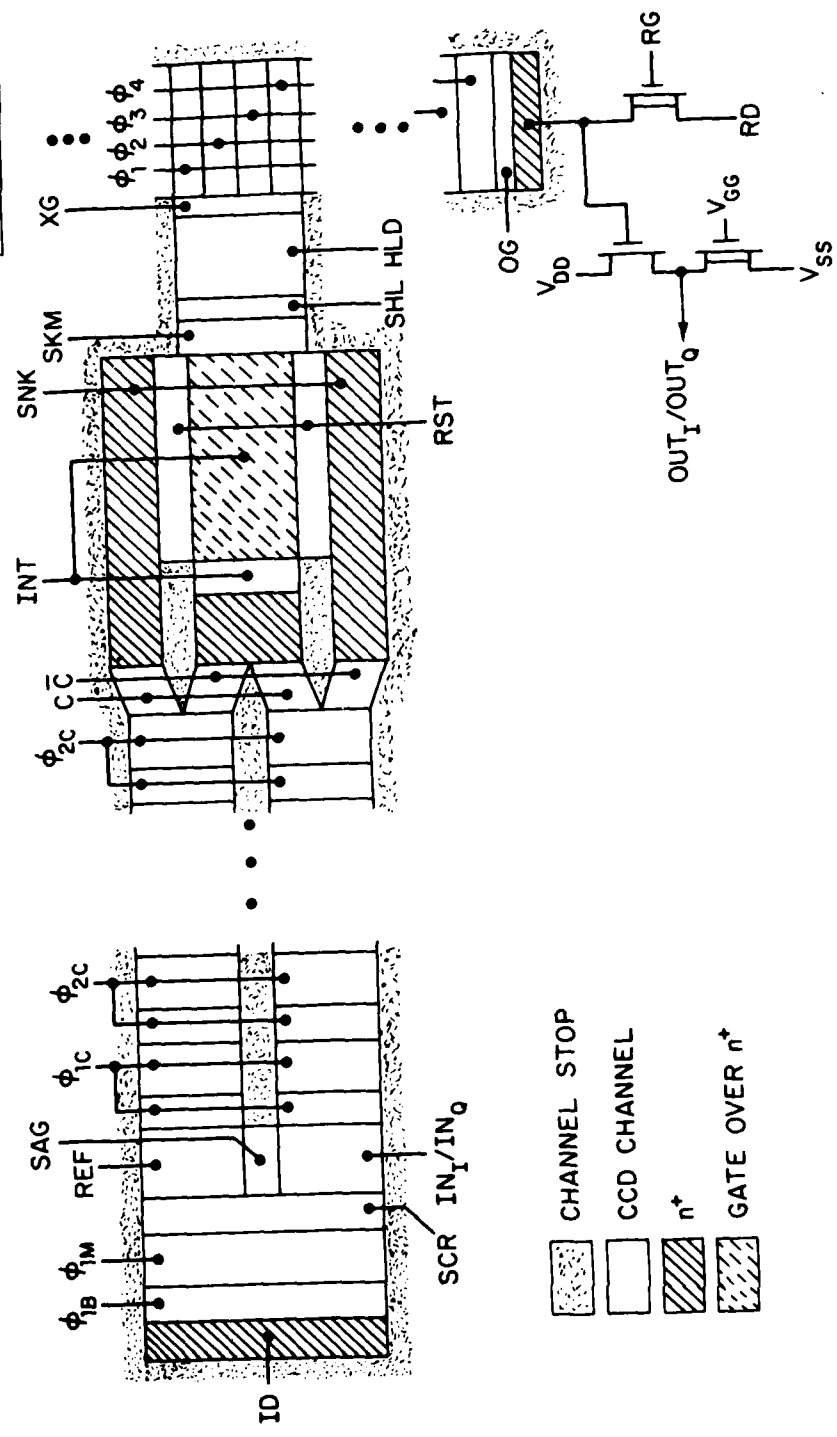


Fig. IV-1. Functional schematic diagram of detailed structure of each "pipe" of pipe-organ CCD TIC.

The charge integrator is a capacitor which must collect and store the charge packets representing the product of the analog signal and the binary reference for a period of 25 μ s or 500 clock periods. Because the large charge buildup expected during this integration time would require excessive chip area for charge storage and transfer, we have sought methods of reducing the integrated charge without introducing excessive spatial or temporal noise onto the signal. The integrated charge contains the desired signal riding on a large fixed bias. Our analysis, following lines suggested by Van Broekhoven,⁴ indicates that the signal constitutes only 1/8 of the mean integrated charge, and that the best approach is to skim this signal off the background. This reduces the amount of charge which the output register must handle and, therefore, reduces its area. However, the skimming process can introduce a spatial or pattern noise into the device, and we have used a Monte Carlo simulation method to study this process and to predict the efficacy of different compensation schemes. This simulation showed that the pattern noise could be severe, but could be removed effectively by analog or digital compensation schemes.

An effective digital cancellation scheme would require storing the 32 samples of pattern noise to an accuracy of 12 bits and using 12-bit arithmetic to correct the correlator output, which could be quantized with 8-bit accuracy. The analog cancellation scheme, on the other hand, would require only simple digital circuitry to complement the reference code during alternate integration intervals, and some minor changes in the digital integration algorithm used for post-processing the quantized correlator output. Furthermore, the accuracy of the analog technique would be limited only by the linearities of the CCD integrator, output register, and quantizer (analog-to-digital converter).

We have used the silicon wafer processing specifications to simulate the channel potential of the various parts of the CCD correlator, and have used these results to estimate the clock levels (HI and LO) and DC levels required to operate the device. We have also devised a scheme to restore the channel potential to a more reasonable range after integration. By using

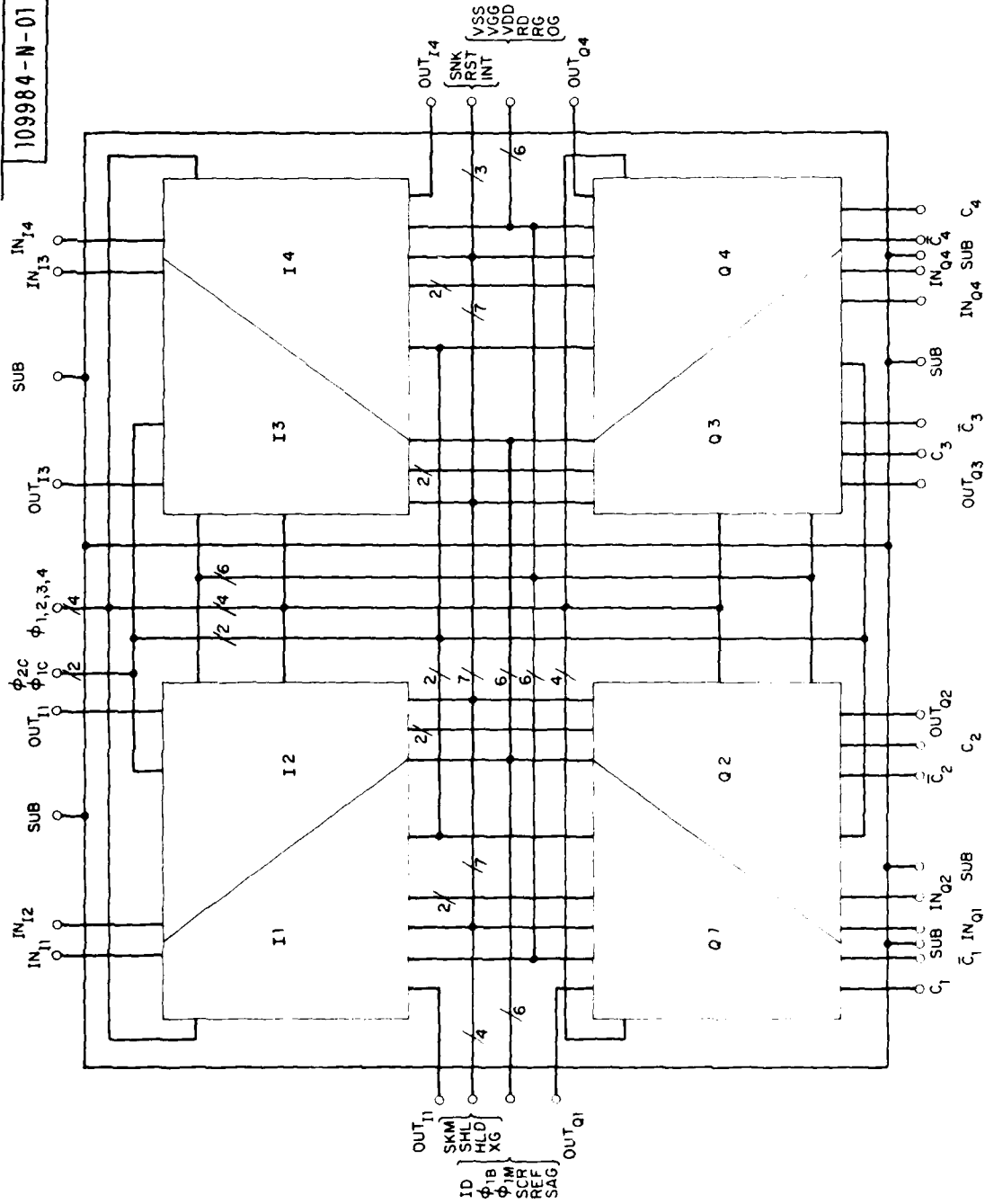


Fig. IV-2. Block diagram of correlator chip showing placement and interconnection of eight independent correlators.

this potential restoration scheme, all estimated clock levels are kept in the 0- to 12-V range.

This correlator design is so compact that it is possible to put eight of them on a single chip. The clock and DC signals are applied in common to all eight correlators, with the result that the conductors which route these signals on the chip are quite lengthy with numerous crossovers among the lines. The high clock rate of the device requires that these conductors have low resistance in order to minimize the RC time constants of the clock lines. Also, the crossovers must be on a second conductor layer. Although two layers of polysilicon are available for this purpose, the polysilicon has an unacceptably high sheet resistance. Therefore, we have elected to add a second aluminum metallization layer to the device to provide low-resistance crossovers. Figure IV-2 is a block diagram of the chip layout and shows the eight correlators with all their interconnects.

The correlator chip will be 5.9 mm square, including some test structures. With eight correlators in one package, four each for inphase and quadrature signals, it will be possible to track four GPS satellites simultaneously.

B.E. Burke
D.L. Smythe

B. A TWO-STAGE MONOLITHIC IF AMPLIFIER UTILIZING A HIGH DIELECTRIC CONSTANT CAPACITOR

A monolithic IF amplifier has been fabricated for use in a millimeter-wave heterodyne receiver chip.⁵ The IF range of the receiver goes from 1.2 to 2.8 GHz, which is determined by the bandwidth of the balanced mixer. The design of multistage amplifiers in this frequency range requires interstage coupling capacitors from 40 to 80 pF. This requirement imposes a difficult fabrication problem, because capacitors based on dielectric materials presently used in monolithic fabrication can achieve only modest values of capacitances per unit area. Typical values of unit area capacitances obtained in the present work using 5000 Å of polyimide, SiO₂, or

Si_3N_4 are 53, 70, and 132 pF/mm^2 , respectively, as shown in Table IV-1. Use of these low dielectric constant materials for the fabrication of 60-pF interstage coupling capacitors resulted in low yield because of the high probability of including pinholes in the large areas required. A solution to this problem is the use of a higher dielectric constant material, such as Ta_2O_5 .

TABLE IV-1 COMPARISON OF DIELECTRIC MATERIALS FOR THIN FILM CAPACITORS			
Material	Relative Dielectric Constant	Thickness (Å)	Capacitance (pF/mm^2)
Polyimide	3	5000	53
SiO_2	4 to 5	5000	71
Si_3N_4	6 to 8	5000	132
Anodized Ta_2O_5	~27 to 30	~3000	834
Thermally Oxidized Ta_2O_5	~27 to 30	~2000	1251
Reactively Sputtered Ta_2O_5	~27 to 30	~1750	1430

Anodized Ta_2O_5 capacitors with Ta anodes are utilized in silicon ICs. Unit area capacitances in the range of 600 pF/mm^2 have been obtained,⁶ but high conductor losses in the Ta electrode limit their operation to frequencies below 10 kHz. Incorporation of an Al layer beneath the dielectric has increased the operating frequency to 10 MHz (see Ref. 6). Although further improvements seem possible, the anodized Ta_2O_5 capacitor process using an Al underlayer is not compatible with Au-based metallization systems used in GaAs monolithic circuits.

In view of these limitations, we have developed a reactively sputtered Ta_2O_5 thin-film capacitor process that is compatible with monolithic integration of GaAs circuits and capable of achieving unit area capacitances of 1500 pF/mm^2 . This value is over an order-of-magnitude higher than the unit area capacitances that are obtained from Si_3N_4 , SiO_2 , and polyimide capacitors.

The Ta_2O_5 dielectric layer for use in the capacitor can be obtained by anodic oxidation⁷ or thermal oxidation⁸ of a Ta layer. Alternatively, Ta_2O_5 can be reactively sputtered^{9,10} from a Ta target by Ar ions in the presence of partial pressures of oxygen. Auger analysis reveals that the chemical compositions of the layers obtained by the three techniques are the same.¹¹ Typical values of capacitances per unit area obtained from capacitors of each type are shown in Table IV-1.

A photograph of a high-frequency Ta_2O_5 capacitor is shown in Fig. IV-3. The top electrode measures 125 by 125 μm . The cross section of the capacitor shown below the photograph reveals a sequence of five layers: Au, Ta, Ta_2O_5 , Ta, and Au. The Au layers are the top and bottom electrodes for the capacitor, the Ta_2O_5 layer is the dielectric, and the thin Ta layers serve the purpose of bonding the Ta_2O_5 to the Au. Without the Ta layer, adhesion of Ta_2O_5 to the Au would be poor. Thicknesses of the layers are 1250, 250, and 1750 Å for Au, Ta, and Ta_2O_5 , respectively. To minimize losses, the thicknesses of the Ta layer should be kept to the minimum required for good adhesion.

In the reactively sputtered capacitor process the Au, Ta, Ta_2O_5 , Ta, and Au layers are deposited sequentially in a single sputtering run without breaking vacuum. An important difference between this process and the oxidation processes is that wafer handling does not occur at the formation of the dielectric layer, so that the susceptibility to particulate contamination is greatly reduced. The Au and Ta layers are deposited from their respective targets in an Ar plasma at 50 W RF power. Deposition of the Ta_2O_5 layer is accomplished by reactive sputtering the Ta target using a



111006-N-021

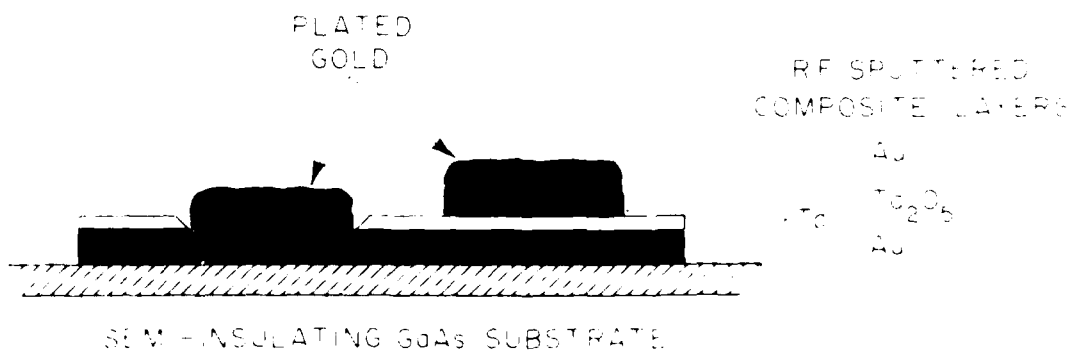


Fig. IV-3. High-frequency Ta_2O_5 capacitor.

mixture of O_2 and Ar. The RF power is maintained at 50 W, and the ratio of O_2 to Ar flow rates is 15 percent. The remaining Ta and Au layers are deposited under conditions described previously.

The fabrication sequence of the two-stage amplifier uses 9 mask levels, of which 3 levels are associated with the fabrication of the capacitor, 3 levels are used for the fabrication of FETs, and the remaining 3 levels are for the fabrication of transmission lines and bias lines. Figure IV-4 shows a diagram of this fabrication process.

The reactively sputtered Ta_2O_5 capacitor was integrated into the two-stage monolithic IF amplifier shown in Fig. IV-5. The capacitance was 140 pF and the area of the capacitor was $9.78 \times 10^{-2} \text{ mm}^2$. This capacitance is about twice the desired value because the mask set was designed assuming a lower value of capacitance per unit area. The chip measures 2.5 by 5.0 mm. Input matching of the first-stage amplifier is provided by a pair of open-circuited $8\text{-}\Omega$ stubs followed by a $140\text{-}\Omega$ high-impedance line. Electrical lengths of the stub and transmission line at 2 GHz are 4.3° and 35.3° , respectively. The FETs have 1- by $500\text{-}\mu\text{m}$ gates positioned in a drain-to-source spacing of $5 \mu\text{m}$. The epitaxial layer is directly implanted with Se^+ ions into an undoped GaAs semi-insulating substrate. Bias lines for the drains and the gate of the second stage are also indicated in the photograph. The interstage matching network is identical to the input matching network with the exception of the electrical length of the open-circuited stub, which is 8.6° at 2 GHz.

Electrical evaluation of the reactively sputtered capacitors was performed with a 1-MHz capacitance bridge and a network analyzer. Figure IV-6 shows a comparison of the 1-MHz data with the network analyzer data obtained from the capacitor connected in shunt between two sections of microstrip lines. Agreement of the data is good to approximately 300 MHz. Values of the discrete capacitor and loss tangent are $\sim 24 \text{ pF}$ and ~ 0.03 , respectively. Divergence of the data at 1 GHz is an artifact of the resonance between the capacitor and the inductance associated with the bonding wire used to connect the capacitor to the microstrip lines and to

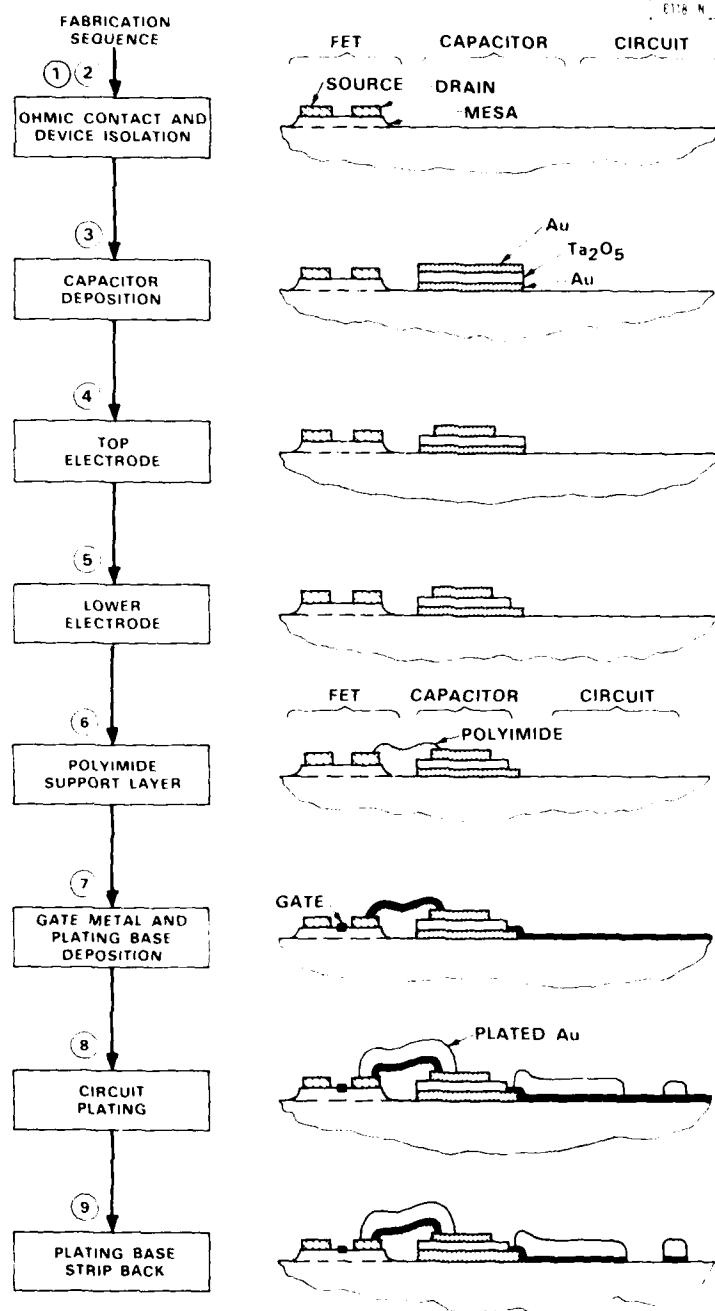


Fig. IV-4. Fabrication sequence of two-stage amplifier incorporating Ta₂O₅ capacitors.

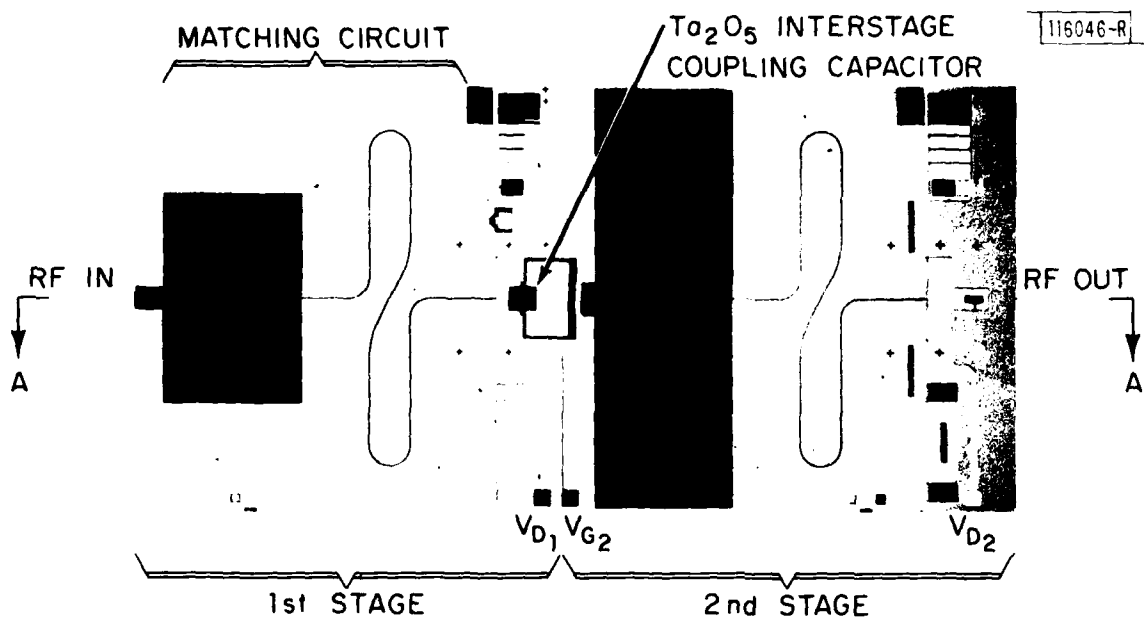
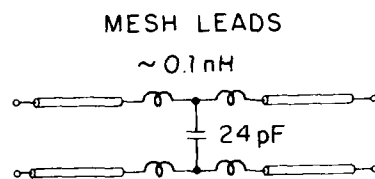
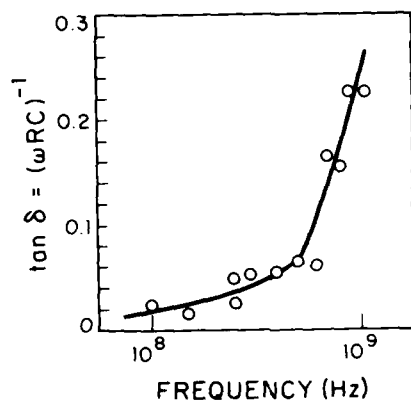
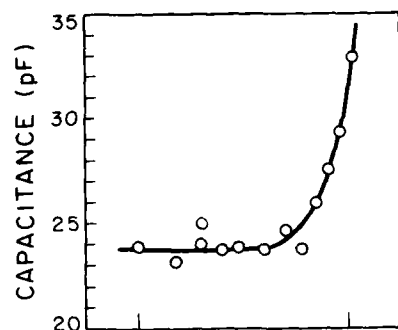


Fig. IV-5. Two-stage monolithic IF amplifier.



$C = 23.85 \text{ pF}$
 $G = 0.66 \mu\text{S}$
 $\tan \delta = 0.028$

} AT 1 MHz

Fig. IV-6. Capacitance and loss-tangent data from capacitors in shunt connection.

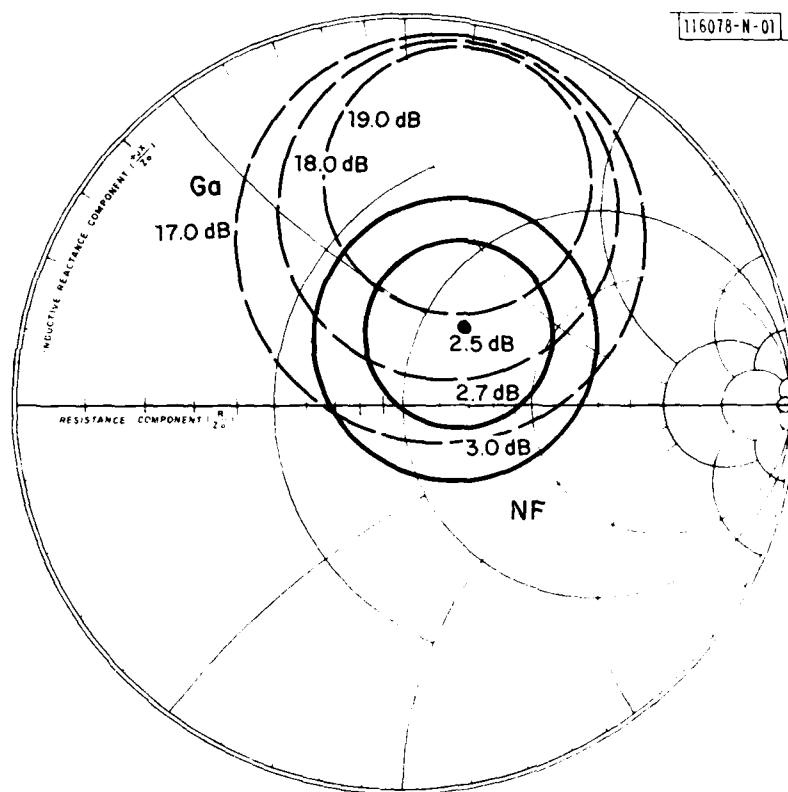
ground. Evaluation of the capacitor as an interstage coupling capacitor was performed on a 140-pF capacitor, which was cut out from an actual monolithic two-stage amplifier. Test results show an insertion loss less than 0.15 dB in the frequency band of interest.

The monolithic amplifiers were mounted in suitable fixtures and measured using a network analyzer. The noise-figure circles at 1.7 GHz are shown in Fig. IV-7 and indicate a minimum noise figure of 2.5 dB. When the amplifier is connected to a 50- Ω source, the noise figure is 2.7 dB at 1.7 GHz, 1 dB of which is the contribution of losses in the high impedance line. The associated gain is 17.5 dB. The bandwidth of the IF amplifier is shown in Fig. IV-8. The unit exhibits a gain in excess of 16.5 dB from 1.0 to 2.8 GHz.

Integration of the two-stage amplifier in the 31-GHz heterodyne receiver should provide an overall conversion gain above 10 dB. The 17.5-dB gain of the IF amplifier is sufficient to suppress noise contributions from additional stages, establishing the single-sideband receiver noise figure in the range of 9 to 10 dB.

Losses in the capacitor arise primarily from RF losses in the electrodes rather than in the dielectric material. Therefore, higher Q's can be achieved by increasing the thickness of the electrodes and reducing the area of capacitors to produce capacitances consistent with circuit design requirements and safe fabrication limits. In the present application, the Au layers can be increased to ~ 2000 Å and the area of the interstage coupling capacitor can be reduced by 50 percent and still achieve an adequate series reactance.

The reactively sputtered Ta_2O_5 capacitor, in addition to being necessary for the two-stage monolithic IF amplifier, may be useful for other monolithic circuits because large capacitances can be achieved with small



TWO-STAGE MONOLITHIC FET AMPLIFIER

Fig. IV-7. Noise figure and gain circles in input plane at 1.7 GHz.

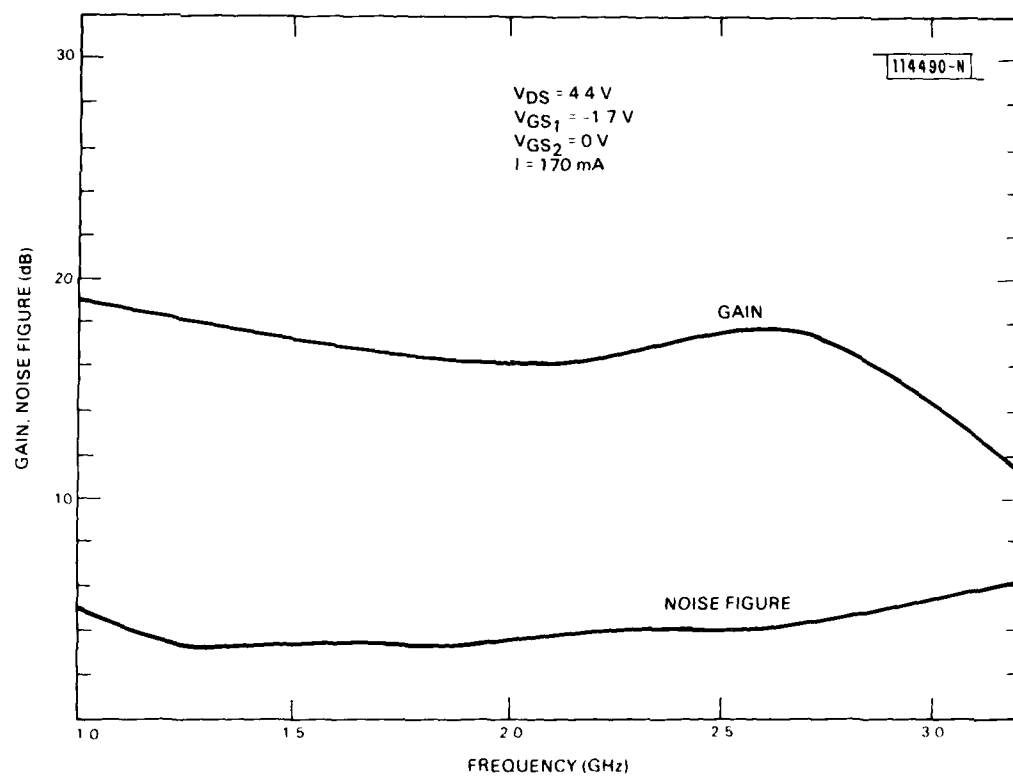
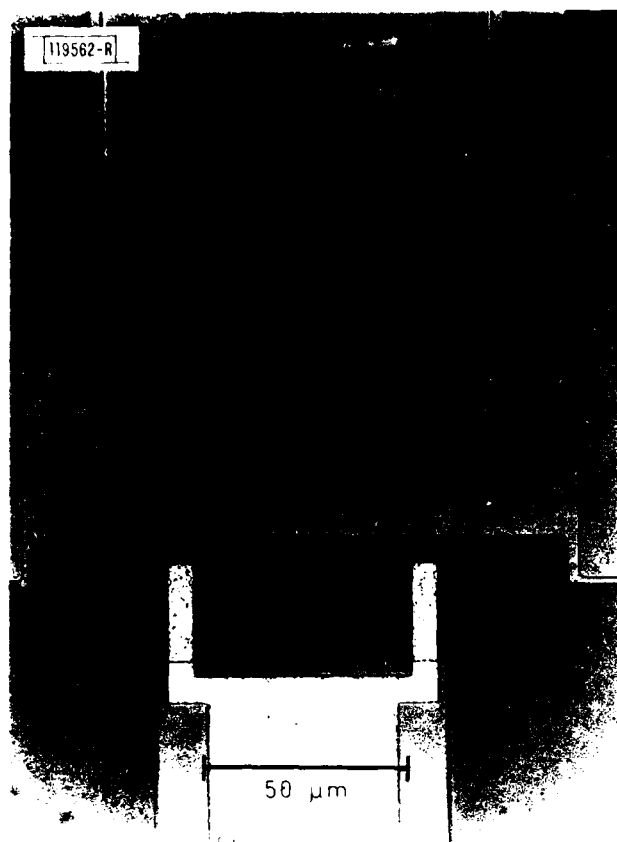
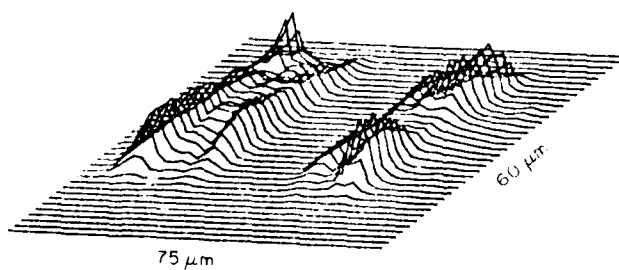


Fig. IV-8. Gain and noise figure of two-stage IF amplifier.



(a)



(b)

Fig. IV-9. (a) Photomicrograph of $0.5 \times 104\text{-}\mu\text{m}$ -gate GaAs FET. (b) Scanning plots of beat frequency from mixing two modes of a He-Ne laser in $0.5\text{-}\mu\text{m}$ -gate device.

size and high fabrication yield. Since coupling and bypass capacitors occupy a considerable fraction of the area in most microwave monolithic circuits, the large unit area capacitance of the present capacitor can reduce the size and cost of both monolithic as well as thin-film hybrid circuits.

A.Chu	W.E. Courtney (Gr.33)
L.J. Mahoney	W.J. Piacentini
M.E. Elta	J.P. Donnelly

C. HETERODYNE EXPERIMENTS FROM MILLIMETER-WAVE TO OPTICAL FREQUENCIES USING GaAs MESFETs ABOVE f_T

Substantial efforts are currently being developed to extending GaAs MESFET operation into the millimeter frequency regime. To date, experimental 0.25- μm -gate-length devices have exhibited useful gain up to 40 GHz (see Ref. 12). In the present work GaAs FETs have been investigated by operating them as mixers and detectors at much higher frequencies, significantly above f_T . Although a number of studies involving visible radiation have been made using picosecond pulses,¹³ the emphasis here is the response to CW sources.

Our results indicate that GaAs FETs can be used as sensitive and versatile detectors and mixers of millimeter-wave and optical radiation. By using GaAs FETs as millimeter mixers, results have been obtained up to 350 GHz, and by exploiting this millimeter-wave responsivity, optical mixing between two lasers has been demonstrated with IFs up to 300 GHz. These results have been reported earlier.¹⁴ Here they are described in greater detail, and possible mechanisms giving rise to the mixing phenomena are discussed.

Devices used in the experiments are 0.5- μm -gate-length MESFETs with a total gate width of 104 μm . The gate fingers are located in a drain-source spacing of ~ 4 μm . Gate capacitance and transconductance are typically 0.06 pF and 9.5 mS, respectively. Consequently, f_T is approximately 25 GHz. A photomicrograph of a typical device is shown in Fig. IV-9(a). The FETs are mounted in the common source configuration and biased in the linear region. The optical and millimeter-wave signals are coupled radiatively into the gate

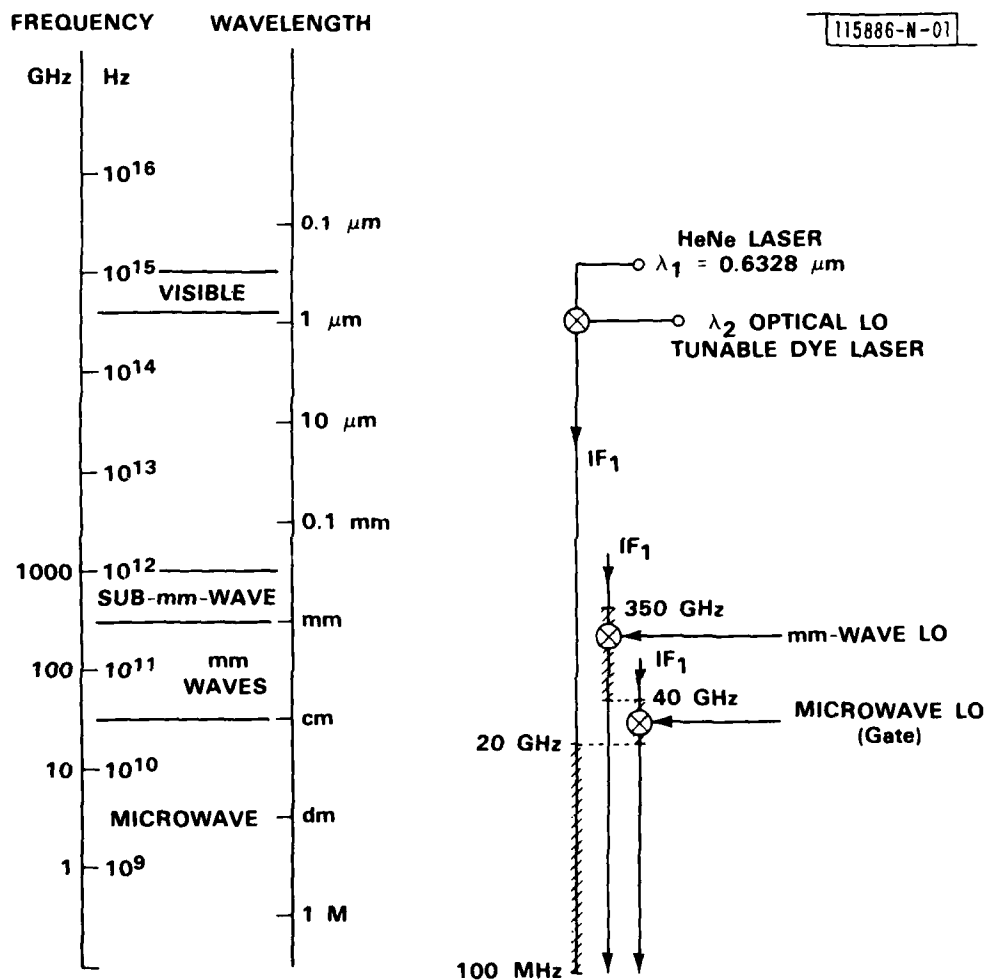


Fig. IV-10. Summary of mixing experiments in optical region showing relevant spectral regions involved.

region of the FET, and the IF is detected at the drain terminal in a 50- Ω system. The gate terminal is only used if the IF is downconverted further by a second local oscillator (LO) in the microwave range. Otherwise, the gate terminal is connected to ground via a 50- Ω resistor.

In the millimeter- and submillimeter-wave frequency ranges, the signal is radiatively coupled into the gate region by the fields of a closely spaced waveguide. The coupling is maximized when the E-field is orthogonal to the gate stripe, as indicated in Fig. IV-9(a). Video detection has been obtained up to 800 GHz by this method. Harmonic mixing was performed by combining spatially the fields of a 350-GHz carcinotron with that of a 70-GHz klystron in the vicinity of the gate region. The detected IF is the difference frequency between the \sim 350-GHz signal and the 5th harmonic of the 70-GHz LO and was typically in the range of 2 to 4 GHz. In the harmonic mixing experiment, the signal-to-noise ratio for the detected IF response was typically on the order of 45 dB.

Once millimeter-wave detection and mixing were demonstrated, it became feasible to examine optical mixing at very high IFs. Mixing in the optical region was performed by focusing a He-Ne laser at 6328 Å and a tunable stabilized dye laser pumped by an Ar⁺ ion laser onto the vicinity of the gate with an \sim 3- μ m diffraction-limited spot. Power levels for the He-Ne laser and dye laser were 1 and 50 mW, respectively. As an optical detector, the device had a signal level on the order of 60 mV. A summary of mixing experiments in the optical region showing the relevant spectral ranges involved is illustrated in Fig. IV-10. The stabilized dye laser was tuned away from the He-Ne laser to produce IFs ranging from 100 MHz to 300 GHz. In order to cover this wide IF range, three conversion techniques were used in different frequency regimes. Below 20 GHz, the IF response was detected directly using a spectrum analyzer. Between 20 and 40 GHz, the IF response was heterodyned down to 500 MHz by feeding a microwave LO into the gate terminal of the FET. The power of the microwave LO used was approximately 200 mW. Between 40- and 300-GHz downconversion of the millimeter-wave IF signal was achieved by coupling the LO (either a klystron or a carcinotron)

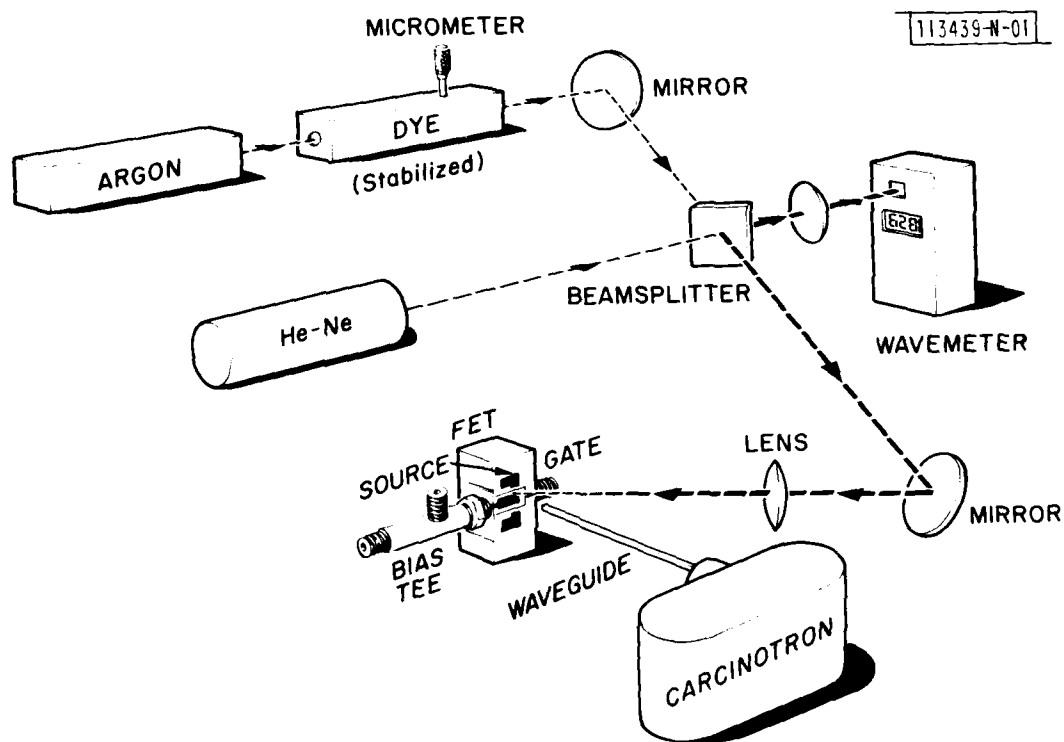


Fig. IV-11. Mixing experiment using two lasers and a millimeter-wave LO.

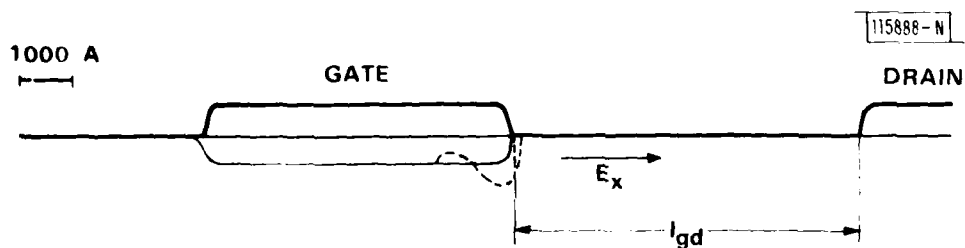


Fig. IV-12. Response to an applied millimeter-wave E-field in depletion layer.

into the gate region by means of a closely spaced waveguide, as shown in Fig. IV-11.

As a special case of optical mixing using only one laser, two modes of a He-Ne laser were also mixed in an FET to produce an IF signal of 641 MHz. In order to define the active region, the laser beam was scanned over the device; a plot of the resultant IF is shown in Fig. IV-9(b). Reduced response has also been observed from the mode mixing of a Nd:YAG laser at 1.06 μm , i.e., below the GaAs bandgap energy.

The frequency limit in most GaAs FET applications arises from the fact that the signal is fed into the gate terminal, which is loaded by the depletion layer capacitance C_g . As a result, the time constant associated with C_g and the transconductance g_m dominates the frequency response of the device. The frequency of unity current gain is given by $f_T = g_m / 2\pi C_g$ and is the primary frequency limit when the signal is fed directly into the gate terminal. However, f_T is not necessarily the upper limit when signals are radiatively coupled into the device.

For IF signals significantly above f_T , it is not possible for the depletion layer to follow the beat frequency because of long time constants associated with the large depletion layer capacitance. Hence, a different mechanism must be responsible for the observed mixing, such as photoconductivity with consequent modulation of the depletion layer and photo-induced effects at the depletion layer edges of the gate. If mixing is produced by a net change in photo-induced carrier density in the FET channel, then the rapid removal of one carrier type from the active device area is required. Both the lifetime and transit time of electrons through the gate region are too long to account for the observed high frequency response. Two possible mechanisms for more rapid carrier removal are the trapping of holes by defect centers or the differences of sweep-out rate of electrons and holes by the electric field. Trapping of holes has been proposed previously to explain the increase of gate capacitance under optical illumination.¹⁵ Then, modulation of the drain current results from variation of the channel thickness at the depletion layer edge. In Fig. IV-12, the response of the

depletion layer under the gate to an applied E-field is shown. Because of the built-in potential of the Schottky barrier, charges do not come from the gate metal, but rather originate near the boundary of the depletion layer. If the charges induced by the radiatively coupled E-field are confined to the edges of the gate, then modulation of the current in the channel takes place. The high frequency response follows by virtue of the small incremental capacitance associated with the depletion layer edge rather than with the large capacitance of the entire depletion layer. In the case of millimeter-wave mixing, a second E-field is radiatively coupled in, to downconvert to IF frequencies which are detected at the drain terminal. Mixing could arise from nonlinearities in the junction or from channel modulation effects.

A number of experiments are in progress to determine the relative importance of the mechanisms giving rise to mixing in an FET over a broad frequency range. More complex mechanisms than those discussed above may have to be invoked to explain the response that has been observed in the saturated current regime and the reduced response observed from the mode mixing of a Nd:YAG laser at 1.06 μm , below the band-gap energy.

A. Chu	D.D. Peck
H.R. Fetterman	P.E. Tannenwald

D. Si DAMAGE INDUCED BY DRY ETCHING

Techniques such as reactive-ion etching or ion milling involve ions impinging on the sample surfaces and can produce surface damage.^{16,17} In this study, Si substrates were etched either in low-pressure glow discharges of CF_4 , CHF_3 , SiCl_4 , or Cl_2 , or in an Ar-ion milling apparatus. The effects of these etching techniques on Si surfaces were investigated by measurements on MOS structures fabricated on etched surfaces, and by Secco etching to determine the extent of oxidation-induced stacking faults (OSFs).

Sample substrates were 5 to 10 $\Omega\text{-cm}$, (100), n-type Si. Some of the wafers had the POGO treatment which uses phosphorus to getter impurities to

AD-A122 252

SOLID STATE RESEARCH(U) MASSACHUSETTS INST OF TECH
LEXINGTON LINCOLN LAB A L MCWHORTER 15 MAY 82 1982-2
ESD-TR-82-055 F19628-80-C-0002

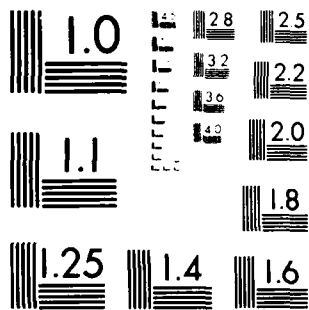
2/1

UNCLASSIFIED

F/G 20/12

NL

END
DATE
FILMED
1-83
DTIC



MICROCOPY RESOLUTION TEST CHART
NATIONAL BUREAU OF STANDARDS-1963-A

the wafer back surface. This treatment is used to minimize OSFs from sources other than surface damage. A Perkin-Elmer system with a SiO_2 target plate was employed for reactive-ion etching.¹⁸ Ar ion-beam etching was performed with a Kaufman-type ion source in a system described elsewhere.¹⁹

Prior to oxidation for MOS capacitor fabrication, the etched surfaces were subjected to a standard H_2O_2 clean. Dry HCl oxide about 1000 Å thick was grown. An unetched control sample was identically processed for comparison. Al was evaporated for front and back contacts, followed by an anneal in N_2 .

Both high-frequency and quasi-static C-V measurements were made on the MOS capacitors to determine the interface state density at the oxide/Si interface. Figure IV-13 shows the distortion in C-V curves for a sample etched in CF_4 at 250 V. The positive flatband shift indicates the presence of acceptor-like interface states. Interface-state density (N_{it}) integrated from 0.28 to 0.84 eV above the Si valence band was found to be $3.8 \times 10^{11} \text{ cm}^{-2}$ for the etched sample and $5.8 \times 10^9 \text{ cm}^{-2}$ for the control sample. The integrated interface-state densities of samples etched under various conditions are shown in Fig. IV-14 for POGO samples, and in Fig. IV-15 for samples not subject to the POGO treatment. Three important features are indicated in the figures. (1) Chlorine-based gases (SiCl_4 or Cl_2) induce less damage than fluorine-based gases (CF_4 or CHF_3) or Ar ions. (2) For a given etching gas, the degree of damage is proportional to the target voltage. (3) Surfaces etched by CHF_3 provide a better Si-SiO₂ interface than those etched by CF_4 .

The explanation for the first observation may be related to the fact that oxidation in the presence of chlorine provides improved SiO_2 films in which metallic impurities are immobilized. In addition, these HCl oxides show significantly lower pin-hole densities and induce fewer OSFs as well as having better bulk and interface properties.²⁰ Chlorine-based etching gases may provide improved surface properties or reduced damage by a chemical reaction similar to the role of chlorine in oxidation.

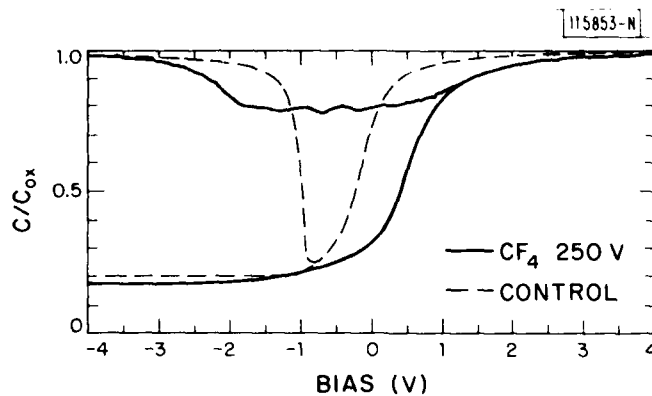


Fig. IV-13. High- and low-frequency C-V curves showing effect of interface states generation due to etching in CF_4 at 250 V.

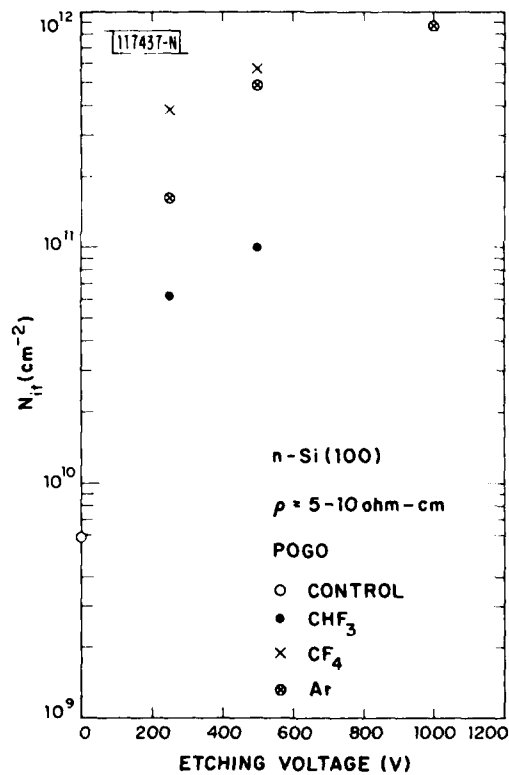


Fig. IV-14. Number of interface states induced as a function of etching voltage in CHF_3 , CF_4 , and Ar for POGO samples.

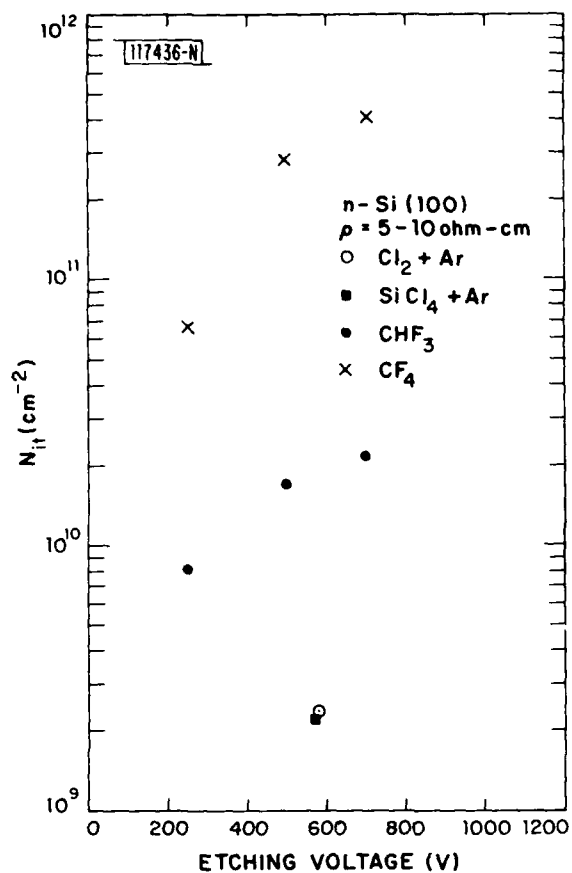
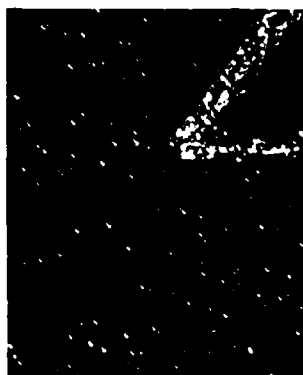


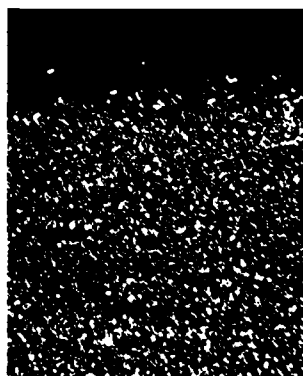
Fig. IV-15. Number of interface states induced as a function of etching voltage in $\text{Cl}_2 + \text{Ar}$, $\text{SiCl}_4 + \text{Ar}$, CHF_3 , and CF_4 for samples without POGO.



(a)



(b)



(c)

Fig. IV-16. Optical micrographs showing OSFs after etching in Secco solution for 2 min. Samples were etched by Ar ion milling at (a) 250 V, (b) 500 V, and (c) 1000 V.

The observation that damage is dependent on target voltage is expected because the energy of ions impinging on the surface is proportional to the target voltage. At higher ion energies, the structural damage in Si due to physical sputtering is greater. However, a chemical reaction involving hydrogen in the etching environment may be important in minimizing sputtering-induced surface damage. Hydrogen is well known for its role in completing Si dangling bonds at the Si-SiO₂ interface and hence lowering the density of fast surface states.²¹ The availability of H⁺ could explain the lower N_{it} associated with MOS capacitors formed on the surfaces etched in CHF₃ gas compared with those etched in CF₄. One potential disadvantage of using CHF₃ in place of CF₄ in etching is its greater tendency to form polymer films (CF₂)_n on the surfaces. Our results show that, in our case, the MOS interface properties are not affected by CHF₃-induced polymer films.

Wet oxides about 5000 Å thick were also grown on the etched wafers. The oxides were then etched back in Secco solution (Cr₂O₃ + H₃PO₄ + HF + H₂O) to bring out OSFs. Figure IV-16(a-c) shows the comparison between samples etched by Ar-ion milling at 250, 500, and 1000 V. The density of defects increases with ion energy. Portions of the wafers were covered during etching, and they are free of OSFs as shown in Figs. IV-16(a) and (c). Nucleation of stacking faults during oxidation can be due to structural distortion as well as impurities in the Si. Any OSF observed on these samples is related to damage induced by dry etching.

S.Pang	R.W. Mountain
D.D. Rathman	P.D. DeGraff
D.J. Silversmith	

REFERENCES

1. Solid State Research Report, Lincoln Laboratory, M.I.T. (1981:3), pp. 45-49, DTIC AD-A112696.
2. Ibid. (1980:2), pp. 26-29, DTIC AD-A092724/4.
3. C.H. Sequin, M.F. Tompsett, D.A. Sealer, and R.E. Crochiere, IEEE Trans. Electron Devices ED-24, 746 (1977).
4. P. Van Broekhoven, ADGINT Memo (M)-111, C.S. Draper Laboratory (February 21, 1981).
5. A. Chu, W.E. Courtney, and R.W. Sudbury, IEEE Trans. Electron Devices ED-28, 149 (1981), DTIC AD-A107062/2.
6. F.L. Feinstein and R. Pagano, IEEE Trans. Components, Hybrids and Manufacturing Tech. CHMT-4, 140 (1981).
7. W.D. Westwood, N. Waterhouse, and P.S. Wilcox, Tantalum Thin Films (Academic Press, New York, 1976), p. 290.
8. L. Holland, Vacuum Deposition of Thin Films (Chapman & Hall, Ltd., London, 1966), Chap. 15, pp. 450-455.
9. T.M. Reith, "The Reactive Sputtering of Tantalum Oxide," Ph.D. Thesis, Syracuse University (University Microfilms International), Ann Arbor, Michigan (1980).
10. M.E. Elta, A. Chu, L.J. Mahoney, R.T. Cerretani, and W.E. Courtney, IEEE Electron Device Lett. EDL-3, 127 (1982).
11. A. Chu, L.J. Mahoney, M.E. Elta, W.E. Courtney, M.C. Finn, W.J. Piacentini, and J.P. Donnelly, IEEE Trans. Microwave Theory Tech. (to be published).
12. E.T. Watkins, H. Yamasaki, and J.M. Shellenberg, ISSCC Digest of Technical Papers, February 1982, pp. 198-199.
13. P.R. Smith, D.H. Auston, and W.M. Augustyniak, Appl. Phys. Lett. 39, 739 (1981).
14. Solid State Research Report, Lincoln Laboratory, M.I.T. (1982:1).
15. J.J. Sun, R.J. Gutman, and J.M. Borrego, Solid-State Electron. 24, 935 (1981).

16. L.M. Ephrath, D.J. DiMaria, and F.L. Pesavento, J. Electrochem. Soc. 128, 2415 (1981).
17. J. Garrido, E. Calleja, and J. Piqueras, Solid-State Electron. 24, 1121 (1981).
18. C.M. Horwitz and J. Melngailis, J. Vac. Sci. Technol. 19, 1408 (1981).
19. P.D. DeGraff and D.C. Flanders, J. Vac. Sci. Technol. 16, 1906 (1979), DDC AD-A090069/6.
20. J. Monkowski, Solid State Tech. 22, 58 (1979); also Solid State Tech. 22, 113 (1979).
21. A.G. Revesz, The Physics of SiO₂ and Its Interfaces, S.T. Pantelides, Ed. (Pergamon, New York, 1978), pp. 222-226.

V. ANALOG DEVICE TECHNOLOGY

A. SUPERCONDUCTIVE MATCHED FILTERS: PULSE COMPRESSION

In a previous report¹ the concept of superconductive matched filters was presented, possible implementations suggested, and design trade-offs analyzed. Linearly frequency-modulated (LFM) dispersive delay lines have since been designed and fabricated using modifications of these concepts. In this report we present the first demonstration of pulse compression with superconductive devices.

A LFM dispersive delay line is shown in Fig. V-1. This chirp filter gives 27 ns of dispersion over a 2-GHz bandwidth centered on 4 GHz. The stripline structure consists of a 2000-Å-thick patterned niobium film sandwiched between two 5-cm-dia., 125-μm-thick sapphire wafers with surrounding ground planes. The pattern has two parallel lines with a total length of 2.5 m wound in a spiral pattern. The input line is coupled to the output line at prescribed points by bringing the two lines into and out of closer proximity, thereby forming quarter-wavelength-long backward-wave couplers (inset, Fig. V-1). The resonant frequency of the couplers is designed to be a linear function of distance along the line pair, producing the desired linear group delay vs frequency relation, in this case an upchirp. The couplers in this device are not amplitude-weighted, so that the magnitude of the frequency response increases linearly with frequency. A matching device, identical except for the sign of the delay vs frequency slope, was also fabricated.

A 200-mV DC step with a 25-ps risetime was applied to the input of the expander, in this case the downchirp device. The resulting 27-ns-long LFM pulse is amplified and time-gated, producing the pulse shown in the lower trace of Fig. V-2(a). This is applied to the input of the compressor, the upchirp device. The resulting compressed pulse is displayed in the upper trace of Fig. V-2(a). Expanded in time, this same pulse is also shown in Fig. V-2(b).

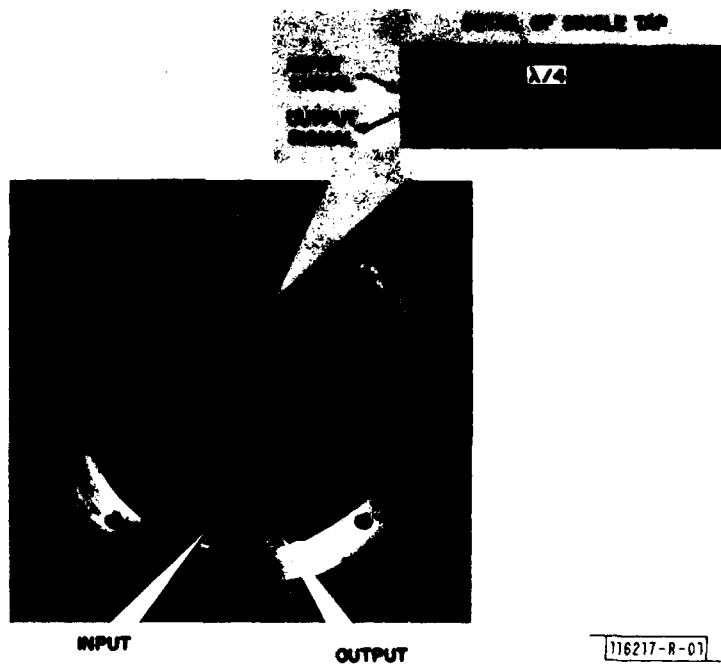


Fig. V-1. Superconductive proximity-tapped delay line just prior to assembly. This device produces a chirp which commences at 3 GHz and rises to 5 GHz over a 27-ns interval. Each tap pair has a coupling strength of -48 dB, calculated theoretically and verified experimentally. One of the quarter-wavelength-long backward-wave couplers is shown in the inset.

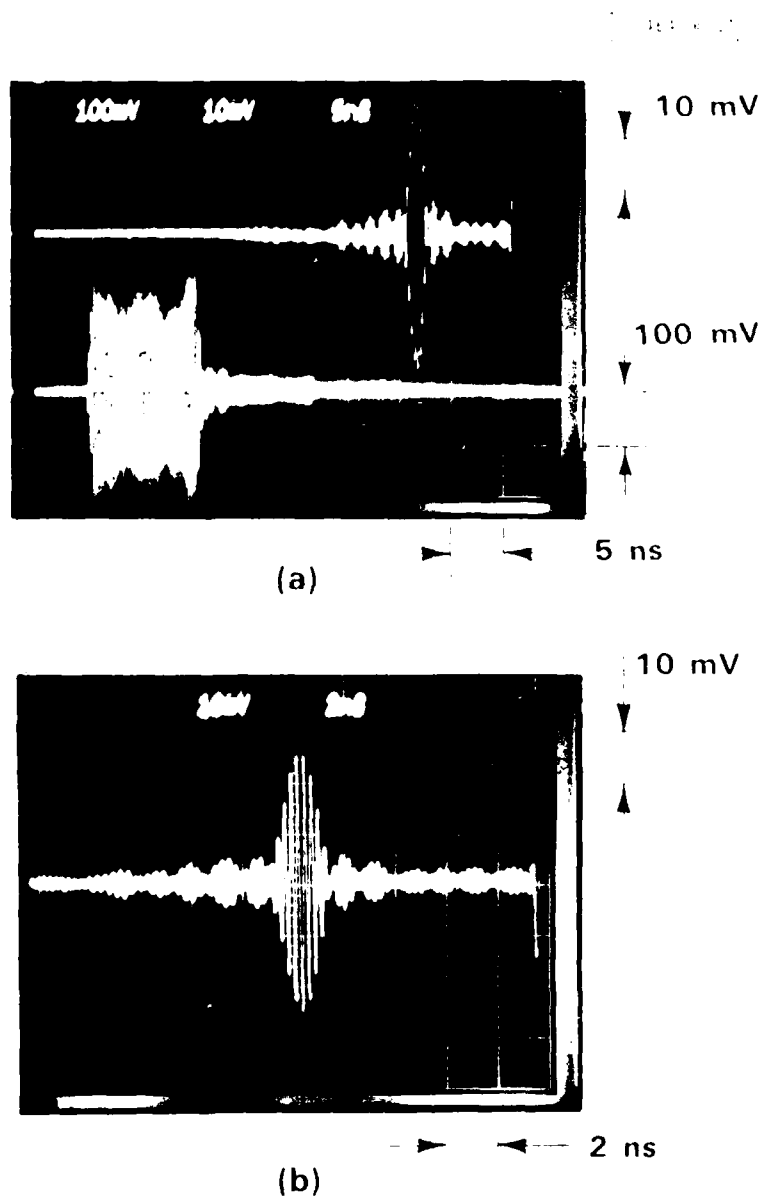


Fig. V-2. Demonstration of pulse compression with two superconductive tapped delay lines. (a) Lower trace: amplified and time-gated expanded pulse from downchirp device. Instantaneous frequency varies linearly from 4200 to 3400 MHz in time. Upper trace: compressed pulse output from upchirp matched filter. (b) Enlarged view of compressed pulse of (a).

Had the compressor been weighted for a flat frequency response, the compressed pulse would be expected to have a $(\sin x)/x$ envelope. (The use of a step rather than impulse input corrects for tilt of the expander's frequency response.) The envelope of the pulse in Fig. V-2(b) has a similar form. The amplitudes of the first three trailing side lobes are, relative to that of the main lobe, 0.22, 0.15, and 0.09, which compare favorably with the $(\sin x)/x$ values of 0.212, 0.127, and 0.091. The width of the main lobe of the compressed pulse is 2.5 ns, exactly what is expected from an input of 800 MHz bandwidth.

For ease of fabrication of these preliminary devices, the input line is not terminated in a matched load but is instead looped around to the beginning of the output line, as may be seen in Fig. V-1. This direct-transmission signal produces serious degradation in both the expander and compressor performance, but its effects may be separated in time from the compressed pulse output by time-gating the expanded pulse, removing several nanoseconds at both its leading and trailing edges. Of course, there is a commensurate loss in time-bandwidth product. In the upper trace of Fig. V-2(a) the arrival of the interfering signal is seen to be delayed until 9 ns after the compressed pulse. In future designs, a quadruple-spiral design will be implemented, providing four rather than two ports so that each end of both lines may be easily terminated in a proper load. This structure will also permit the cascading of devices.

A numerical model has been constructed that can be used to calculate the transfer functions of dispersive filters with arbitrary amplitude weighting. The transfer function of a filter can be multiplied by that of another filter or by the spectrum of an arbitrary LFM input and subsequently Fourier transformed to give the compressed pulse response. Such a calculation was made for the actual upchirp filter of Fig. V-1. If one uses the time-gated pulse in Fig. V-2(a) as input, the envelope of the compressed output is predicted to be that shown in Fig. V-3. This theoretical prediction is remarkably close to the experimental result of Fig. V-2(b).

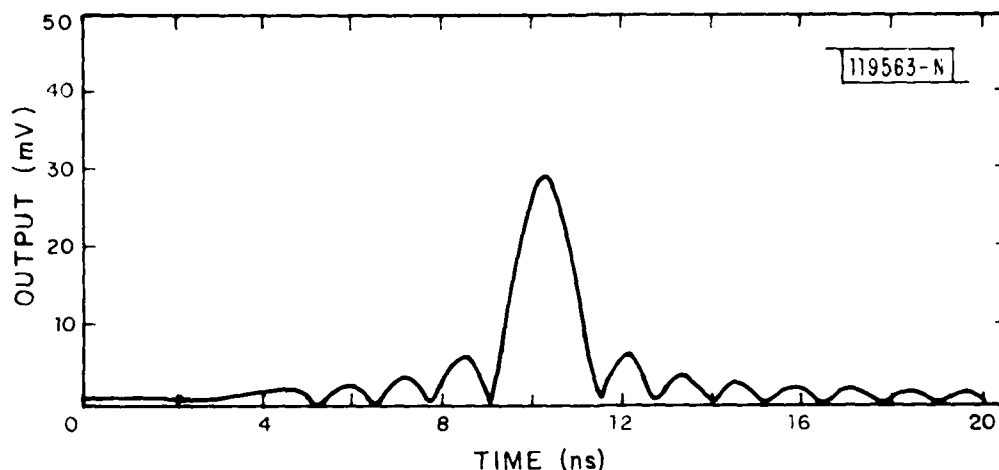


Fig. V-3. Theoretical calculation of compressed pulse envelope of Fig. V-2(b). Actual device parameters of upchirp device of Fig. V-1 and a 10.6-ns-long, 4200- to 3400-MHz downchirp of 180 mV amplitude, as seen in Fig. V-2(a), were used as input.

In conclusion, the ability to design, model, and fabricate superconductive dispersive delay lines has been demonstrated. Devices with greater dispersion, wider bandwidth, and amplitude weighting are now in design and fabrication. Devices with time-bandwidth products of 1000 appear to be feasible in the near future.

R.S. Withers P.V. Wright
A.C. Anderson S.A. Reible

B. TEMPERATURE DEPENDENCE OF WIDEBAND SAW RAC DEVICES ON QUARTZ

1. Introduction

For adequate temperature stability, LiNbO_3 surface-acoustic-wave (SAW) reflective-array-compressor (RAC) devices are usually operated in a temperature-controlled oven. Since size, weight, and power consumption are important considerations in mobile systems there is substantial interest in the development of wide-bandwidth temperature-stable RACs. There are two very promising orientations of quartz for the realization of temperature-stable RACs: the well-known ST cut and the recently proposed RAC cut.² Both

cuts have low piezoelectric coupling, and edge-bonded transducers (EBTs) must be used to obtain wide bandwidth. Such transducers have been previously reported.³ Here, we report detailed measurements of the temperature dependence of wide-bandwidth RAC devices fabricated on ST- and RAC-cut quartz.

A theoretical treatment of the temperature dependence of a RAC on ST quartz was not available until recently because of the complications arising from the temperature dependence of the anisotropy in velocity. As is well known, the ST cut is anisotropic in velocity and in the temperature-coefficient of delay (TCD). The latter is zero in the X (long) direction and 47 ppm in the perpendicular direction. Thus, changes in temperature produce not only changes in delay but also changes in the angle of reflection.⁴ In RAC-cut quartz the two directions of SAW propagation are by crystal symmetry equivalent, with equal velocities and equal TCDs, so that temperature dependence may be analyzed using the method developed for isotropic substrates.⁵

2. Theory

In this section an abbreviated analysis is given of the temperature behavior of an anisotropic RAC substrate which includes the effects of changes in the angle of reflection. A more complete treatment is given in Ref. 6.

Consider a RAC device which at design temperature has design center frequency f_o , chirp slope μ (MHz/ μ s), and isotropic velocity v_d . Through an appropriate distortion of the coordinate system, we can treat anisotropic materials. Assume that the temperature changes. In terms of the fractional changes in velocity d_x and d_z , the velocities along the x and z directions in Fig. V-4 can be written as

$$v_x = v_d (1 - d_x)$$

$$v_z = v_d (1 - d_z) \quad .$$

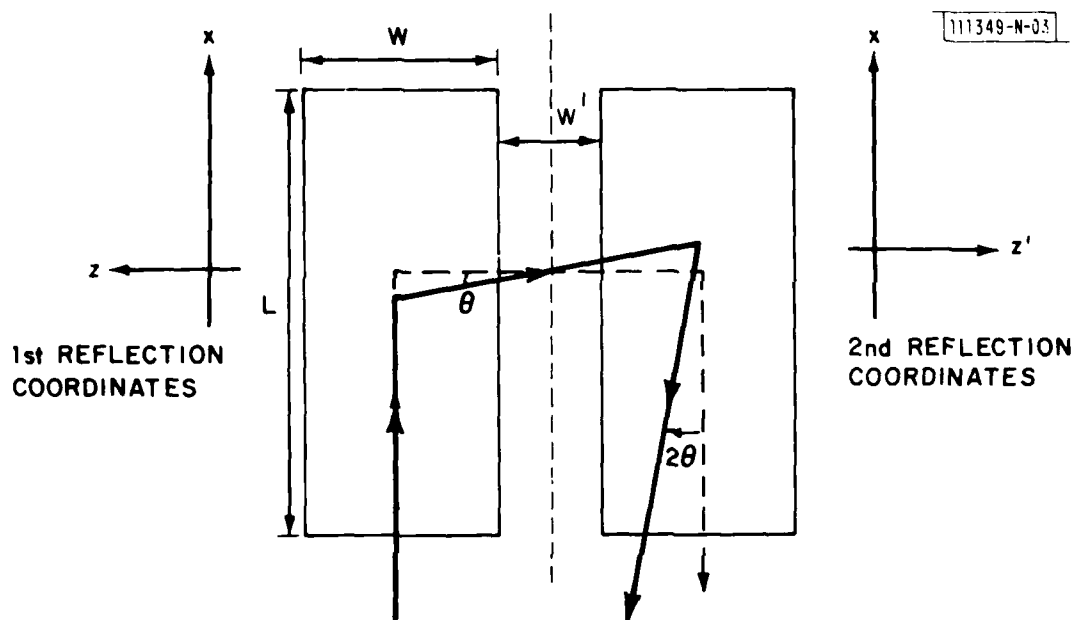


Fig. V-4. Reflection path for one particular frequency at shifted temperature.

The point of maximum reflection shifts to the point (x, z) , which satisfies

$$\frac{2\pi f_o}{v_d} + (x + z) \frac{2\pi}{v_d} 2\mu = \frac{2\pi f}{v_x} (1 + \theta)$$

where $\theta = d_z - d_x \ll 1$ is the angle which the first reflection makes with the z axis. At $f = f_o$, this is

$$\frac{x + z}{v_d} = \frac{f_o}{2\mu} d_z$$

Similarly, the point of maximum reflection at $f = f_o$ in the second grating shifts to the point (x, z) , where

$$\frac{x + z}{v_d} = \frac{f_o}{2\mu} (2d_x - d_z)$$

The reflections thus follow the paths shown in Fig. V-4. The dotted line in Fig. V-4 shows the reflection path at design temperature.

It can be shown⁷ that the phase ϕ as measured at the output transducer is

$$\frac{2\pi}{2\hat{\mu}} (f - \hat{f}_o)^2 - \frac{2\pi}{v_d} 2\phi f_z' \quad (V-1)$$

where

$$\hat{f}_o = f_o (1 - d_x)$$

$$\hat{\mu} = \mu(1 - 2d_x) \quad .$$

The first term in Eq. (V-1) shows that the x-direction TCD is the only one which affects the chirp slope and center frequency (to first order in d_x and d_z).

The important result of this analysis, then, is that the chirp slope of an ST-quartz RAC shows a parabolic dependence of temperature as determined by the second-order temperature coefficient of delay in the X direction. That is, $d_x = B(T - T_o)^2$, where B is the second-order TCD, T is temperature in degrees Celsius, and T_o is the turnover temperature. The first-order TCD is zero.

The group delay at center frequency $\tau_g(f_o)$ and its variation with temperature are parameters of interest for a RAC ($\tau_g = d\phi/df$). Group delay in a RAC is composed of two components; one is due to the delay in the grating and the other is due to propagation on the bare surface of the substrate. Thus, the temperature dependence of τ_g for an ST-quartz RAC is parabolic due to the x direction with the addition of a small linear component due to the z direction (which has a nonzero first-order TCD). The addition of a small linear term simply means that there will be a shift of the turnover temperature in the group delay vs temperature curve relative to the turnover temperature of the chirp slope vs temperature curve.

The second term in Eq. (V-1) indicates that, at the output transducer, the acoustic wave is tilted at an angle of 2θ ; the tilt introduces added insertion loss.

For a very long array, it can be shown that the total transfer function (away from the band edges) is proportional to

$$\int_0^{W_{\text{eff}}} E(x) \cos \left[2\pi\theta(W_{\text{eff}} - x) \frac{f}{2\mu} \right] dx$$

where

$$W_{\text{eff}} = \frac{W \sqrt{2\mu}}{v_d}$$

and

$$E(x) = \int_0^x \exp \left[\frac{-j\pi z^2}{2} \right] dz \quad .$$

Interestingly, if the output SAW were a simple, flat wave tilted at an angle 2θ from the transducer (as the case of a periodic grating⁸), the response would be a $(\sin x)/x$ pattern with nulls at $\theta f/2\mu = 1/2$ and 1. This is not the case for a RAC.

3. Measurements

Measurements were carried out on RAC devices fabricated on both ST-cut quartz and on RAC-cut quartz. The parameters for both devices are given in Table V-1.

The devices were placed directly in a temperature-controlled liquid bath. At each temperature, complete phase and amplitude data were taken. A quadratic function

$$\phi = \phi_0 + (f - f_0) C_1 + \frac{(f - f_0)^2}{2\mu}$$

TABLE V-1		
PARAMETERS OF MEASURED DEVICES		
	ST Quartz	RAC Quartz
Center Frequency f_o	100 MHz	125 MHz
Bandwidth Δf	14 MHz (downchirp)	50 MHz (downchirp)
Dispersive Delay Δt	30 μs	38 μs
TB $\Delta f \cdot \Delta t$	420	1900
Group Delay at f_o $\tau_g(f_o)$	21.87 μs	24.40 μs
Chirp Slope	0.452 MHz/ μs	1.316 MHz/ μs

was then fitted to the phase data using a least-squares procedure. The group delay is

$$\tau_g = C_1 + \frac{f - f_o}{\mu}$$

The devices are characterized by determining the chirp slope, group delay at center frequency $\tau_g(f_o)$, and device insertion loss at three frequencies: center frequency and the ends of the passband, $f_o + \Delta f/2$, and $f_o - \Delta f/2$. The data for ST quartz are plotted in Figs. V-5 through V-7, and for RAC-cut quartz in Figs. V-8 through V-10. Each plot shows the changes in the parameter values from those measured at room temperature. For the chirp-slope and group-delay data, the points given are fractional changes in parts per million and for insertion loss the changes given are in decibels. The statistical errors in the individual points are smaller than 1 ppm.

4. Results and Conclusions

First, let us examine the results from ST quartz. The theoretical analysis predicts a parabolic change in both chirp slope and group delay. Figure V-5 shows the measured data and a theoretical curve for chirp slope

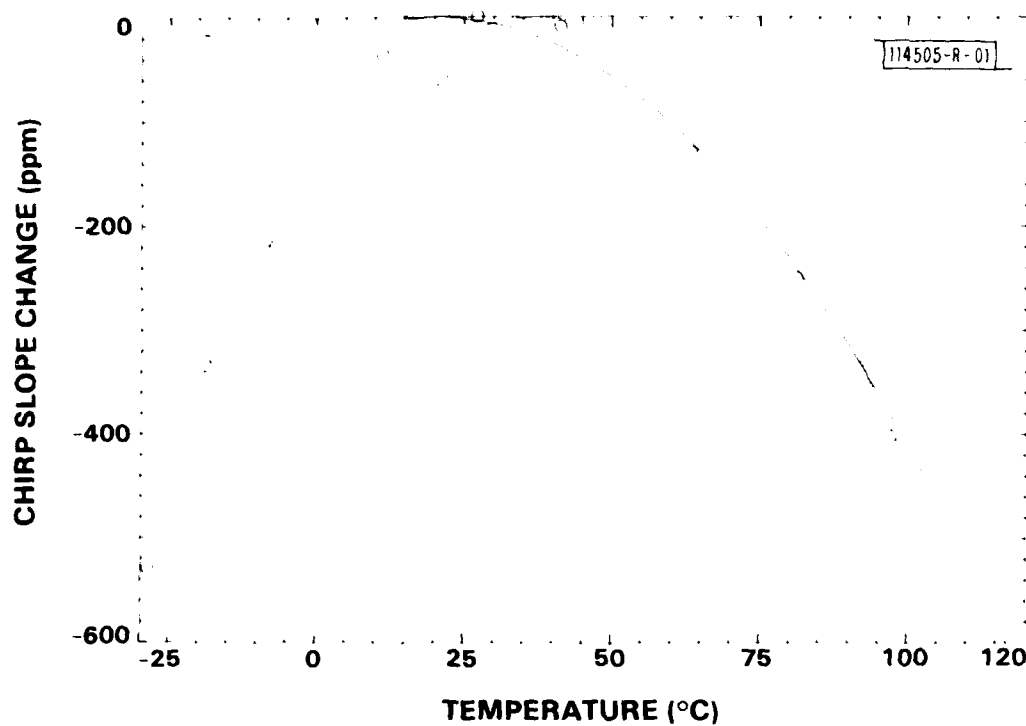


Fig. V-5. Chirp slope change vs temperature for ST quartz: points are measured values; solid line is computed using published value of $0.064 \text{ ppm}/(^{\circ}\text{C})^2$ for second-order TCD. Dotted line is best fit to data and gives a value $0.11 \text{ ppm}/(^{\circ}\text{C})^2$ for second-order TCD.

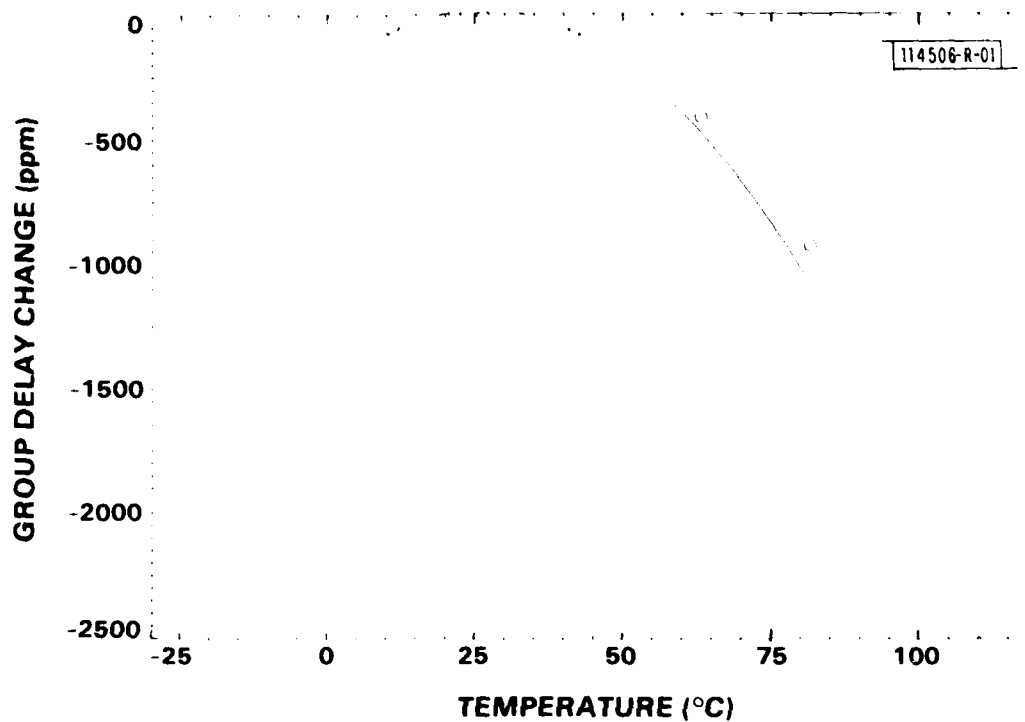


Fig. V-6. Change in group delay at center frequency vs temperature for ST quartz: points are measured values; solid line is computed using published TCD.

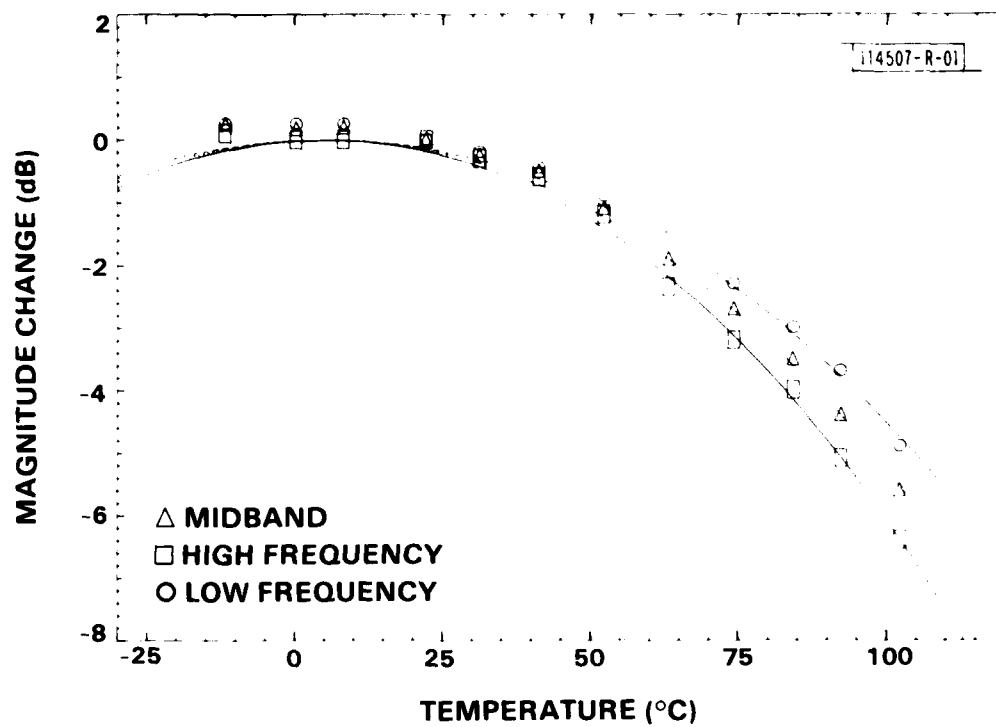


Fig. V-7. Change in magnitude of frequency response vs temperature for ST quartz: points are measured values; dashed, dotted, and solid lines are computed.

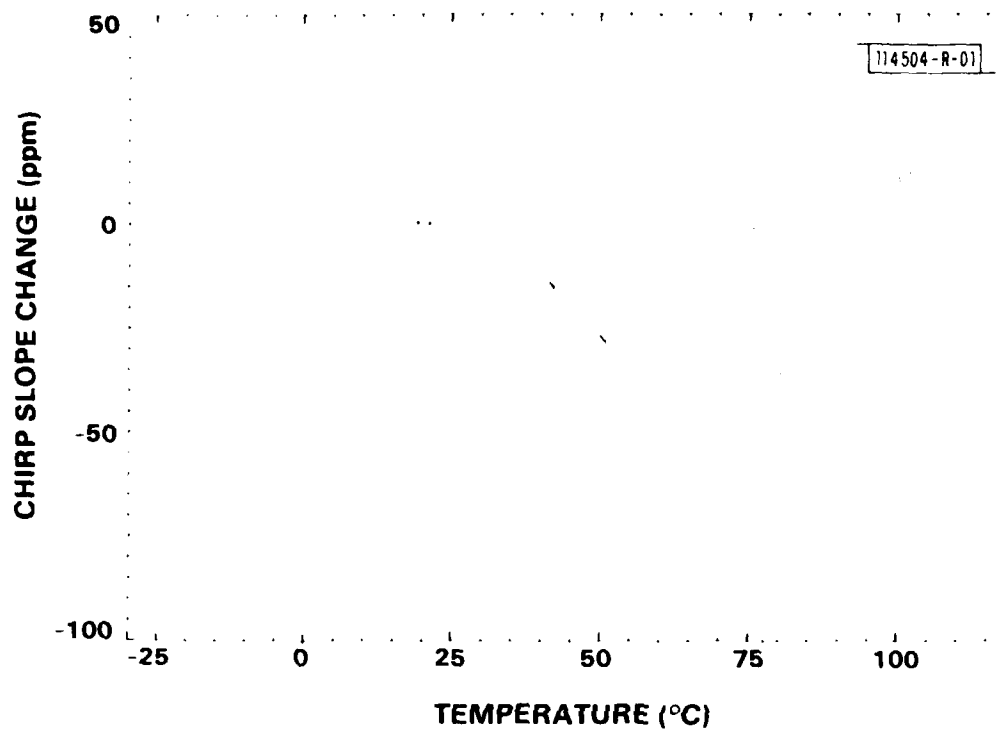


Fig. V-8. Chirp slope change vs temperature for RAC-cut quartz: points are measured values; solid line is computed.

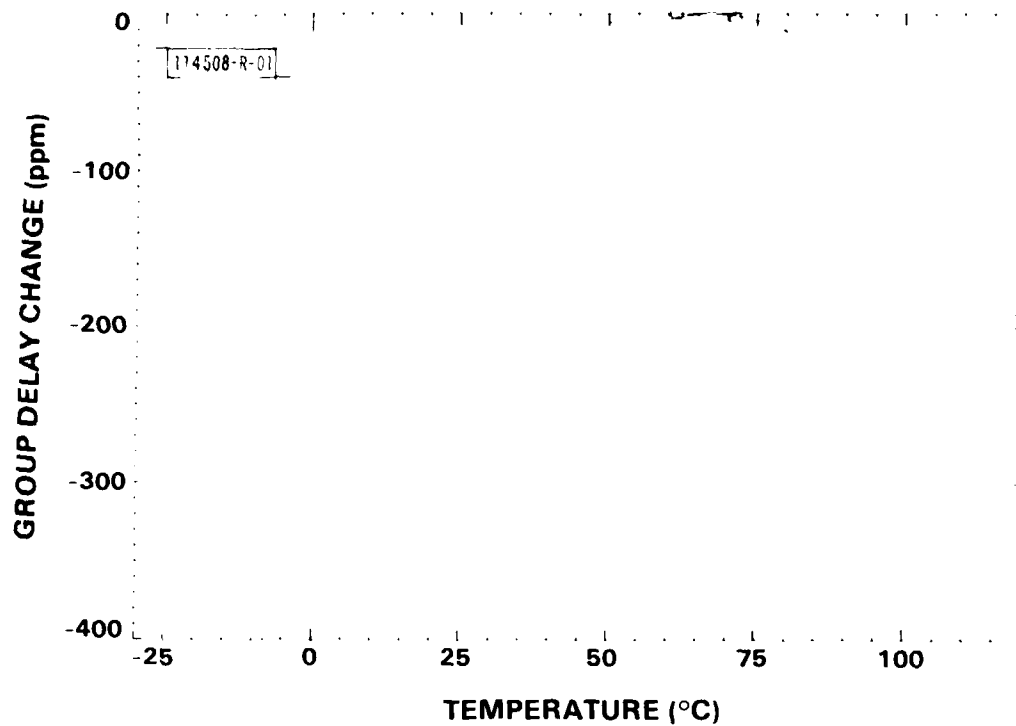


Fig. V-9. Group delay change vs temperature for RAC quartz: points are measured values; solid line is computed with a shift of turnover temperature to fit data.

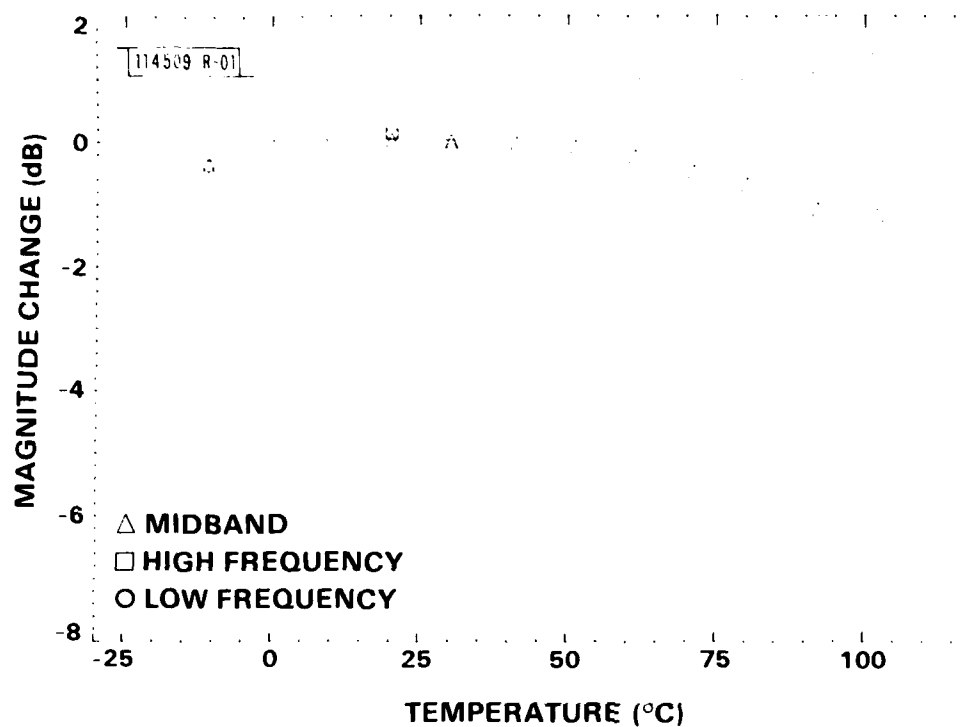


Fig. V-10. Change in magnitude of frequency response vs temperature for RAC quartz: points are measured values; dashed, dotted, and solid lines are computed.

assuming a turnover temperature of 20°C (solid line), as well as a best quadratic fit (dotted line). The fit has a coefficient of $0.11 \text{ ppm}/(^{\circ}\text{C})^2$, whereas the theoretical coefficient is 0.064. Similarly, we show measured data and a theoretical curve for group delay in Fig. V-6. In both cases, the fit is quite good, with only a slight deviation at low temperatures. Thus, there is very good evidence to support the analysis method as well as the claim that the phase properties of ST-quartz RACs are two orders of magnitude better than those of LiNbO_3 . In Fig. V-7, we have plotted the insertion loss at the top, middle, and bottom of the frequency band as well as the predicted curve. The match is quite striking.

Figures V-8 through V-10 are plots of the same data for RAC quartz. In Fig. V-8, the turnover temperature of the theoretical curve has been shifted by 45°C to agree with the measured data. Such a shift could be explained by a small error in the angle of the crystal cut within the tolerances with which the crystal was fabricated. Although the group delay shows the predicted quadratic change, the nonquadratic nature of the measured chirp slope deviation is not yet understood. Note, however, that the temperature dependence is even less than predicted, with a total change over 120°C of less than 50 ppm. Measurements have also shown an unexplained rolloff in insertion loss at the lower frequencies, where the model predicts only isotropic changes and thus theoretically no change in loss. We suspect that such rolloff is due to a temperature-dependent change in the beam steering angle of RAC quartz.⁹

In summary, both RAC and ST quartz have been shown to be two orders of magnitude more phase stable over a 100°C range than LiNbO_3 . Thus, with the advent of EBTs, such devices will prove useful in applications where temperature-stable wideband RACs are needed. Both cuts, however, exhibit a frequency-dependent insertion loss variation, which must be taken into account for devices requiring accurate amplitude weighting.

On the basis of the measurements presented here, it is clear that the temperature stability of the RAC cut is superior to that of the ST cut when one considers chirp slope and group delay variations. However, the RAC cut shows a larger change in the amplitude response across the passband of the

device as a function of temperature. It should be emphasized that the stability of ST quartz is still excellent. Therefore, the availability of substrates and the lack of beam steering might still make the ST cut the choice for a particular application.

D.E. Oates
D.M. Boroson

REFERENCES

1. Solid State Research Report, Lincoln Laboratory, M.I.T. (1981:2), p. 57, DTIC AD-A110947/9.
2. D.E. Oates, IEEE Trans. Sonics Ultrason. SU-26, 428 (1979), DDC AD-A085793/8.
3. D.E. Oates and R.A. Becker, Appl. Phys. Lett. 38, 761 (1981), DTIC AD-A103292/9.
4. D.E. Oates and R.C. Williamson, 1979 Ultrasonics Symposium Proceedings (IEEE, New York, 1979), p. 691, DTIC AD-A090871/5.
5. T. Martin, private communication.
6. D.M. Boroson and D.E. Oates, 1981 Ultrasonics Symposium Proceedings (IEEE, New York, 1981), p. 38.
7. D.M. Boroson and D.E. Oates (unpublished).
8. P.C. Meyer and M.B. Schulz, 1973 Ultrasonics Symposium Proceedings (IEEE, New York, 1973), p. 500.
9. D.F. Williams and F.Y. Cho, Electron. Lett. 17, 164 (1981).

UNCLASSIFIED

SECURITY CLASSIFICATION OF THIS PAGE (When Data Entered)

REPORT DOCUMENTATION PAGE		READ INSTRUCTIONS BEFORE COMPLETING FORM
1. REPORT NUMBER ESD-TR-82-055	2. GOVT ACCESSION NO. AD 4122 252	3. RECIPIENT'S CATALOG NUMBER
4. TITLE (and Subtitle) Solid State Research		5. TYPE OF REPORT & PERIOD COVERED Quarterly Technical Summary 1 February — 30 April 1982
		6. PERFORMING ORG. REPORT NUMBER 1982:2
7. AUTHOR(s) Alan L. McWhorter		8. CONTRACT OR GRANT NUMBER(s) F19628-80-C-0002
9. PERFORMING ORGANIZATION NAME AND ADDRESS Lincoln Laboratory, M.I.T. P.O. Box 73 Lexington, MA 02173-0073		10. PROGRAM ELEMENT, PROJECT, TASK AREA & WORK UNIT NUMBERS Program Element No. 63250F Project No. 649L
11. CONTROLLING OFFICE NAME AND ADDRESS Air Force Systems Command, USAF Andrews AFB Washington, DC 20331		12. REPORT DATE 15 May 1982
		13. NUMBER OF PAGES 126
14. MONITORING AGENCY NAME & ADDRESS (if different from Controlling Office) Electronic Systems Division Hanscom AFB, MA 01731		15. SECURITY CLASS. (of this report) Unclassified
		15a. DECLASSIFICATION DOWNGRADING SCHEDULE
16. DISTRIBUTION STATEMENT (of this Report) Approved for public release; distribution unlimited.		
17. DISTRIBUTION STATEMENT (of the abstract entered in Block 20, if different from Report)		
18. SUPPLEMENTARY NOTES None		
19. KEY WORDS (Continue on reverse side if necessary and identify by block number)		
solid state devices	photodiode devices	infrared imaging
quantum electronics	lasers	surface-wave transducers
materials research	laser spectroscopy	charge-coupled devices
microelectronics	imaging arrays	acoustoelectric devices
analog device technology	signal processing	
20. ABSTRACT (Continue on reverse side if necessary and identify by block number)		
<p>This report covers in detail the solid state research work of the Solid State Division at Lincoln Laboratory for the period 1 February through 30 April 1982. The topics covered are Solid State Device Research, Quantum Electronics, Materials Research, Microelectronics, and Analog Device Technology. Funding is primarily provided by the Air Force, with additional support provided by the Army, DARPA, Navy, NASA, and DOE.</p>		

UNCLASSIFIED

SECURITY CLASSIFICATION OF THIS PAGE (When Data Entered)

ILMEI
— 83